UiT
THE ARCTIC
UNIVERSITY
OF NORWAY

Faculty of Science and Technology
Department of Physics and Technology

Optimization of Wind Turbine Location in Urban Environment

Trond-Ola Hågbo

EOM-3901 Master's Thesis in Energy, Climate and Environment, June 2017

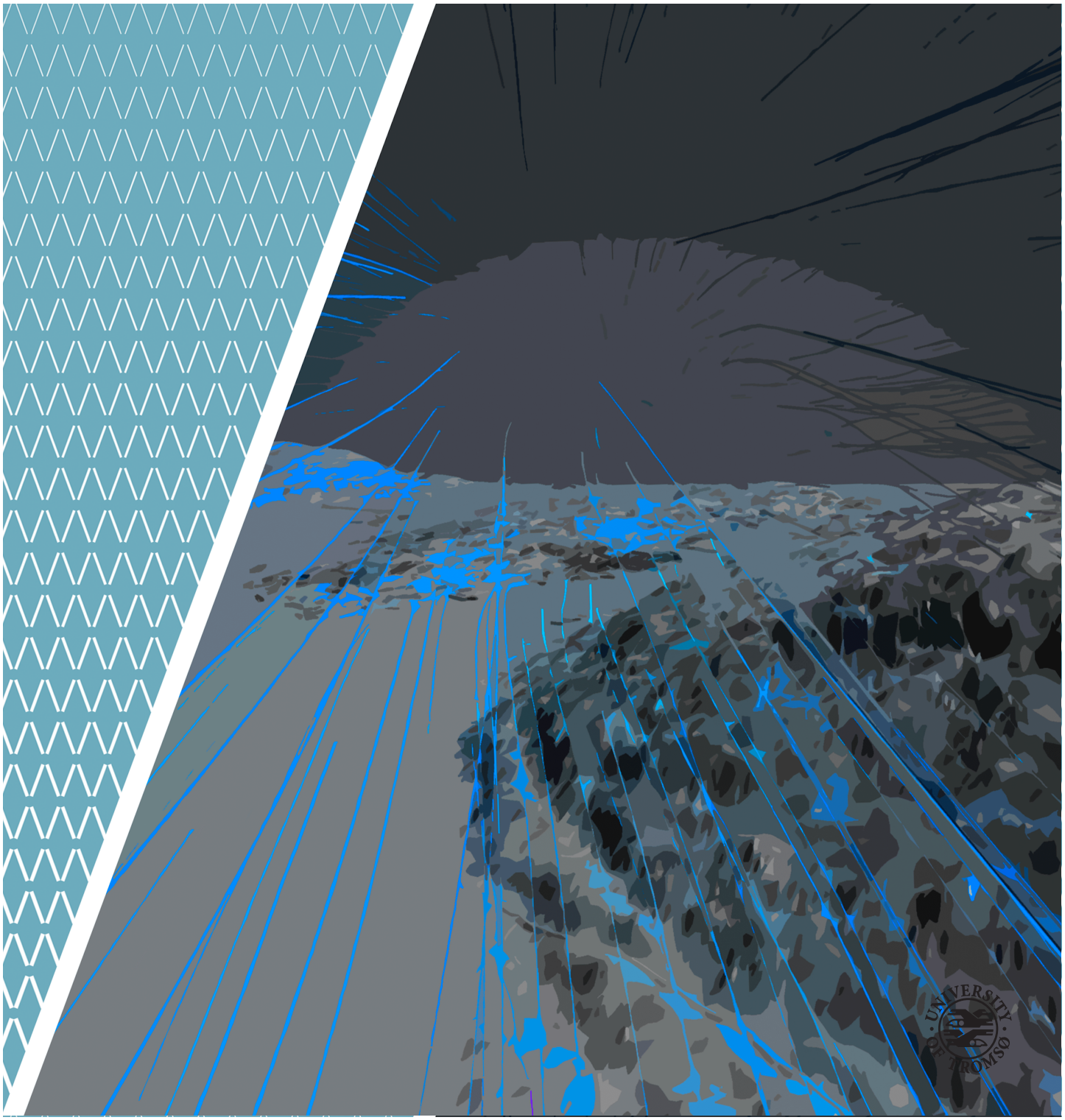

"Electric power is everywhere present in unlimited quantities
and can drive the world's machinery without the need of
coal, oil, gas, or any other of the common fuels."
–Nikola Tesla, 1933

Abstract

Making energy clean, reliable and readily available is essential for fighting climate change and to supply an ever-rising global power demand. The aim of the study is to identify optimal locations for a wind turbine to be joined to a small-scale hybrid system at the main campus of UiT – The Arctic University of Norway. To identify feasible areas for maximizing electric power production, techniques originating from two quite different disciplines are utilized: Geographical Information System and Computational Fluid Dynamics. Local weather data and detailed 3D-models are used as inputs to the wind simulations. Two optimal wind turbine locations are proposed with the following UTM-33N coordinates: (654053 – 7735418) at Realfagsbygget and (653410 - 7736185) at Grønnåsen. To further study the power production capability at Grønnåsen wind sensors were installed in the Avinor mast, 200 m east of the suggested optimal location. Here the average wind speed and power density at 21 m above ground level was calculated to be 4.22 m/s and 135.4 W/m^2 corresponding to the period of mid-February to mid-May 2017. For both the suggested optimal locations of a wind turbine, more weather data is necessary to accurately estimate the annual wind speed and power density averages.

Contents

Abstract **iii**

List of Figures **ix**

List of Tables **xiii**

Acknowledgements **xv**

Abbreviations **xvii**

Nomenclature **xix**

1 Introduction **1**
1.1 Background 1
1.2 Objectives 2
1.3 Significance 3
1.4 Structure of the Thesis 4

2 Theoretical Background **5**
2.1 Wind Physics 5
2.1.1 Source of Wind 5
2.1.2 Vertical Wind Shear 7
2.1.3 Turbulence 8
2.2 Generating Electricity from Wind Energy 10
2.2.1 Power in the Wind 10
2.2.2 Wind Turbines 11
2.2.3 Betz' Limit 13
2.2.4 Power Curve 13
2.3 Computational Fluid Dynamics 15
2.3.1 General Introduction 15
2.3.2 Governing Equations 16
2.3.3 Discretization Methods 28
2.3.4 Turbulence Models 29
2.3.5 Boundary Conditions 31

2.4 Geographical Information System 33
2.4.1 General Introduction 33
2.4.2 Acquiring Data 33
2.4.3 Universal Transverse Mercator 34
2.4.4 Digital Elevation Model 35
2.4.5 Triangulated Irregular Network 40

3 Methodology **43**
3.1 Weather Data 43
3.1.1 General Introduction 43
3.1.2 Bioforsk Weather Station, Holt 44
3.1.3 Realfagsbygget Weather Station, Breivika 45
3.1.4 Avinor Mast, Grønnåsen 45
3.1.5 Explanations of the Plots 49
3.2 3D-models 51
3.2.1 General Introduction 51
3.2.2 Tromsøya and Surrounding Area 51
3.2.3 Campus 55
3.2.4 Grønnåsen and Surrounding Area 57
3.3 Autodesk Flow Design 60
3.3.1 General Introduction 60
3.3.2 Visualization Methods 60
3.3.3 Boundary Conditions 65
3.4 AWS Truepower - Openwind 66
3.4.1 Background 66
3.4.2 Setup and Limitations 66

4 Results **69**
4.1 Weather Data 69
4.1.1 Holt 69
4.1.2 Realfagsbygget 72
4.1.3 Grønnåsen 74
4.1.4 Comparison of the Data Sets 76
4.2 Flow Simulations 80
4.2.1 Tromsøya 80
4.2.2 Realfagsbygget 85
4.2.3 Grønnåsen 90
4.2.4 AWS Truepower - Openwind 93
4.2.5 Comparison of the Simulations 95

5 Discussion **97**
5.1 Choice of Computer Tools 97
5.1.1 Building the 3D-models 97
5.1.2 Flow Simulation 98

5.2 Weather Data Reliability 99
5.2.1 Realfagsbygget 99
5.2.2 Grønnåsen 101
5.3 Deciding Parameter Values for Simulation 103
5.3.1 Inlet Wind Speed 103
5.3.2 Inlet Wind Direction 103
5.4 Simulation Reliability 104
5.4.1 Validity of the 3D-models 104
5.4.2 Resolution 105
5.4.3 Simulated Results 106
5.5 Optimal Placement of Wind Turbines 107
5.5.1 Realfagsbygget 107
5.5.2 Grønnåsen 109
5.6 Wind Power Density Estimations 111

6 Conclusion **115**
6.1 Summary 115
6.2 Concluding Remarks 117
6.3 Future Work 118

Appendices **121**

A Importing Data from Sensors at Grønnåsen **123**

B Additional Plots of Weather Data **125**
B.1 Holt 126
B.2 Realfagsbygget 127

C Openwind - Additional Simulations **129**
C.1 Wind speed distributions from different directions 130

D Sources of Data **133**
D.1 Public 133
D.2 Non-public 134

Bibliography **135**

List of Figures

2.1 Source of wind 6
2.2 Global wind patterns 6
2.3 Wake vortex produced by the passage of an aircraft wing . . 9
2.4 Typical structure of a horizontal-axis wind turbine 11
2.5 Working mechanism of most modern wind turbines 12
2.6 Examples of wind turbines with different axis of rotation . . 12
2.7 Wind flow through a turbine 13
2.8 Powercurve of a typical wind turbine 14
2.9 Low-pressure system over Iceland 15
2.10 Finite control volume approach 17
2.11 Infinitesimal fluid element approach 17
2.12 Flow chart showing alternatives to forming a complete set of equations 24
2.13 Finite control volume approach fixed in space 29
2.14 Grid arrangement at boundaries 31
2.15 Passive and active sensors in remote sensing 33
2.16 UTM zones and projection method 34
2.17 DEM produced using photogrammetry, northern region of Troms County 35
2.18 Difference between DSM and DTM 36
2.19 Producing DEMs through photogrammetry 37
2.20 LIDAR pulse recording multiple signal returns 38
2.21 Airborne scanning LIDAR system 39
2.22 The empty circumcircle principle for Delaunay triangulation, 2D 41
2.23 TINs generated with 3D Delaunay triangulation 41

3.1 Used weather data origin, Tromsø 43
3.2 Bioforsk weather station, Holt 44
3.3 Realfagbygget weather station, Breivika 45
3.4 Connection to the data logger 47
3.5 Data logger suitcase 47
3.6 Avinor mast, Grønnåsen 48
3.7 Wind sensors placement in the mast 48

3.8 Tromsøya 3D-model and its origin 51
3.9 Tromsøya 3D-model from different angles 53
3.10 Triangulated irregular network 54
3.11 Campus 3D-model 1 55
3.12 Campus 3D-model 2 56
3.13 Grønnåsen 3D-model and its origin 57
3.14 LIDAR pointcloud 58
3.15 LIDAR classes example 59
3.16 1 m DTM of Tromsøya produced by LIDAR 59
3.17 Flow lines and vortices, 2D-sim. 60
3.18 Disadvantage, 2D-sim. 61
3.19 Flow lines, 3D-sim. 62
3.20 Velocity planes, 3D-sim. 62
3.21 Isosurfaces, 3D-sim. 63
3.22 Simulation window 64
3.23 Example scale 64
3.24 Virtual wind tunnel 66
3.25 Openwind DTM and wind rose 67

4.1 Distribution of wind speed at Holt, 2015 70
4.2 Wind rose from Holt, 2015 71
4.3 Distribution of wind speed at Realfagsbygget, 2015 72
4.4 Wind rose from Realfagsbygget, 2015 73
4.5 Distribution of wind speed at Grønnåsen, mid-February to mid-May 2017 74
4.6 Wind roses from Grønnåsen, mid-February to mid-May 2017 74
4.7 Wind power density at Grønnåsen, mid-February to mid-May 2017 75
4.8 Contour map of Tromsø with annual wind roses, 2015 76
4.9 Comparison of daily averaged wind speed at Grønnåsen and Holt, mid-February to mid-May 2017 78
4.10 Vertical wind profile predictions, at Grønnåsenat mid-February to mid-May 2017 79
4.11 Inlet velocity dependency, Tromsøya 81
4.12 Inlet direction dependency, Tromsøya 82
4.13 High-speed regions combined 83
4.14 Flow lines, Tromsøya 84
4.15 Inlet velocity dependency, Realfagsbygget 85
4.16 Inlet direction dependency, Realfagsbygget 86
4.17 High-speed regions combined, Realfagsbygget 87
4.18 Areas of separation and deflection, Realfagsbygget 88
4.19 Formation of turbulence, Realfagsbygget 89
4.20 Smoke flow lines, Realfagsbygget 89
4.21 Inlet velocity dependency, Grønnåsen 90

4.22 Inlet direction dependency, Grønnåsen 91
4.23 High-speed regions combined, Grønnåsen 92
4.24 Flow lines, Grønnåsen 92
4.25 Estimated annual distribution of wind speed averages 93
4.26 Estimated annual distribution of wind speed averages from 180° 94
4.27 Comparison of AFD and Openwind simulations 95

5.1 Turbulence evaluation at Realfagsbygget 100
5.2 Turbulence evaluation at Grønnåsen 102
5.3 Optimal placement of MWT at Realfagsbygget 108
5.4 Optimal placement of wind turbine at Grønnåsen 110
5.5 Wind power density estimations, weekly averaged values from 2015 111

B.1 Seasonal wind roses from Holt, 2015 126
B.2 Seasonal wind roses from Realfagsbygget, 2015 127

C.1 Estimated annual distribution of wind speed averages from different directions, at 20 m AGL 130
C.2 Estimated annual distribution of wind speed averages from different directions, at 50 m AGL 131

List of Tables

2.1 Typical values of the wind shear exponent 8

4.1 Wind speed averages and data set correlation (Pearson), mid-February to mid-May 2017 79

5.1 Typical simulation time to reach "stable state" 105

Acknowledgements

First and foremost, I would like to thank my supervisor professor Tobias Boström for offering me the opportunity to do this project and for providing valuable feedback even on parental leave.

I would like to express my gratitude to Avinor for sponsoring my thesis by allowing my sensors to be mounted in their mast at Grønnåsen, completely free of charge.

A big thanks goes to professor Rune Graversen for discussing fluid dynamics with me and his inspiring enthusiasm for the subject. Also, I would like to acknowledge my appreciation to my childhood friend, Thomas Aspmo, for suggesting using Autodesk Infraworks 360 to produce the 3D-models. Extensive and much appreciated proof reading has been conducted by my Canadian friend, Devin Clemens, for which I am forever grateful.

Multiple sources of data have been applied in this study and I would like to thank all the contributors providing non-public data, including: Department of Computer Science at UiT, Statsbygg, Norconsult section Arkitektstudio, Rambøll, Tromsø municipality, Statens Kartverk and Geodata AS.

To the staff at UiT – The Arctic Univerity of Norway and my fellow classmates: thank you for five years packed with long nights, inspiring lectures, enlightening discussions and most of all great joy and companionship. You are the best!

Finally, I would like to thank my parents and my sister for supporting my choice of career and for helping out when needed. For example, most recently for helping me move out of a completely stacked house when the landlord decided to start the process of demolishing the house the very same day I submitted my thesis.

Sincerely,

Trond-Ola Hågbo
Tromsø, June 2017

Abbreviations

AFD	Autodesk Flow Design
AGL	Above Ground Level
BC	Boundary Condition
CFD	Computational Fluid Dynamics
DEM	Digital Elevation Model
DNS	Direct Numerical Simulation
DSM	Digital Surface Model
DTM	Digital Terrain Model
FCV	Finite Control Volume
FDM	Finite Difference Method
FEM	Finite Element Method
FVM	Finite Volume Method
GIS	Geographical Information System
GPS	Global Positioning System
HAWT	Horizontal-axis wind turbine
IFE	Infinitesimal Fluid Element
IMU	Internal Measurement Unit
LES	Large Eddy Simulation
LIDAR	Light Detection and Ranging
m a.s.l.	Metres above sea level
MWT	Micro-wind Turbine
PDE	Partial Differential Equation
PV	Photovoltaic
RADAR	Radio Detection and Ranging
RANS	Reynolds-averaged Navier-Stokes
TIN	Triangulated Irregular Network
UTM	Universal Transverse Mercator
VAWT	Vertical-axis wind turbine
VWT	Virtual Wind Tunnel
WMS	Web Map Service

Nomenclature

In this thesis, vectors are denoted by bold, italic types and scalars in normal, italic types. Mathematical operators are in upright letters. The list below and on the next page are sorted alphabetically, first Latin symbols and then Greek ones.

Symbol	Description	Unit
A	Cross-section area	m^2
$\boldsymbol{b}$	General vector field	
C_p	Power coefficient	
c_v	Heat capacity at constant volume	
đC	Chemical composition	J
dI	Internal energy	J
đQ	Heat input	J
đW	Work done	J
E_k	Kinetic energy	J
$\boldsymbol{F}$	Force per unit volume	$\mathrm{N\,m^{-3}}$
$\boldsymbol{F_b}$	Body forces per unit volume	$\mathrm{N\,m^{-3}}$
$\boldsymbol{F_{b'}}$	Body forces per unit mass	$\mathrm{N\,kg^{-1}}$
$\boldsymbol{F_p}$	Pressure forces per unit volume	$\mathrm{N\,m^{-3}}$
$\boldsymbol{F_v}$	Viscous forces per unit volume	$\mathrm{N\,m^{-3}}$
$\boldsymbol{f}$	The Coriolis parameter	$\mathrm{rad\,s^{-1}}$
P	Power	$1\,\mathrm{J\,s^{-1}}$
p	Pressure	$1\,\mathrm{N\,m^{-2}}$
$\dot{Q}$	Rate of heating	$1\,\mathrm{J\,s^{-1}}$
R	Gas constant	
Re	Reynolds number	
T	Temperature	K
t	Time	s
$\boldsymbol{u}$	Two-dimensional (horizontal) velocity, (u,v)	$\mathrm{m\,s^{-1}}$
v	Scalar velocity	$\mathrm{m\,s^{-1}}$
$\boldsymbol{v}$	Three-dimensional velocity, (u,v,w)	$\mathrm{m\,s^{-1}}$
x, y, z	Cartesean coordinates	

Symbol	Description	Unit
α	$\alpha = 1/\rho$ is the specific volume	$\mathrm{m^3\,kg^{-1}}$
β	Wind shear exponent	
ϑ	Latitude	rad
μ	Viscosity	$\mathrm{N\,s\,m^{-2}}$
ν	Kinematic viscosity, μ/ρ	$\mathrm{m^2\,s^{-1}}$
ρ	Density	$\mathrm{kg\,m^{-3}}$
ϕ	General scalar field	
φ	General fluid property per unit mass	
$\mathbf{\Omega}$	Angular velocity	$\mathrm{rad\,s^{-1}}$

1 Introduction

1.1 Background

The world population continues to increase every year, along with the standard of living, particularly in developing nations. Consequently, the global energy demand has reached a record high and is predicted to follow the trend well into the future (IPCC 2007, 253).

As of today, fossil fuels are the prevailing source of energy (IPCC 2007, 253) and are used for a variety of applications, such as transportation, heating and electric power production. However, an ever-rising awareness of climate change and how it is affected by human energy consumption and its potentially devastating impact is leading to an increased focus on shifting from fossil fuels to renewable sources of energy.

Making energy clean, affordable, reliable and readily available is not just essential for fighting climate change, but also to provide electric power to areas without access to it. For example, a stand-alone hybrid system can be installed in remote areas without access to the power grid. It can provide affordable and reliable electricity enabling the community to use electric powered equipment and technology.

A stand-alone hybrid system includes one or more methods of electricity generation (such as a photovoltaic system (PV) and a wind turbine), energy storage (for example a battery bank) and regulation. The idea is that multiple sources of energy can provide a more reliable supply of electricity. For instance, wind power and PV are often complimentary sources of energy. For many locations, the peak production of PV is usually midday in the summer, while the power in the wind is often more evenly distributed in the day and stronger in the winter period.

Hybrid systems can also be connected directly to the grid which might be an effective solution for companies and private homes eager to produce their own renewable electricity while at the same time ensuring reliable power supply in periods of low production. When the electricity produced by the hybrid system exceeds the demand of the company or private home, it can be sold to the grid if the grid owner allows it. A scaled-up hybrid system can even be used solely as a power plant.

In conjunction with an increased focus on renewable energy, UiT – The Arctic University of Norway is currently in the process of erecting a small-scale hybrid system for research purposes. A PV system has already been installed and a battery bank is being constructed and is not yet operating as of June 2017. The next step is to add at least one wind turbine to the system.

1.2 Objectives

The aim of the study is to identify an optimal location for a wind turbine in the nearby area of the university campus. An optimal location is a place of frequently high wind speed where the operative blades of the wind turbine are placed in an area of little or no turbulence, maximizing the power production. Two potential regions for installing a wind turbine have already been identified; the roof of Realfagsbygget (The Science Building) and the Grønnåsen area, about 800 meters Northwest of Realfagsbygget. The behavior of the wind in these two areas is to be studied so that optimal placements are obtained.

If a wind turbine is placed at the roof of Realfagsbygget it is not going to be very big and falls into the category of micro-wind turbine (MWT) which is confined to a power capacity of less than 2.5 kW (Peacock 2008). The Grønnåsen area is deserted and more open compared to Realfagsbygget enabling for a bigger wind turbine to be erected and the university has ambitions for installing a wind turbine of up to 50 kW in size in the region.

To be able to identify feasible areas, techniques originating from two quite different disciplines are utilized and combined: Geographical Information System (GIS) and Computational Fluid Dynamic (CFD). GIS is used to obtain and process geographical data to produce reliable 3D-models. The next step is to use these models to simulate the behavior of the wind in the regions of interest in a CFD-based computer tool. To set realistic input parameters, such as wind speed and direction, relevant weather data have been gathered and analyzed.

1.3 Significance

The local wind conditions in many urban environments can fluctuate considerably within the day and seasonal variations are significant. The local conditions can be much different compared to neighboring areas as a result of the topography and nearby buildings. GIS and CFD are therefore necessary tools to be able to find the optimal location for a wind turbine in an urban environment.

The power produced by any type of wind mill can be described by the equation:

$$P = \frac{1}{2}\, c_p\, \rho\, A\, v^3 \tag{1.1}$$

Here P is the power produced by a wind turbine, c_p is the power coefficient (limited by the Betz limit of $\frac{16}{27} \approx 0.59$), ρ is the density of the air, A is the cross-section area of the passing air and v is the wind speed.

As equation (1.1) illustrates, the power produced is highly dependent on the wind speed as it is cubed. Small speed reductions cause significant loss in power. Therefore, pinpointing a turbine location of feasible wind speed is vital for ensuring maximum power production.

An annual wind speed average of 6.5 m/s is considered by the Norwegian Ministry of Petroleum and Energy to be the lower limit to produce commercially viable wind power (Norwegian Ministry of Petroleum and Energy 2015, 28). Therefore, a location of an approximate annual wind speed average of 6.5 m/s or more is sought to locate.

1.4 Structure of the Thesis

This thesis is comprised of 6 chapters, including the introduction.

Chapter 2 provides the theoretical background for the methods used in this thesis. The chapter holds a short introduction to the working principles of wind turbines and more elaborated parts describing CFD and GIS.

Chapter 3 presents the methodology. It describes the weather data sites used, explains the production process of the 3D-models used and demonstrates the simulation tools applied.

Chapter 4 contains the results of the weather data analysis and presents the most important findings in the wind simulations. A comparison of the weather data and also the simulations is provided in this chapter.

Chapter 5 holds a discussion of the results validity and the choice of methods. In the end of this chapter, the optimal placements of a wind turbine are debated and presented.

Chapter 6 summarizes the results and proposes future work for extension and further improvements of the study.

Additional information is added in the appendix and includes a guide to import data from sensors at Grønnåsen, supplementary weather data analysis and simulation results. Also, a list of the sources of data is provided in the end.

2

Theoretical Background

2.1 Wind Physics

2.1.1 Source of Wind

The origins of wind power lie in the solar radiation emitted from the Sun. The radiation makes its way to Earth where it heats up the surface of the planet which in turn heats the surrounding air. Air temperature gradients arise as the radiation is absorbed unevenly across the globe and the gained heat is conducted to the surrounding air at different rates. The share of radiation being absorbed is highly dependent on the properties of the local surface materials. For example, dry snow reflects almost all the radiation whilst the ocean absorbs most of it. The measurement denoting the reflectance of the entire spectrum of solar radiation is called “albedo”, it is a dimensionless unit and an albedo of 1 corresponds to all the radiation being absorbed.

Higher temperature air has a lower density which causes it to rise above lower temperature air. The process is called convection and causes horizontal pressure gradients as the total weight of a vertically orientated column of hot air is less than a column of the same size and orientation, but of lower temperature. During the process of natural air pressure stabilization, the air flows from high pressure regions towards low pressure regions causing wind. The process is simplified in figure 2.5, bearing in mind that it is continuous, all the steps are occurring at the same time and are dependent on each other.

Figure 2.1: Source of wind

Annually Earth's surface at low latitude areas receives and absorbs more radiation compared to areas closer to the poles which induces a global energy transfer of warm air towards the North and the South poles. It may seem that the global energy transfer of warm air occurs as a result of two big convection cells radiating from the equator to the poles. However, this is not the case, mainly due to the rotation of the Earth and the cooling of the air. Instead, there are three sets of convection cells illustrated in figure 2.2; they are known as the Headley cells, the Ferrel cells and the Polar cells.

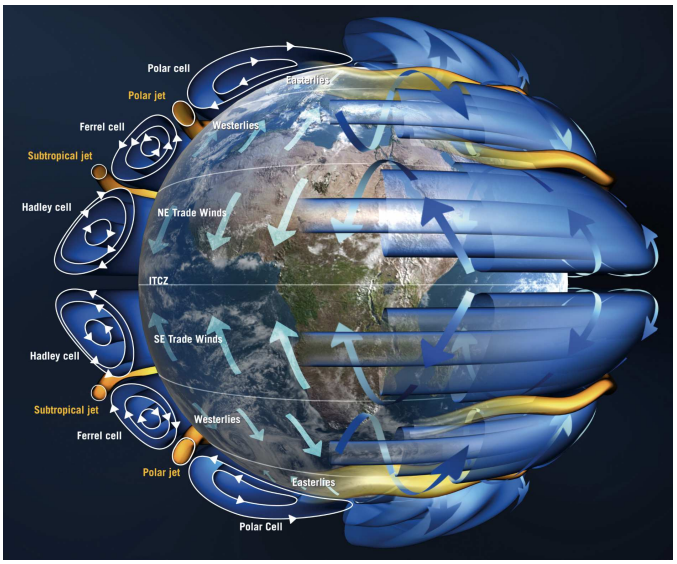

Figure 2.2: Global wind patterns (not to scale) (ESA 2004)

The rotation causes the wind (and water currents) to bend to the right relative to their direction in the Northern Hemisphere and to the left in the Southern Hemisphere. We call this fictitious force bending the flow the Coriolis force. As mentioned, the air naturally flows from high pressure to low pressure areas, but due to the bending it cannot go in a straight line. It keeps missing the target, just like satellites keep missing when falling towards the ground as the horizontal velocity is too high. In the Northern Hemisphere, the wind flows counterclockwise around a low-pressure system and clockwise for the same system in the Southern Hemisphere.

About 1-2 % of global incident solar radiation is converted into wind (Andrews and Jelly 2007, 100). It may not sound like that much, but it adds up to $\sim 10^{15}\ W$ – some 100 times the global power usage (Andrews and Jelly 2007, 100).

Wind energy is not evenly distributed across the globe and may vary significantly with the seasons. For instance, winter winds are typically stronger as the temperature differences from the Equator to lower latitudes (at the winter side) are greater, causing amplified pressure differences. Also, moving cells are constantly changing in shape and size as a result of weather related fluctuations.The direction of the wind at ground level is highly dependent on local conditions, such as the terrain, and small, high or low pressure systems. The described variations imply that a statistical analysis of the wind must be conducted to describe its behavior over time at a location.

2.1.2 Vertical Wind Shear

The wind speed usually increases with height all the way from the ground surface level to the end of the troposphere. A central cause is that the air flowing near the ground is slowed down by friction. The wind speed at elevations not directly in contact with the ground or any obstacles, like buildings or mountains, will also be affected as friction arises between layers flowing at different velocities.

The power law for wind shear is a commonly used equation for estimating the wind speed at different elevations based on known wind speed at a certain elevation for engineering applications (Nelson 2009, 37):

$$v = v_0\left(\frac{H}{H_0}\right)^{\beta} \tag{2.1}$$

v is the unknown wind speed at height H, v_0 is the measured wind speed average at the reference height H_0. β is the wind shear exponent.

The wind shear exponent, β, depends on many factors, such as atmospheric conditions and terrain roughness. The best way to determine β at a location is to measure the speed at two different heights and then calculate it using equation 2.1. Table 2.1 shows typical values of the exponent in different conditions and types of landscape:

Stability	Open water surface	Flat, open coast	Cities, villages
Unstable	0.06	0.11	0.27
Neutral	0.10	0.16	0.34
Stable	0.27	0.40	0.60

Table 2.1: Typical values of the wind shear exponent (Kaltschmitt et al. 2007, 55)

2.1.3 Turbulence

Reynolds Number

Turbulence is a generic term for any flow characterized by chaotic or unstable changes in pressure and velocity fields. A turbulent flow occurs when the inertial forces dominates the viscous forces within the fluid itself and the relation between the forces is often expressed by the dimensionless Reynolds Number *Re*. A low number indicates a laminar flow and a high number implies turbulent fluid behavior.

As the inertial and the viscous forces are described by the momentum equation, later derived in section 2.3.2, the relation between the forces is found by scaling a general form of the momentum equation:

$$\underbrace{\frac{\partial \boldsymbol{v}}{\partial t}}_{U/T} + \underbrace{(\boldsymbol{v} \cdot \nabla)\boldsymbol{v}}_{U^2/L} = \underbrace{-\frac{1}{\rho}\nabla p}_{\Phi/L} + \underbrace{\nu \nabla^2 \boldsymbol{v}}_{\nu U/L^2} \tag{2.2}$$

Inertial forces — Viscous forces

$\boldsymbol{v}$ is three-dimensional velocity (u, v, w), ρ is the density, p is pressure and $\nu \equiv \mu/\rho$ is the kinematic viscosity. Here U is the typical scale for the velocity, T is the time scale, L is the length scale and Φ is the scale of pressure deviation.

Now the scaled ratio, namely the Reynolds number, can be expressed as:

$$Re \equiv \frac{UL}{\nu} \tag{2.3}$$

Turbulent Eddies and Vortices

Turbulent flow is highly complex and chaotic, but some patterns are often recognizable. Examples are turbulent eddies and vortices. They appear in many sizes interacting with each other and cause increased friction which may result in the mixing of the fluid parcels, temperature increase, drag and lift forces acting on objects.

An eddy is the swirling of a fluid backwards toward the opposite direction of the general flow and often decays to smaller eddies forming a turbulent cascade. Vortices are similar, but often more stable structures and do not have to be caused by turbulence at all. An example is the flow around a low-pressure region as a product of near geostrophic balance induced by the Coriolis force. A vortex is a region of concentrated vorticity and can be stationary, move in space as well as change in size, shape, and strength.

Figure 2.3: Wake vortex produced by the passage of an aircraft wing (NASA 1990)

2.2 Generating Electricity from Wind Energy

2.2.1 Power in the Wind

When deriving the equation for the power in the wind it is natural to start with the energy it holds. Here we are only interested in kinetic energy, as it is what is utilized by wind turbines to be converted into mechanical energy and later electrical energy by exploiting the Faraday Effect. The kinetic energy E_k:

$$E_k = \frac{1}{2}\, m\, v^2 \tag{2.4}$$

m is mass and v is the scalar velocity of the wind.

The power P is simply the energy per unit time, hence:

$$P = \frac{\mathrm{d}E_k}{\mathrm{d}t} = \frac{1}{2}\, v^2 \underbrace{\frac{\mathrm{d}m}{\mathrm{d}t}}_{\substack{\text{mass}\\ \text{flux}}} \tag{2.5}$$

The mass flux is the total mass of all the particles in the flow passing an area in a given period of time. Therefore $\frac{dm}{dt}$ can be written as:

$$\frac{\mathrm{d}m}{\mathrm{d}t} = \rho\, A\, v \tag{2.6}$$

A is the cross-section area of the flow.

Substituting equation 2.6 into equation 2.5 gives:

$$P = \frac{1}{2}\rho\, A\, v^3 \tag{2.7}$$

Note that the power in the wind is highly dependent on its velocity. Doubling the velocity increases the power by a factor of 8 as v in equation 2.7 is cubed.

2.2.2 Wind Turbines

A Brief Introduction

Detailed information about the working mechanism of wind turbines is readily available and will not be provided as it is not in the scope of this thesis. However, a brief introduction follows on the next few pages. Figure 2.4 shows the structure and components of a typical modern horizontal-axis wind turbine (HAWT).

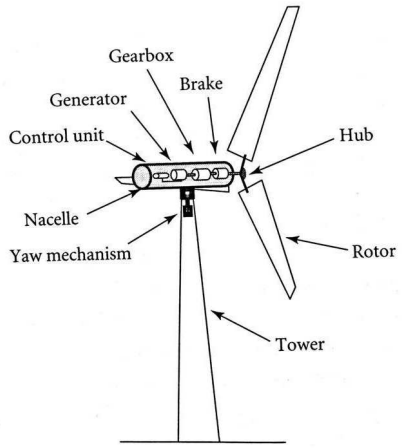

Figure 2.4: Typical structure of a horizontal-axis wind turbine (Andrews and Jelly 2007, 103)

Wind turbines are designed to use the kinetic energy in the wind to rotate their blades thus converting the kinetic energy into mechanical energy. The wind causes the blades to rotate and power the turbines due to their shape. They are shaped much like a wing of an airplane making the wind flow faster over one side of the wing compared to the other side. The resulting uneven velocity field creates a lift force driving the rotation of the turbine. It can be explained by the Bernoulli principle stating that when the velocity of a fluid increases consequently the pressure decreases. Therefore, a net pressure force is exerted onto the wing pushing it in the direction of the rotation.

The rotation cannot be directly coupled to a generator as wind turbine blades typically turn at a very low rate due to the issues of noise and mechanical strain. To achieve a more useful frequency is the rotor connected to a gearbox which increases its angular velocity. Inside the generator are magnets attached to the end of the rotor surrounded by coils of copper wire. Electromagnetic induction is generated when the rotor spins around inside the generator converting some of its mechanical energy into electrical energy.

Before delivering the electrical energy to the power grid or a stand-alone power system the voltage is usually ramped up in a high voltage step-up transformer. When ramping up the voltage the current drops proportionally. It reduces the power loss in lines as power loss increases with the current squared. In a stand-alone system, the distances are small compared to distances in the grid and a step-up transformer may not even be necessary depending on the voltage and current delivered by the wind turbine and the specifications of the other components in the system.

The basic working mechanism of most modern wind turbines can be summarized in the steps illustrated in figure 2.5.

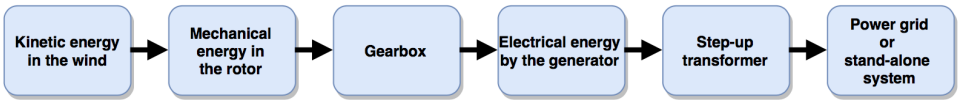

Figure 2.5: Working mechanism of most modern wind turbines

There are many different types of wind turbines available today. The most common ones have a horizontal axis of rotation. They usually have the gearbox, generator and other important components located inside the nacelle high in the air with the step-up transformer either located inside the nacelle as well or placed in the bottom of the tower at ground level. Vertical-axis wind turbines (VAWTs) differ in that they often have most of their heavy equipment at ground level which allows for simple installation and maintenance of turbines. Figure 2.6 shows two examples of wind turbines of different axes of rotation. The one with the vertical axis is a type called the Darrieus.

(a) Horizontal-axis (Tookapic 2005)

(b) Vertical-axis (Wikimedia 2005)

Figure 2.6: Examples of wind turbines with different axis of rotation

2.2.3 Betz' Limit

Not all the power in the wind can be extracted by a stationary wind turbine. The reason is intuitive and as follows: if all the kinetic energy in a moving fluid parcel was withdrawn, its downstream velocity would be zero, preventing other air parcels to pass. Instead, the velocity is only reduced, and because of continuum the cross-section area of the flow will increase as shown in figure 2.7.

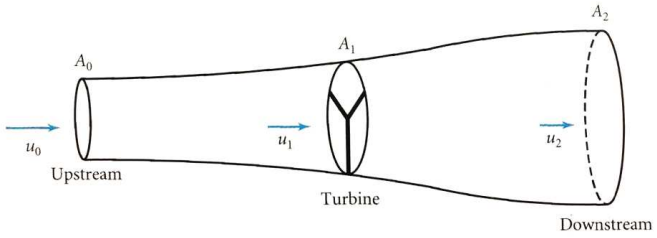

Figure 2.7: Wind flow through a turbine (Andrews and Jelly 2007, 105)

Betz' limit is the theoretical maximum that any stationary wind turbine can harvest and can be derived by applying the conservation of mass and momentum to the case illustrated in figure 2.7. Hence, the Betz' limit describing the maximum power coefficient of an ideal wind turbine is:

$$C_{p,max} = \frac{P_{optimal}}{P_{potential}} = \frac{16}{27} \approx 59.3\ \% \tag{2.8}$$

2.2.4 Power Curve

The power in the wind increases significantly with rising wind speed, as made clear in equation 2.7. A wind turbine is not able to harness all the available energy and would only under the most ideal and theoretical circumstances reach the maximum efficiency limited by the Betz' Limit of approximately 59.3 %.

Figure 2.8 illustrates a typical delivered power curve of a modern wind turbine. Both axes are linear without any values except for the zeroes. The lack of values on the axes are to illustrate the shape of the curve of any turbine as they look similar, but obviously has quite different power output depending on the size of the turbine. The cut-in speed is the minimum wind speed the turbine needs to be able to withdraw any energy of the slowly spinning rotor without stopping its movement entirely. At some wind speed, u_{rated}, the turbine reaches its

maximum generation capacity and the power is denoted as P_{rated}. If the wind speed increases the turbine is not able to generate additional power.

At an even higher wind speed, the turbine will turn on its brake and pitch its rotor blades to stall the movement of the rotor and stop the generation of electricity. Braking and pitching the rotor blades prevents the thrust force from damaging the turbine. The corresponding speed is called the cut-out speed.

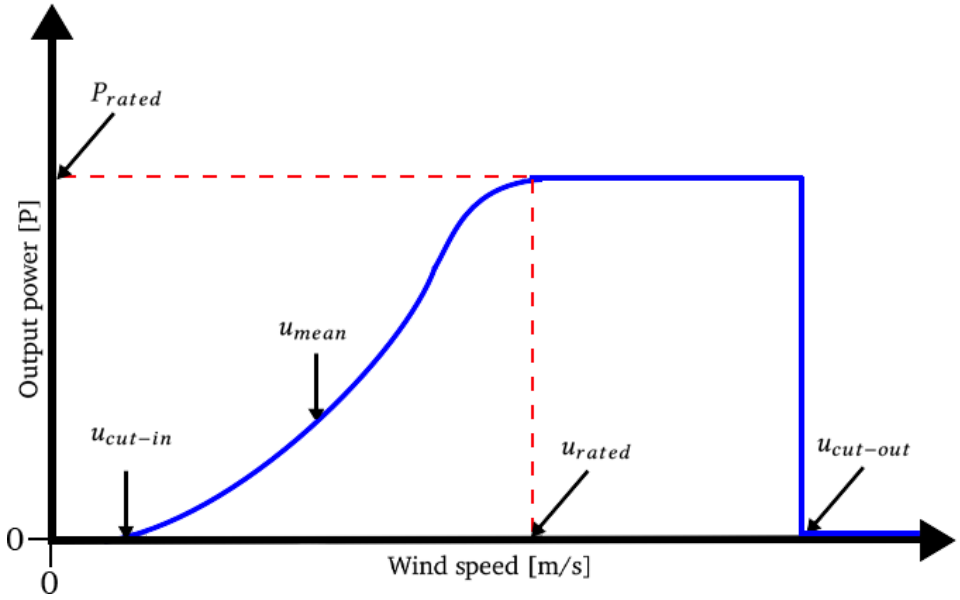

Figure 2.8: Powercurve of a typical wind turbine

2.3 Computational Fluid Dynamics

2.3.1 General Introduction

Computational Fluid Dynamics, commonly referred to as CFD, is a branch within the field of fluid mechanics utilizing computational power to analyze and predict fluid flow behavior. CFD-software uses a variety of different numerical methods and algorithms, all designed to solve versions of the same set of governing equations. Describing the equations and how they are tackled by CFD is the aim of this section of the theoretical background.

The inclusion of written explanations of differing equations may seem confusing and unnecessary - fluid flows are after all governed by the same laws - but the equations are often separated by simple and numerical analysis, resulting in differing set versions used for specific cases.

An example of a common simplification is neglecting the Coriolis force. The Coriolis force is called a fictitious force as it is the result of a rotating frame of reference, such as Earth. Even though it is fictitious it still has real impact. It plays a central role in the energy flow from the tropical zone towards the poles and is responsible for the vortices of low-pressure systems typically seen in a common weather report. Figure 2.9 is an example of such a vortex spinning counterclockwise and is a result of near geostrophic balance, meaning that Coriolis almost manages to balance the pressure gradient force in the momentum equation. Coriolis is often neglected when simulating fluid behavior on a local scale as the global energy transfer is not of importance and the bending is small compared to other movement.

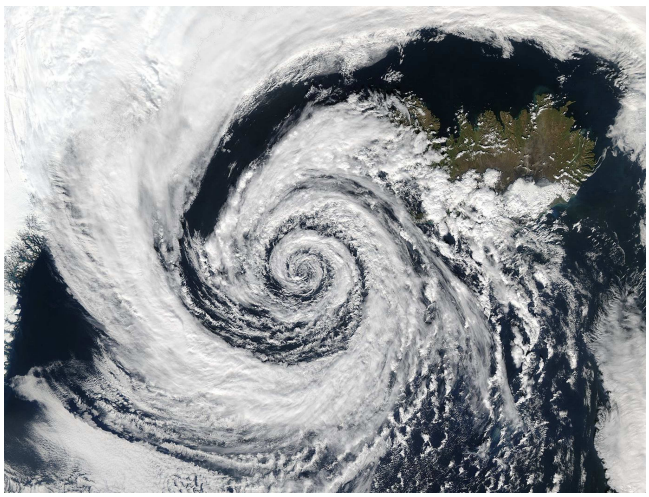

Figure 2.9: Low-pressure system over Iceland (NASA, 2003)

Fluid flow is governed by three fundamental laws; conservation of mass, Newton's second law of motion and conservation of energy. These laws are usually expressed as partial differential equations and will be explained further in section 2.3.2. CFD attempts to solve these equations numerically in space and time with the desired accuracy in a cost-efficient way - using as little computational power needed to attain satisfactory results.

In addition to deciding the set of equations that represent the fundamental laws of fluid dynamics, there are also other essential options for consideration. One of them is the method of discretization. For any numerical method to work, the system of equations needs to be made discreet. More about this process is found in section 2.3.3. Another choice to consider is the turbulence model. There are a variety of turbulence models to choose from with different features. Perhaps the most decisive choices to get right are the boundary conditions. When considering the best option for the mode of analysis of any given problem, it is necessary to consider many factors, such as the time and length scales to be simulated and the computational power available.

2.3.2 Governing Equations

Approach to deriving the equations

A common starting point when deriving equations is to link them to the relevant fundamental laws of physics. As mentioned before, for fluid dynamics those are: the conservation of mass, Newton's second law of motion and conservation of energy.

The next step is to apply the laws of physics to a suitable model of the flow, such as Finite Control Volume (FCV) or Infinitesimal Fluid Element (IFE), then extract the equations derived from them. Both are commonly used in CFD and are seen respectively in figures 2.10 and 2.11. (Wendt 2009, 15-18)

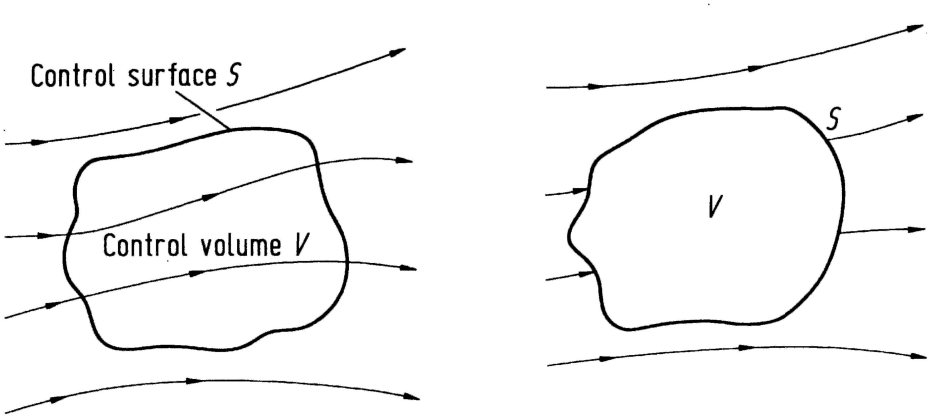

Figure 2.10: Finite control volume approach (Wendt 2009, 17)

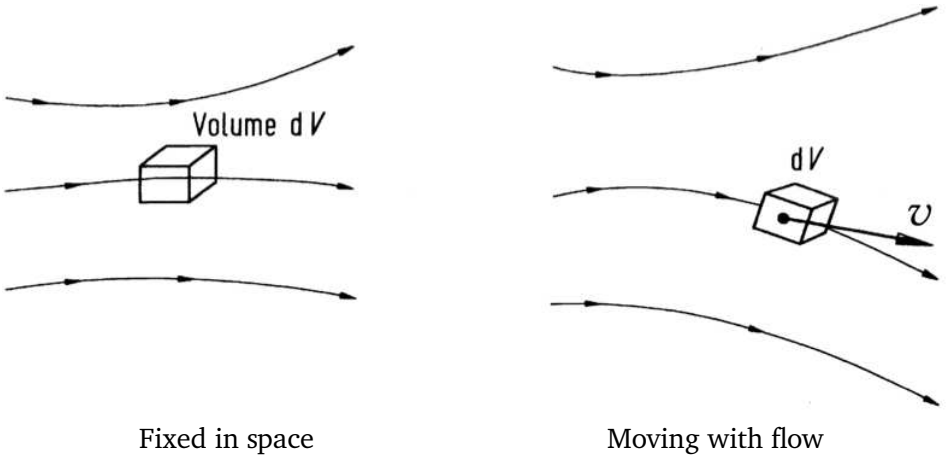

Figure 2.11: Infinitesimal fluid element approach (modified) (Wendt 2009, 17)

The FCV examines a closed and reasonably large region of the flow of constant size, a more precisely constant volume. The IFE differs as it is much smaller and can change in size, but is a fluid element of constant mass. They can both be either fixed in space or moving with the flow. (Wendt 2009, 16-18)

As expected, the two approaches will set up their initial equations quite differently. However, through a comprehensive analytical process they could both be rewritten to the very same two sets of equations. Both the models are equally valid representations of the flow, the only vital difference is the coordinate system we want the system to be expressed in, a fixed one or moving with the flow.

One of the sets consists of conservative equations and is obtained by either the FCV or the IFE being fixed in space as they are on the left-hand side of both figures. The other set contains non-conservative equations and is correspondingly obtained by either the FCV or the IFE moving with the flow as they are on the right-hand side of both figures, figure 2.10 and 2.11. The two sets are equally valid and will not affect the results in any problem solved analytically. However, as CFD solves the equations numerically in discretized form, solving the two sets could give different results and choosing the right set for the problem is therefore crucial to achieve reliable calculations. (Wendt 2009, 15-18)

Conservative versus Non-Conservative Set

As the name suggests, the non-conservative set is not quite able to conserve mass, energy and momentum when solved numerically. The problem is related to the splitting of the derivatives after being discretized, a problem not shared by the conservative set. To attempt to reduce the error, a certain amount of mass can be added or subtracted after every iteration.

The two sets have different practical applications depending on their advantages. As the non-conservative set is derived from a model following the flow, it is often more favorable to use when finding information about a fluid-parcel, such as its position or momentum. Following the motion is called the material point of view, or sometimes the Lagrangian view, and the associated equations involve usage of the material derivative. (Vallis 2006, 4)

The conservative set describes fluid behavior from a frame of reference fixed in space. It is often called the field view, or the Eulerian view, and is convenient when describing the local change of a field. The field of view refers to how dynamical variables evolve in space and time such as velocity, pressure and density. As the velocity field at a given location is particularly relevant to this study, CFD software that simulates fluid flow using a conservative set is preferential. For the same reason, the conservative equations are the only ones listed in the sections to come. (Vallis 2006, 4)

Conservation of Mass (continuity eqation)

The principle of conservation of mass is a conservation law. It states that in any closed system that does not allow for any transfer of matter in or out of the system that the total mass will remain constant over time. CFD is typically used to simulate how a fluid flows *through* a system. Conservation of mass is therefore applied using a continuity equation as it allows for fluid to flow in and out of regions and fluid density to change, so long as the total fluid flux of the system is zero.

Consider the case of a FCV fixed in space, also called an Eulerian CV, as illustrated on the left-hand side of figure 2.10. The FCV itself is of constant volume, not constant mass, but it does not mean that the principle of mass conservation cannot be applied to it. It follows that all the lost or gained mass of the FCV would have to leave or enter through its surface. Hence:

$$\text{Mass gain of FCV} = \text{Mass entering FCV} \tag{2.9}$$

As the FCV has a fixed volume, any mass gain/loss will result in increased/decreased density within itself. It can be expressed by integrating the density change within the entire volume V:

$$\text{Mass gain of FCV} = \int_V \frac{\partial \rho}{\partial t}\, dV \tag{2.10}$$

Where t is time.

Likewise, an expression for the fluid mass entering/leaving the FCV through surface $\boldsymbol{S}$ is:

$$\text{Mass entering FCV} = -\int_S \rho \boldsymbol{v} \cdot d\boldsymbol{S} \tag{2.11}$$

The minus sign comes from that the normal of the infinitesimal surface element $d\boldsymbol{S}$ is defined to point outwards in the opposite direction of the entering mass. To be able to simplify equation 2.9 after substituting in equation 2.10 and 2.11 it is convenient for the integrals to be of the same type. It can be achieved by rewriting equation 2.11 using the divergence theorem:

$$\text{Mass entering FCV} = -\int_S \rho \boldsymbol{v} \cdot d\boldsymbol{S} = -\int_V \nabla \cdot \left(\rho \boldsymbol{v}\right) dV \tag{2.12}$$

Now substituting equation 2.10 and 2.12 into equation 2.9 gives:

$$\int_V \frac{\partial \rho}{\partial t}\, dV + \int_V \nabla \cdot (\rho \boldsymbol{v})\, dV = 0$$

$$\int_V \left[\frac{\partial \rho}{\partial t} + \nabla \cdot (\rho \boldsymbol{v}) \right] dV = 0 \tag{2.13}$$

Since the FCV is arbitrarily chosen, the only way for the integral on the left-hand side of equation 2.13 to equal zero is for the integrand itself to be zero at every point inside the volume. The result is the continuity equation in conservation form:

$$\frac{\partial \rho}{\partial t} + \nabla \cdot (\rho \boldsymbol{v}) = 0 \tag{2.14}$$

Momentum equation (Navier-Stokes)

Applying Newton's second law to fluid motion, together with a couple of assumptions related to stress, gives the momentum equation. As the equation describes how a viscous flow responds to both internal and imposed forces in all the three spatial directions of Euclidean space, the equation can be written in component form giving a set of three equations commonly referred to as the Navier-Stokes equations. The equations are important for numerous study fields within physics and mathematics, and come in many varieties due to their wide applications. The solution of the conservative Navier–Stokes equations is a flow velocity field. (Wendt 2009, 27-33)

To show how the governing equations can be obtained from different models of the flow, the momentum equation will be derived using the IFE approach with a coordinate system moving with the IFE, as illustrated in the right-hand side of figure 2.11. Choosing a material point of view leads to the non-conservative version of the equation. Fortunately, it is not an issue as the conservative version is easily obtained by substituting in the definition of the material derivative after a while.

Before applying Newton's second law of motion to the IFE, a couple of properties of the material derivative need to be established.

The definition of the material derivative of a vector field $\boldsymbol{b}$ is:

$$\frac{\mathrm{D}\boldsymbol{b}}{\mathrm{D}t} = \underbrace{\frac{\partial b}{\partial t}}_{\substack{\text{local rate} \\ \text{of change}}} + \underbrace{(\boldsymbol{v} \cdot \nabla)\boldsymbol{b}}_{\textit{advection}} \tag{2.15}$$

The right-hand side of the equation is how the material derivative is expressed in a coordinate system fixed in space, called the field view or the Eulerian view.

The material derivative of a general fluid property φ multiplied with the mass of a fluid element:

$$\frac{\mathrm{D}}{\mathrm{D}t}(\varphi\rho\Delta V) = \rho\Delta V\frac{\mathrm{D}\varphi}{\mathrm{D}t} + \varphi\frac{\mathrm{D}}{\mathrm{D}t}(\rho\Delta V) \tag{2.16}$$

Applied to a fluid, Newton's second law of motion states that a fluid parcel's rate of change of momentum is equal to the force acting on it. By integrating the momentum-density field $\rho\boldsymbol{v}$ over the entire volume V of the IFE, its total momentum is expressed. Likewise, the net force acting on it is found by integrating the force per unit volume $\boldsymbol{F}$. Thus:

$$\frac{\mathrm{D}}{\mathrm{D}t}\int_V \rho\boldsymbol{v}\, dV = \int_V \boldsymbol{F}\, dV \tag{2.17}$$

Substituting fluid velocity $\boldsymbol{v}$ into equation 2.16 replacing the general fluid property φ gives:

$$\frac{\mathrm{D}}{\mathrm{D}t}(\boldsymbol{v}\rho\Delta V) = \rho\Delta V\frac{\mathrm{D}\boldsymbol{v}}{\mathrm{D}t} + \boldsymbol{v}\frac{\mathrm{D}}{\mathrm{D}t}(\rho\Delta V) \tag{2.18}$$

As $\rho\Delta V$ is simply the mass of the FE and because it is constant the second term on the right-hand side of equation 2.18 vanishes giving:

$$\frac{\mathrm{D}}{\mathrm{D}t}(\boldsymbol{v}\rho\Delta V) = \rho\Delta V\frac{\mathrm{D}\boldsymbol{v}}{\mathrm{D}t} \tag{2.19}$$

$$\frac{\mathrm{D}}{\mathrm{D}t}\int_V \boldsymbol{v}\rho\, dV = \int_V \rho\frac{\mathrm{D}\boldsymbol{v}}{\mathrm{D}t}\, dV \tag{2.20}$$

Equation 2.20 does NOT imply that density is time-independent even though ρ is moved outside the derivative, it is just a result of the mass of the IFE being time-independent.

Rewriting equation 2.17 using the property of the material derivative as presented in equation 2.20, gives:

$$\int_V \left(\rho \frac{\mathrm{D}\boldsymbol{v}}{\mathrm{D}t} - \boldsymbol{F} \right) dV = 0 \tag{2.21}$$

Just like for the continuity equation, the integrand must equal zero as the volume being integrated over is arbitrarily chosen. Hence:

$$\rho \frac{\mathrm{D}\boldsymbol{v}}{\mathrm{D}t} - \boldsymbol{F} = 0 \tag{2.22}$$

$\boldsymbol{F}$ consists of both external and internal forces. The external forces are often called the body forces, $\boldsymbol{F_b}$, and gravity is an example of such a force. Internal forces arise due to stress between the fluid parcels causing pressure and viscous forces represented by $\boldsymbol{F_p}$ and $\boldsymbol{F_v}$:

$$\frac{\mathrm{D}\boldsymbol{v}}{\mathrm{D}t} = -\frac{1}{\rho}\left(\boldsymbol{F_p} + \boldsymbol{F_v} + \boldsymbol{F_b} \right) \tag{2.23}$$

Deriving the expressions for the pressure and the viscosity forces could be quite lengthy and for this reason they are simply shown as they appear in the textbook "Atmospheric and Oceanic Fluid Dynamics" by Geoffrey K. Vallis.

The pressure force per unit volume can be shown to be (Vallis 2006, 12):

$$\boldsymbol{F_p} = -\nabla p \tag{2.24}$$

The minus sign arises as the pressure force is directed inwards, in the opposite direction of how the normal to the IFE's surface is defined.

Finding the viscosity force per unit volume is more complicated. For most liquids and gasses, it is approximately (Vallis 2006, 13):

$$\boldsymbol{F_v} \approx \mu \nabla^2 \boldsymbol{v} \tag{2.25}$$

Substituting equation 2.24 and 2.25 into equation 2.23 gives:

$$\frac{D\boldsymbol{v}}{Dt} = -\frac{1}{\rho}\nabla p + \nu\nabla^2\boldsymbol{v} + \boldsymbol{F_{b'}} \tag{2.26}$$

$\nu \equiv \mu/\rho$ is the kinematic viscosity and $\boldsymbol{F_{b'}}$ represents body forces per unit mass.

Now, the definition of the material derivative of a vector field, equation 2.15, is substituted in giving the conservative form of the momentum equation:

$$\frac{\partial\boldsymbol{v}}{\partial t} + (\boldsymbol{v}\cdot\nabla)\boldsymbol{v} = -\frac{1}{\rho}\nabla p + \nu\nabla^2\boldsymbol{v} + \boldsymbol{F_{b'}} \tag{2.27}$$

For the momentum equation to be accurate for a fluid in a rotating frame it must include the Coriolis-term and equation 2.27 becomes:

$$\frac{\partial\boldsymbol{v}}{\partial t} + (\boldsymbol{v}\cdot\nabla)\boldsymbol{v} + \boldsymbol{f}\times\boldsymbol{v} = -\frac{1}{\rho}\nabla p + \nu\nabla^2\boldsymbol{v} + \boldsymbol{F_{b'}} \tag{2.28}$$

$\boldsymbol{f} \equiv 2\Omega\, sin\vartheta$. $\boldsymbol{f}$ is the Coriolis parameter, Ω is the angular velocity and ϑ is the latitude.

Forming a Complete Set

So far, we have five unknown flow field variables (ρ, p, u, v and w), but only four equations. Therefore, additional information is required for solving the set. Three options of forming a complete set are illustrated in the flow chart below. A detailed explanation of the different options is not in the scope of this thesis, so only a brief explanation of the alternative solutions is provided below.

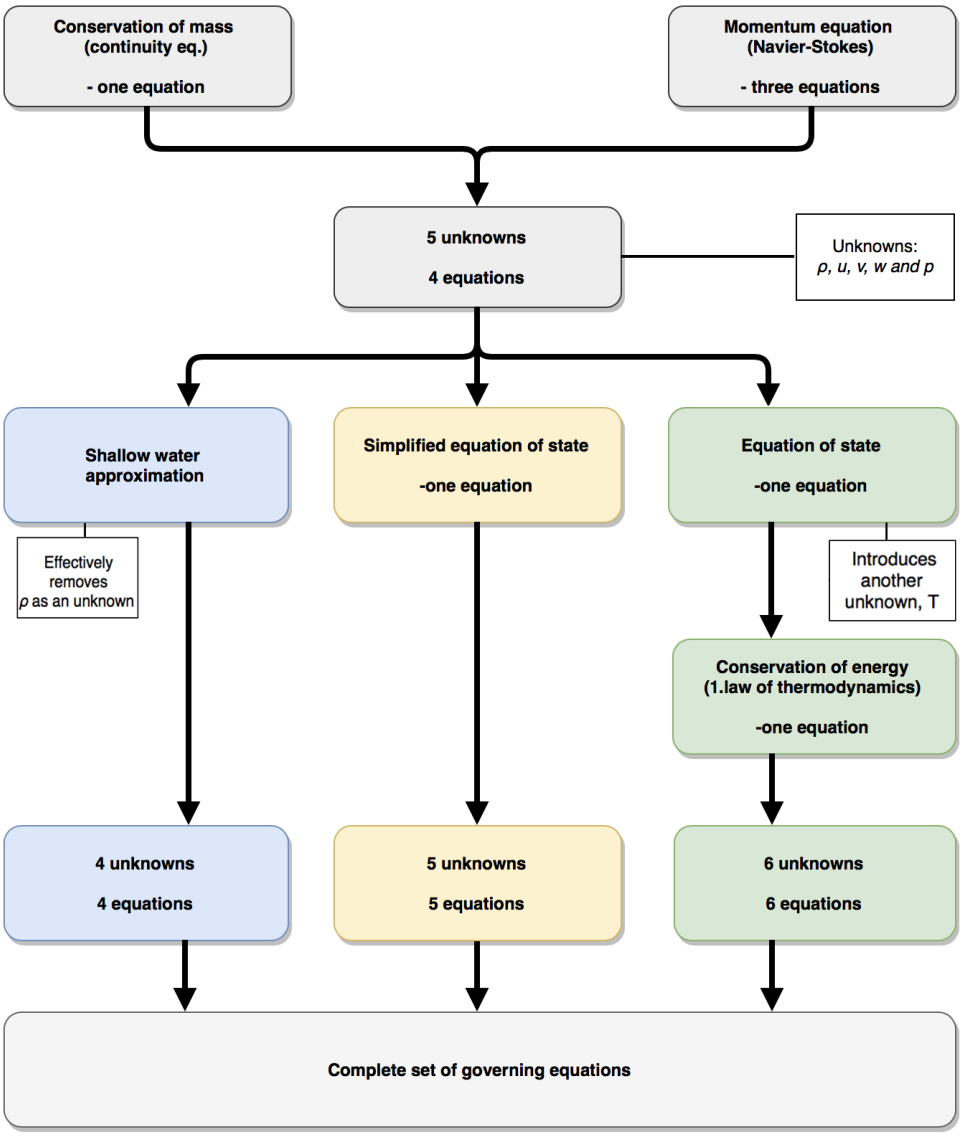

Figure 2.12: Flow chart showing alternatives to forming a complete set of equations

Shallow water approximation

Water is compressible, but the density variation is relatively small when comparing a fluid parcel on the surface to one at the bottom of the deepest ocean. Water is therefore often considered to be incompressible. The shallow water approximation applies to a fluid of constant density in which the flow's horizontal length scale is much greater that its vertical; hence, the water is "shallow". As the density is simplified to be constant, the continuity equation and the Navier-Stokes equations form a complete set. (Vallis 2006, 123)

Simplified equation of state
In the shallow water approximation, the density is constant. If the density is a function of pressure only, the fluid is said to be *barotropic* contrary to a *baroclinic* fluid in which the density is also affected for example by temperature and salinity. In a barotropic fluid the isolines of pressure and density are parallel, something that restricts the fluid movement significantly. As much of the movement in the atmosphere is caused by horizontal pressure differences it could in most cases considered not to be barotropic, but the ocean might be near barotropic. (Vallis 2006, 15)

Equation of state
The equation of state is not a fundamental law like conservation of mass and Newton's second law of motion, it is an empiric law. It means that it is not derived from an idea or a concept, but from observations and experiments. An equation of state relates thermodynamic state variables to each other. Earth's atmosphere is very close to being an ideal gas (Vallis 2006, 14), which is described by the equation of state for an ideal gas:

$$p = \rho RT \tag{2.29}$$

R is the gas constant.

Conservation of energy
As the equation of state introduces yet another unknown variable, T, an additional equation is required to form a complete set of equations. A solution is applying the fundamental principle of conservation of energy to a fluid flow. The law of conservation of energy states that the total energy of an isolated system remains constant as energy cannot be created nor destroyed. Nevertheless, the energy can change its form, for example going from potential energy to kinetic energy or vice versa.

Within a fluid parcel, the energy does not have to be conserved as it can flow in from or out to neighboring parcels, but the principle of energy conservation is applied through the 1^{st} law of thermodynamics. It states that the internal energy ($\mathrm{d}I$) of a body may change due to heat input ($đQ$), work done *by* the body ($đW$), or a change in chemical composition ($đC$), hence:

$$\mathrm{d}I = đQ - đW + đC \tag{2.30}$$

The bars over the differentials on the right-hand side symbolizes that they are imperfect differentials as Q, W and C are not functions of state, but fluxes of energy.

For a dry ideal gas the internal energy is a function of temperature only and $\mathrm{d}I = c_v \mathrm{d}T$. c_v is the heat capacity at constant volume. The work done is equal to the pressure times the change in its volume, so $đW = p\ \mathrm{d}\alpha$. $\alpha = 1/\rho$ is the specific volume of the fluid. In this study, chemical changes in composition are not considered, consequently $đC = 0$. Combining the listed information gives:

$$đQ = c_v \mathrm{d}T + p\ \mathrm{d}\alpha \tag{2.31}$$

Now it is time to include some derivatives so that a differential equation can be obtained. Choosing the Lagrangian view:

$$\dot{Q} = \frac{\mathrm{D}Q}{\mathrm{D}T} = c_v \frac{\mathrm{D}T}{\mathrm{D}t} + p\frac{\mathrm{D}\alpha}{\mathrm{D}t} \tag{2.32}$$

Here $\dot{Q}$ is the rate of heating.

A result of mass being conserved is that equation 2.32 can be written as:

$$\dot{Q} = c_v \frac{\mathrm{D}T}{\mathrm{D}t} + p\alpha\nabla \cdot \boldsymbol{v} \tag{2.33}$$

As the conservative version of the equation is preferred we want to modify the equation from having a material point of view to having a field view. The definition of the material derivative of a scalar field (ϕ) is:

$$\frac{\mathrm{D}\phi}{\mathrm{D}t} = \frac{\partial \phi}{\partial t} + \boldsymbol{v} \cdot \nabla\phi \tag{2.34}$$

Now substituting the definition into the equation 2.33 gives the conservative version of the energy conservation equation for a dry ideal gas:

$$\underbrace{\frac{\partial Q}{\partial t}}_{\substack{\text{local rate of}\\ \text{heating change}}} + \underbrace{\boldsymbol{v} \cdot \nabla Q}_{\substack{\text{heating}\\ \text{advection}}} = c_v \Bigg(\underbrace{\frac{\partial T}{\partial t}}_{\substack{\text{local rate of}\\ \text{temperature}\\ \text{change}}} + \underbrace{\boldsymbol{v} \cdot \nabla T}_{\substack{\text{temperature}\\ \text{advection}}} \Bigg) + \underbrace{p\alpha\nabla \cdot \boldsymbol{v}}_{\substack{\text{total rate}\\ \text{of change}\\ \text{in work}}} \tag{2.35}$$

Common simplifications of the set
A couple of simplifications are already mentioned and used in the described sets including the shallow water approximation, disregarding the Coriolis force in a rotating frame of reference and simplifying the atmosphere to be a dry ideal gas. Simplifications of the sets are made to reduce the computational costs while hoping to maintain the reliability of the simulations. Some simplifications may be considered reasonable in one specific case and not in another.

When deciding what simplifications to use it is vital to know the desired accuracy of the simulation and the computational power available. The next step is to evaluate the specific case of interest. A powerful tool is to make a typical time and length scale analysis for the case to see what terms in the governing equations will dominate the fluid flow behavior. Terms of lower order of magnitudes relative to the other terms in the equation are considered of lesser importance, and simplifications affecting only these terms can be carried out.

The Boussinesq approximation neglects any density variations except in terms multiplied with the gravitation and effectively reduces the nonlinearity of the problem. The approximation is not applicable to large-scale atmospheric simulations as the density of air changes significantly with height relative to its mean density. However, as water is often considered to be incompressible the set of Boussinesq equations can in many cases be used to simulate fluid flow in the ocean. Also, it is frequently used to solve non-isothermal flow, such as natural convection. (Vallis 2006, 67-73)

The anelastic approximation is similar to the Boussinesq, but instead of disregarding the density change entirely (except for in terms multiplied with gravity), it simplifies density to be a function of only height. For a stratified atmosphere, this representation of the density is quite accurate and the anelastic approximation could in many cases be adequate. (Vallis 2006, 73-77)

For many large-scale atmospheric flows the horizontal length scales is far greater than the vertical ones. In these cases a common simplification is to assume the atmosphere is in hydrostatic balance, meaning that the pressure gradient force perfectly balances the gravitational force resulting in no movement in the vertical direction. (Vallis 2006, 80–85)

2.3.3 Discretization Methods

Not including the equation of state, all other equations in the set are partial differential equations (PDEs) and need to be reformulated in a way that enables them to be solved numerically. The equations need to be made discreet; in other words, instead of solving for continuous space and time, calculations are made on a system of points in space with a certain time step between the calculations. There are a variety of ways of arranging these discreet points and the process of doing so is called discretization.

Perhaps the most known discretization methods commonly used by CFD are "Finite element method"(FEM), "Finite difference method"(FDM) and "Finite Volume Method"(FVM) (Wendt 2009, 87-88, 235-236). FEM divides the continuum field into cells, or elements, and does not look for the solution of the PDEs themselves, but the integral form of the equations (Wendt 2009, 235). FDM seeks to replace the partial derivatives with algebraic difference quotients yielding a system of equations solvable for the discreet points (Wendt 2009, 88). While the two previous methods have their applications in CFD, this study is primarily concerned with the use of FVM as it applies to the CFD-software used. A brief description of the method follows.

Finite Volume Method

The finite volume method is a common approach used in CFD and is known as a robust and cost-efficient method for the discretization of conservation laws, which are very important in fluid dynamics (Eymard et al. 2003, 9). Simply put, the approach is to divide the fluid flow into a mesh of discreet points of constant volumes. Each point is assigned one discrete unknown represented by one equation. Similar to the approach of FEM does FVM also discretize the integral form and not the differential form of the equations (Wendt 2009, 275). The equations hold a derivative of the unknowns which are replaced by a finite difference using Taylor expansion. (Eymard et al. 2003, 8-9)

The set of governing partial differential equations used in the FVM discretization is a conservative one. Therefore, the fluid flow modeled by CFD-software discretizing the set of equations with FVM is best viewed as the FCV fixed in space illustrated in the left side of figure 2.10 re-presented below. (Eymard et al. 2003, 4)

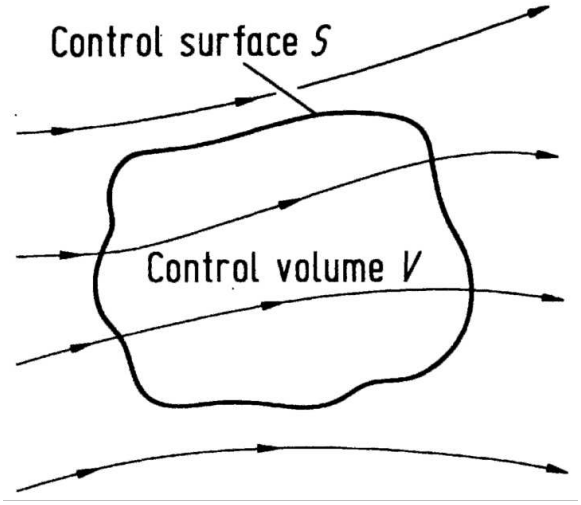

Figure 2.13: Finite control volume approach fixed in space (Wendt 2009, 17)

The best feature of FEM is the geometric flexibility while FDM's advantage is its flexibility when defining the discreet flow fields. FVM tries to combine these desired features, but does not fully succeed without issues. One example is that it has difficulties defining the derivatives in an accurate manner. Unlike in FDM, the grid is not necessarily represented orthogonally nor equally spaced. As such, an accurate definition of the derivative based on a Taylor expansion is impossible. (Wendt 2009, 278)

2.3.4 Turbulence Models

General Introduction

Laminar fluid behavior can often be predicted accurately without the need for considerable computational power. In fact, for some simplified cases the set of equations can even be completely solved analytically. Unfortunately, this is currently not the case for turbulent flows as the level of complexity is significantly higher. A high level of complexity equates to high computational costs, which is why the application of a turbulence model is effective.

Turbulent fluid behavior can be very chaotic, producing eddies on very different time and length scales. For many cases, it is not necessary to know exactly what happens on the smallest scales, but how the movement affects the fluid behavior on a bigger scale. A turbulence model works by estimating the influence that small scale turbulent movements have on the general fluid behavior.

There are a variety of turbulence models available today designed for many applications. A few common types are the Reynolds-averaged Navier-Stokes (RANS), the Large Eddie Simulation (LES) and the Direct Numerical Simulation (DNS) listed from highest to lowest level of simplification.

In research lead by Zhao Zhang, an extensive comparison was conducted between different types of RANS and LES models. For the simulations executed in the study the LES provided much more detailed flow features when compared to RANS and the simulated flow behavior was far closer to *in situ* measurements done in experiments (Zhang et al. 2007).

Reynolds-averaged Navier-Stokes

The principle of the RANS models is to decompose some of the unknowns in the governing equations into average and fluctuating components. For example, using a time average could be appropriate when the flow is stationary, meaning it does not change in time. If the flow on average does not vary in any spatial directions the turbulence is said to be homogeneous. For a homogeneous flow, averaging the spatial variables could be a reasonable simplification. However, most engineering problems involve inhomogeneous turbulence and for those cases a time-averaging RANS model is often chosen. (Wilcox 1993, 11-12)

Large Eddie Simulation

For the LES only the small eddies (smaller than the calculation mesh) are modeled, while bigger eddies are calculated without any simplification. This filtering process is done by reducing the range of time and length scales being solved for with a low-pass filtering of the set of governing equations. (Wendt 2009, 324-325)

Direct Numerical Simulation

DNS is not actually a turbulence model, it is the absence of one. It means that the whole range of scales involved, spatial and temporal, needs to be solved for numerically. The smallest scales involved in the DNS model refers to the grid size of the mesh and the time step, scales which need to be chosen carefully. (CFD Online 2017)

2.3.5 Boundary Conditions

When simulating fluid behavior, it is essential to choose proper boundary and initial conditions. They are what truly connects the simulation to the data and determines the outcome. A boundary condition (BC) is a stated restriction required to be satisfied. It limits the possible solutions to a differential equation.

The physical boundaries play a central role when arranging the computational mesh to enable the implementation of BCs in a numerical problem. The grid is constructed in such a way that a set of nodes surrounds each physical boundary; one set is placed on the inside and another is located right on the outside. An intended consequence is that the outermost surface of the boundary FCVs coincide with the physical boundary as illustrated in the two-dimensional representation of the arrangement in figure 2.14. Fluid behavior is only simulated in the internal nodes (From $I = 2$ and $J = 2$). (Versteeg and Malalasekera 1995, 192-193)

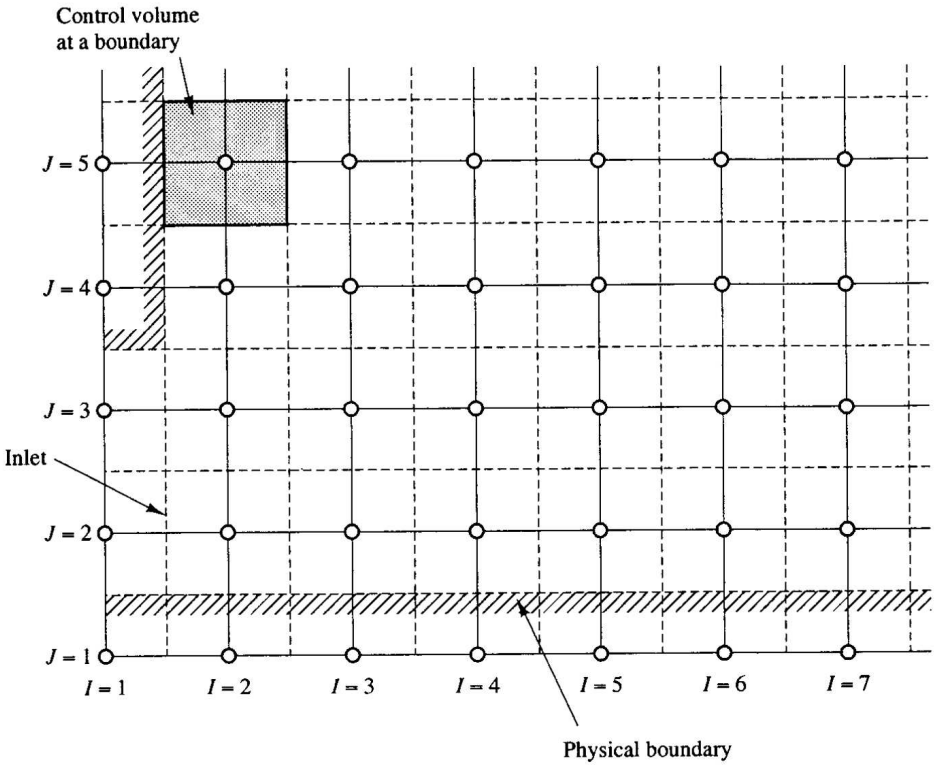

Figure 2.14: Grid arrangement at boundaries (Versteeg and Malalasekera 1995, 193)

Some of the most common BCs in the discretized equation of the FVM are listed below (Versteeg and Malalasekera 1995, 192):

- **Inlet**
  The distribution of the flow variables entering the system to be simulated. Examples are velocity, pressure, density, mass and direction of the movement. In figure 2.14 the inlet is the two grid points $(1, 2)$ and $(1, 3)$.

- **Outlet**
  The outlet BC is similar to the inlet, but defines the distribution of flow variables at the exit. If the outlet is sufficiently far downstream of any geometric obstacles the fluid may reach a fully developed state, meaning that no change occurs in the direction of the flow in the region. If that is the case than a BC could state that the gradients of all variables, except pressure, are zero in the direction of the flow. (Versteeg and Malalasekera 1995, 197).

- **Wall**
  A wall boundary condition defines how the walls affect the fluid in contact with it. There are a lot of factors involved, including whether the fluid behavior is laminar or turbulent, how rough the walls are or if the walls are moving themselves. For a viscous fluid, the BC on the surface of a wall, called the no-slip condition, assumes no relative velocity between the wall and the fluid it is in direct contact with. (Versteeg and Malalasekera 1995, 198-203)

- **Prescribed pressure**
  A condition of constant pressure can be assigned in association to inlet and outlet areas, but also inside the physical boundaries. This type of BC is often used instead of the inlet and outlet conditions when detailed information about the distribution of flow variables at the inlet and outlet is absent. (Versteeg and Malalasekera 1995, 203-204)

2.4 Geographical Information System

2.4.1 General Introduction

A Geographical Information System, commonly referred to as GIS, is any system that stores, analyses and displays spatial and geographical data. In the past two decades, the utilization and application of GIS has increased significantly and is now a great aid to a variety of industries, from agriculture assessment to space technology and environmental monitoring.

2.4.2 Acquiring Data

Most of the data commonly used in GIS is either recorded by high altitude satellites or any kind of low altitude aircraft, usually in the troposphere. The sensors used for the task could either be passive (for example Modis and Landsat) or active (for example RADAR and LIDAR), see figure 2.15.

Passive sensors are designed to measure reflected, refracted or scattered sunlight from the surface of the Earth, as well as the atmosphere itself. The sensors can be designed to also detect electromagnetic waves of longer wave length (lower energy), such as Earth's thermal radiation in the form of infrared.

Contrary to the passive sensors are the active sensors which send out energy to harness the desired information by measuring how much of the signal is reflected. A benefit of providing its own source of energy is that active sensors can also collect data at Earth's night side. The remote sensing technology RADAR (Radio Detection and Ranging) sends out radio waves able to pass through clouds. Similarly, LIDAR (Light Detection and Ranging) uses near-infrared lasers to make high-resolution topography maps of Earth's surface, but is far more sensitive to outdoor conditions and thus applied at low altitude flights.

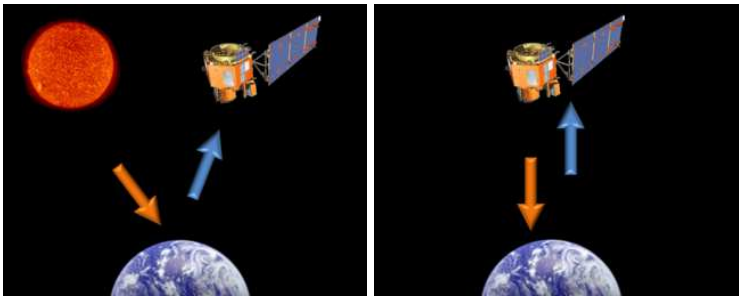

(a) Passive **(b)** Active

Figure 2.15: Passive and active sensors in remote sensing (NASA 2017)

2.4.3 Universal Transverse Mercator

The acquired data needs to be georeferenced into the same geodetic datum and use the same map projection to be successfully utilized by any GIS software. A geodetic datum is a type of coordinate system and a map projection is a way of representing a surface expanded in three-dimension on a flat map.

The true shape of the Earth is not perfectly round, but more like an oblate spheroid. It means that the radius from the center to equator is somewhat greater than from the center to the poles. As the Earth is not flat, the acquired data must be reinterpreted then projected onto a conventional map.

A common solution is to use the Universal Transverse Mercator (UTM) coordinate system. It is a system that divides Earth into 60 zones, each zone is a six-degree band of longitude, as seen in figure 2.16a. Consequently, the division method results in an uneven width of the zones. They will be at their widest at the equator and decreasing in width towards the poles.

For map projections, UTM uses a secant cylinder in a transverse position and the method is illustrated in figure 2.16b. It simplifies the surface of the Earth as the curvature within each zone is flattened.

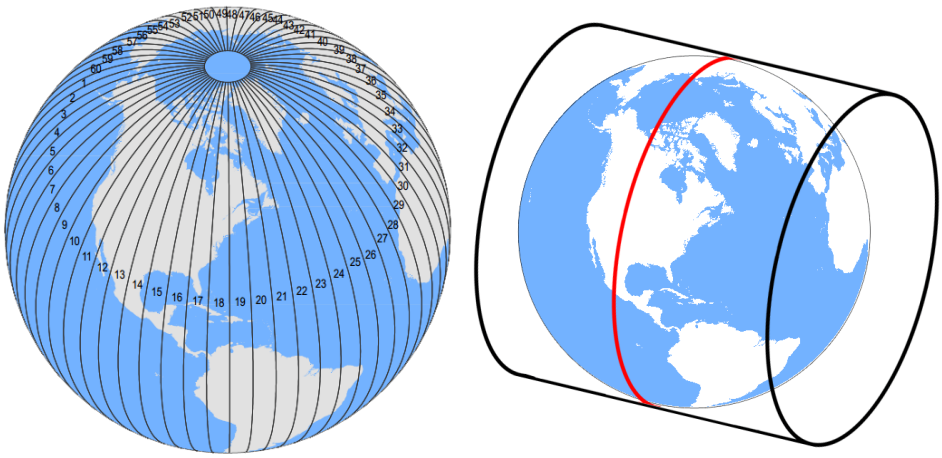

(a) (b)

Figure 2.16: UTM zones and projection method (GISGeography 2017)

2.4.4 Digital Elevation Model

General Introduction

There are two main structures or formats for storing GIS data, vector and raster. A vector file consists of single or multiple points, lines or figures placed in an otherwise transparent layer. Raster on the other hand holds a value for each point in a grid system, just like pixels in a photo. Each value, or pixel, characterizes an attribute of the location it represents.

The values could represent any preferred attribute (of the location), such as reflectance of red, green, blue or even infrared light. Another frequently used attribute is elevation. A raster or vector file containing information about the elevation is called a "Digital Elevation Model" (DEM) and an example is provided in figure 2.17. DEMs are most commonly available in raster format and will therefore be the chosen format in this study.

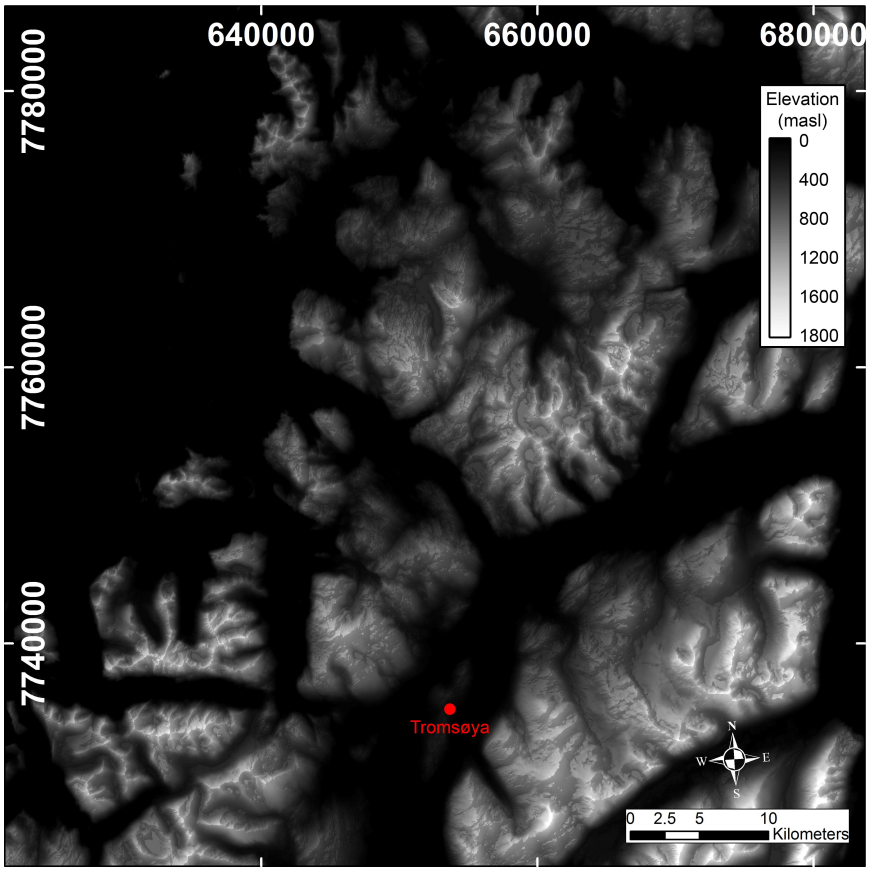

Figure 2.17: DEM produced using photogrammetry, northern region of Troms County
Datum: WGS85 Proj.: UTM-33N

There are a variety of techniques to obtain DEMs. Some of the commonly used ones are photogrammetry, LIDAR, IfSAR and land surveying (Li et al. 2005). As the nature of the techniques is quite different so is the corresponding accuracy and resolution. Some of the methods might calculate the average elevation within each zone the pixel represents, while other methods might simply use the elevation at the center.

DEM is a generic term covering both the terms "Digital Terrain Model" (DTM) and "Digital Surface Model" (DSM). A DTM represents the bare terrain when objects like buildings, trees and other types of vegetation are excluded, while DSMs include those objects. The difference between DTM's and DSM's is illustrated in figure 2.18 to the right.

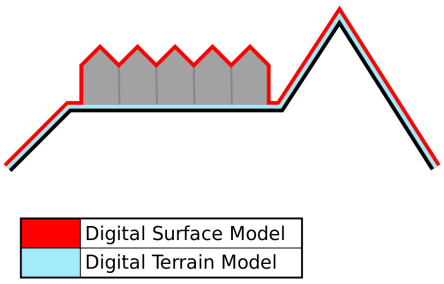

Figure 2.18: Difference between DSM and DTM (Defra 2011)

DEMs are available for the public for most areas of the world with different resolutions. Currently (June 2017), the best countrywide DEM of Norway is a DTM of 10 meter resolution. The next level of high resolution DEMs in Norway are planned to be produced using LIDAR technology. For some places they are already produced, but not jet accessible for the public as special permission is required.

Photogrammerty

Perhaps the most commonly used method when producing DEMs is photogrammetry. Photogrammetry is the science and technology of utilizing photographs to obtain spatial measurements of any kind (Lillesand, Kiefer and Chipman 2015, 146). All the DEMs used in this study, except for one constructed of LIDAR data, have been produced through photogrammetry.

It is important to recognize that single aerial photographs cannot be used as accurate maps, as they do not show the true surface of objects, but only the view from a single point in space. Near objects appear bigger in comparison with distant ones and, as an example, mountains seem to "lean away" from the principal point of a photograph radially. This effect of misrepresenting reality is called "relief displacement" and needs to be accounted for when producing maps and other reliable ground measurements. (Lillesand, Kiefer and Chipman 2015, 147)

Although relief displacement is usually thought of as an image distortion it can be utilized to measure distances. By comparing the relief displacement in a pair of stereo images, enough information about the terrain can be harnessed to produce a DEM using simple trigonometry. A stereo pair refers to two images of the same location taken from two slightly different positions with a certain degree of overlap, as illustrated in figure 2.19.

Governing distance using a stereo pair of images is the very same principal humans, and most animals, use to get a better understanding of our surroundings. Estimating distances of more than just 10 meters or so using this method becomes difficult and inaccurate for humans as the distance between our eyes is typically not more than 7-8 cm. Luckily, satellites and airplanes do not share the same constraint of a rigid and relatively narrow image separation and can be used to measure far more distant objects in a sufficiently accurate manner.

Figure 2.19 below illustrates the basic principle of producing DEMs through photogrammetry. S_1 and S_2 are the positions of the camera, called the projection centers. a' and a'' are pixel positions representing the same point on the ground, point A, as they appear in the corresponding two images. Matching pixels are paired up, like a' and a'', digitally in the overlapping area and elevation values for the DEM are calculated.

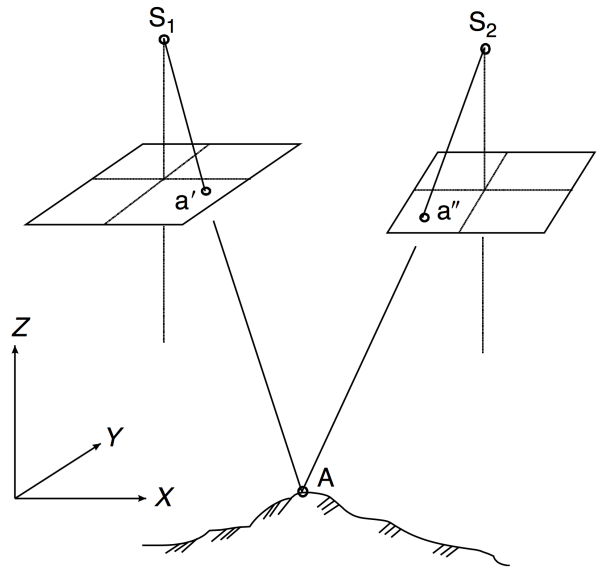

Figure 2.19: Producing DEMs through photogrammetry (Li, Zhu and Gold 2005, 38)

LIDAR

Sometimes the resolution and accuracy of a DEM obtained by photogrammetry is unsatisfactory. In those cases, producing the DEM using data provided by a LIDAR device is a solution. Both LIDAR and RADAR are active systems (see figure 2.15) sending out electromagnetic radiation, but differ as they are transmitting different parts, or channels/bands, of the spectrum. RADAR uses radio waves and LIDAR sends out laser, referring to electromagnetic radiation in the range of 1040 to 1060 nm (Li, Zhu and Gold 2005, 53).

As the speed of light is known to be constant in a medium, the distance covered by that light can be calculated by measuring the time of flight. LIDAR utilizes this relation to calculate the distances to objects. It works by sending out pulses of laser light, the light that is reflected directly back to the sensor of the LIDAR-apparatus is measured and the distance to the object reflecting the light can be calculated.

When an object is illuminated with laser light the light does not have to be reflected directly back to the sensor. Whatever happens to the radiation is governed by the property of the object, such as its density and thickness or the texture of the surface. In addition to reflection, the light could also be refracted, or partially or entirely absorbed. Figure 2.20 illustrates a typical return signal obtained using LIDAR. It shows multiple returns as various surfaces are "hit" and the difference in signal intensity is dependent on the physical properties of the objects.

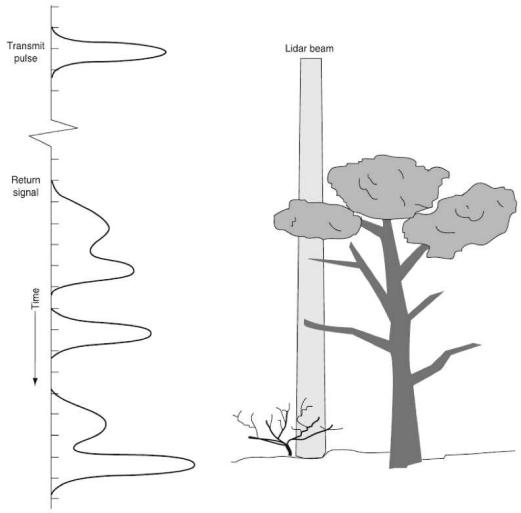

Figure 2.20: LIDAR pulse recording multiple signal returns (Lillesand, Kiefer and Chipman 2015, 474)

To be able to create a DEM using LIDAR the area of interest needs to be scanned in a way than ensures enough information and accuracy. A commonlu used method to gather terrain data is to use the airborne scanning LIDAR system illustrated in figure 2.21. It is typically mounted on a small aircraft equipped with:

- An IMU of sufficient accuracy. IMU stands for Internal Measurement Unit and measures the angular orientation of the sensor relative to a reference point on the ground.
- A high-precision GPS. GPS is an abbreviation of Global Positioning System and calculates the airborne sensor's position in space.
- A rapidly pulsing laser (10^4 – 10^5 pulses/sec) (Lillesand, Kiefer and Chipman 2015, 472).
- A highly accurate clock.
- A robust data storage.

Together with a ground based GPS the data is combined to make a three-dimensional point cloud representing surfaces of scanned objects. (Lillesand, Kiefer and Chipman 2015, 472)

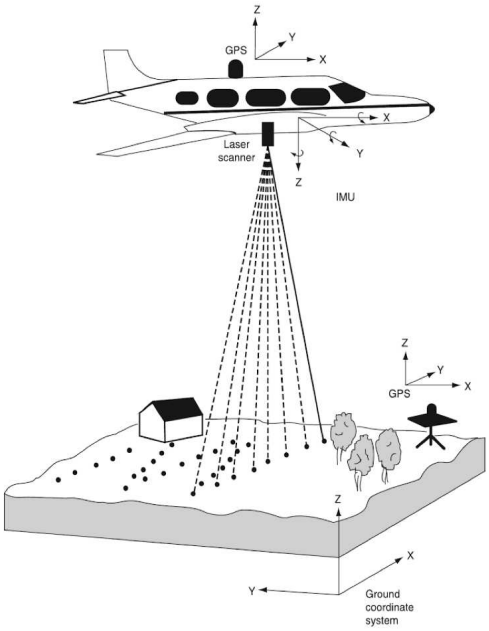

Figure 2.21: Airborne scanning LIDAR system (Lillesand, Kiefer and Chipman 2015, 473)

To simplify the process, the data in the point cloud is filtered enabling the production of any type of DEM, either in vector or raster format. As a point cloud obtained using LIDAR can hold information about multiple layers in the terrain, such as the height of buildings, vegetation and the bare ground, the data can be used to exclude certain features when producing a DEM. Essentially, both a DSM and a DTM can be produced from the very same LIDAR data set.

2.4.5 Triangulated Irregular Network

As a raster DEM is simply a collection of points, it needs to be assigned a surface if it is to be used as a 3D-model for fluid simulations. One approach is to use the points to make a Triangulated Irregular Network (TIN) out of them. The points serve as nodes, or triangle corners, in a continuous network of nonoverlapping triangles. If the DEM is produced by photogrammetry, the points will typically be grid points evenly distributed on the xy-plane with different elevation values. For DEMs generated using LIDAR technology the points will be semi-randomly distributed on the xy-plane.

Triangles have a special property making them perfect building blocks for surface modeling. The property referred to is that any grid of squares or rectangular cells, even any polygon, can be decomposed into a series of triangles as base units. Triangle-based surface modeling is highly geometry tolerant and a feasible method regardless the data pattern type, even if it includes merging vector and raster files. (Lillesand, Kiefer and Chipman 2015, 69-70)

The precision and quality of the TIN depends on the underlying triangle mesh, hence there is no unique way of arranging it. “Delaunay triangulation” is the most used algorithm when generating a triangle mesh for TINs and in its simplest form it generates a surface embedded in a two-dimensional Euclidean plane. Here the triangles are chosen so that the circumcircle of each triangle does not contain any data point in its interior, making the triangles as equiangular as possible, see figure 2.22. (Floriani and Magillo 2009, 3178)

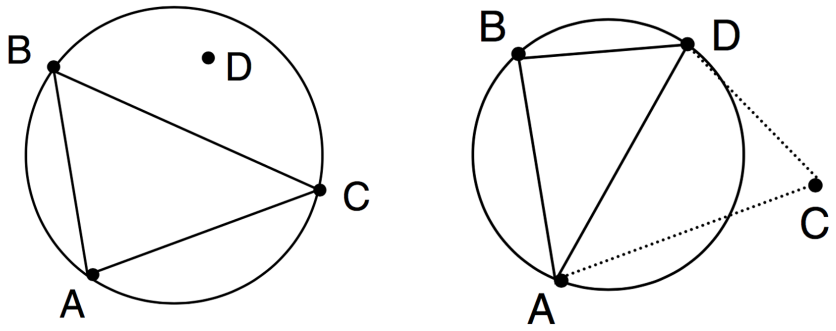

(a) Circumcircle countaining point D **(b)** Point D is used to form a new triangle

Figure 2.22: The empty circumcircle principle for Delaunay triangulation, 2D (Li, Zhu and Gold 2005, 38)

In this study, the TINs represent terrain surfaces and therefore need to be open two-dimensional manifolds embedded in three-dimensional Euclidean space. The only difference in the algorithm of generating the mesh is that the circumcircle in figure 2.22 is replaced with a circumsphere.

Delaunay triangulation is easily implemented in Matlab and two examples of TINs generated using this algorithm are presented below in figure 2.23. The one to the left exemplifies a TIN from a photogrammetry-DEM as the points are evenly distributed on the xy-plane. To the right is an illustration of what a LIDAR-DEM might look like as the points are sub-randomly distributed on the xy-plane.

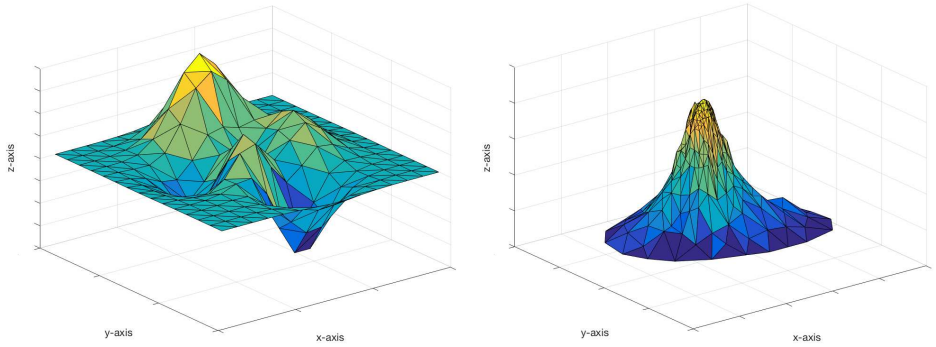

Figure 2.23: TINs generated with 3D Delaunay triangulation

Using a TIN with a Delaunay mesh has been proven to improve the quality of the terrain approximations while at the same time enhancing the numerical stability when generating and using the model (Floriani and Magillo 2009, 3178).

3

Methodology

3.1 Weather Data

3.1.1 General Introduction

The weather data in this study serves two purposes: to provide reliable input values for the simulations conducted and to validate the simulation results. The input values represent the common wind conditions of the given location and are determined by analyzing data from two separate weather stations located at the main island of Tromsø. Their location, in addition to the location of a pair of wind sensors installed for simulation validation, are pinpointed in figure 3.1.

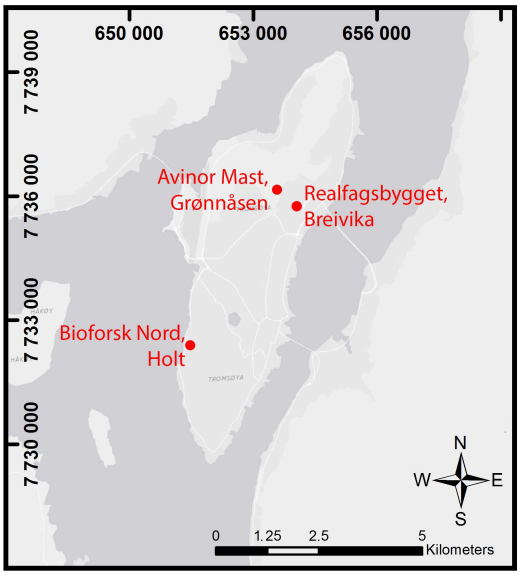

Figure 3.1: Used weather data origin, Tromsø
Datum: WGS85 Proj.: UTM-33N

The weather stations are located at Holt and Realfagsbygget. For both locations, the wind direction and the average wind speed from each measurement are retrieved. In addition, temperature measurements from Holt are gathered as the data is required for the simulation of wind resources in Openwind. To validate the simulations, wind sensors were installed in a mast located at Grønnåsen, as early simulations indicated the area was feasible for installing a wind turbine. Also, the wind data from Grønnåsen is required for investigating its correlation to the data sets gathered from other nearby weather stations which provide a much longer time series

3.1.2 Bioforsk Weather Station, Holt

Bioforsk is a research institute for agricultural and environmental sciences and is located 3.9 km southwest of Realfagsbygget (see figure 3.1). It uses a heated ultrasonic anemometer to measure both wind speed and direction while preventing icing from influencing the measurements. The anemometer is placed two meters above the ground in the middle of a field and is the one on the right-arm of the installation in figure 3.2b. The weather data is publicly available and is averaged over one hour.

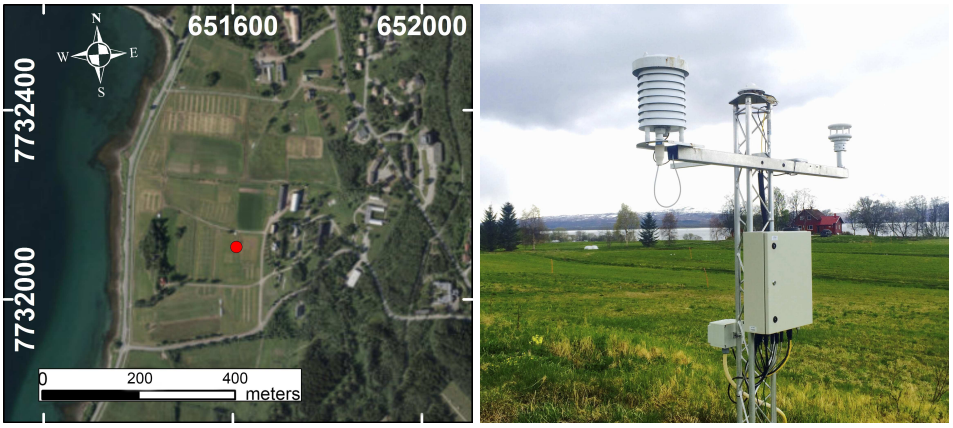

(a) Datum: WGS85 Proj.: UTM-33N **(b)** Photo: T. Hågbo 2016

Figure 3.2: Bioforsk weather station, Holt

3.1.3 Realfagsbygget Weather Station, Breivika

The weather station at Realfagsbygget is located on the roof of the exact same building as one of the suggested locations for a wind turbine. The data from this station is therefore by far the most valuable of the two data sets when deciding input parameters to be used for the simulation of local wind behavior in the area. At Realfagsbygget, the wind direction and the average wind speed are measured each minute and the anemometer and the wind vane are located two meters above the roof.

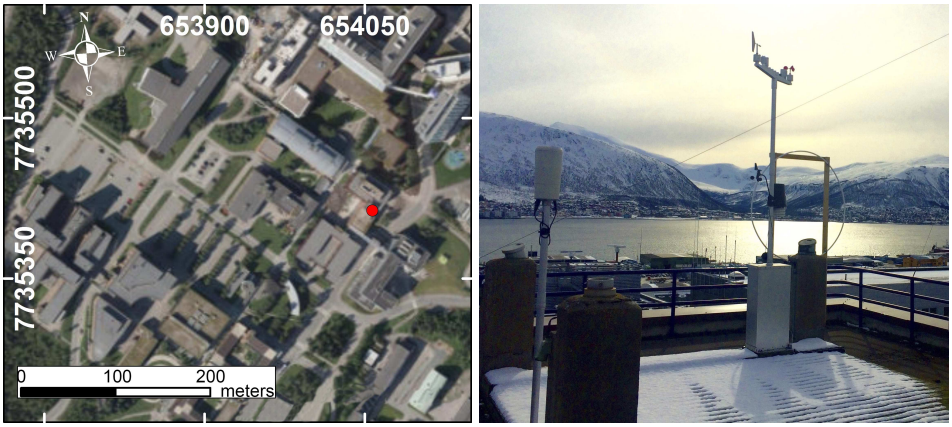

(a) Datum: WGS85 Proj.: UTM-33N **(b)** Photo: T. Hågbo 2016

Figure 3.3: Realfagbygget weather station, Breivika

Teknologibygget (the Technology Building), a neighboring building of Realfagsbygget, was erected in the autumn of 2014. It is plausible that the presence of Teknologibygget affects the flow of wind over Realfagsbygget, at least to some extent. As of spring 2017, the measurements from 2015 and 2016 are the only complete data years on record due to the construction and effect of Teknologibygget on subsequent data.

3.1.4 Avinor Mast, Grønnåsen

Initial research and data suggested that Grønnåsen was a suitable place to install a wind turbine connected to a hybrid system at the university campus of UiT. A telecommunication mast located in Grønnåsen, and owned by Avinor, was outfitted with sensors to measure wind speed and direction at two different heights (at 6 and 21 m AGL). Heated sensors that prevent icing are very costly and as icing did not seem to be a big problem in the mast it was decided that sensors without heating were sufficient.

The wind sensors at Grønnåsen were mounted in the Avinor Mast and fully functioning from the 8^{th} of February 2017. The weather data from Grønnåsen presented in this study is continuously logged data in averages of 60 second intervals from the 9^{th} of February to the 9^{th} of May 2017.

The sensors are the *WindSonic – Ultrasonic Wind Sensor* model produced by Gill Instruments Limited. Instead of measuring the wind using a weather vane and a spinning cup anemometer, the WindSonic utilizes properties of ultrasonic sound waves. It measures wind speed and direction based on the time of flight of sonic pulses between pairs of transducers, which are sensors producing a signal. Sound waves are vibrations propagating in a medium, for example air, and will be affected by the wind. If the wind is blowing northward, the sonic pulse transmitted from the southtransducer will be received faster at the northtransducer rather than the other way around, while pulses from the east-west pair will have the same time of flight regardless of the direction of the lateral movement.

For data organization, the use of a local logging program, known as 'Spacelogger.S10, was determined to be sufficient due to its compatibility with the wind sensors, as well as the local annual temperature range.

For data organization, the use of a local logging device, known as "Spacelogger.S10", was determined to be sufficient due to its compatibility with the wind sensors, as well as the local annual temperature range. It also provides many options for storing the data. Data for this case study was stored by the logger every minute according to average values of wind speed and direction in pairs.

The baud rate of each sensor was found to be 4800 bits per second, but it was set to only store average values for every minute. As a result, the total information stored is 9600 bits, or 1200 bytes, per minute. The memory card can store 2 GB which allows for approximately 621 days of data accumulation, more than is required to demonstrate this study's findings. The calculation is presented below:

$$t_{\text{full card}} = \frac{2\ GB}{1200\ B/min \times 60\ min/hr \times 24\ hrs/day}$$
$$= \frac{2 \cdot 2^{30}\ B}{1.728 \cdot 10^{6}\ B/day} \approx 621\ days$$

Figure 3.4 shows how the wires from the sensors and the DC power supply terminals are connected to each other and to the data logger. As a continuously logging of data is demanded, the remote wires (the white ones) are redundant and therefore not connected to the logger, but taped with electric tape.

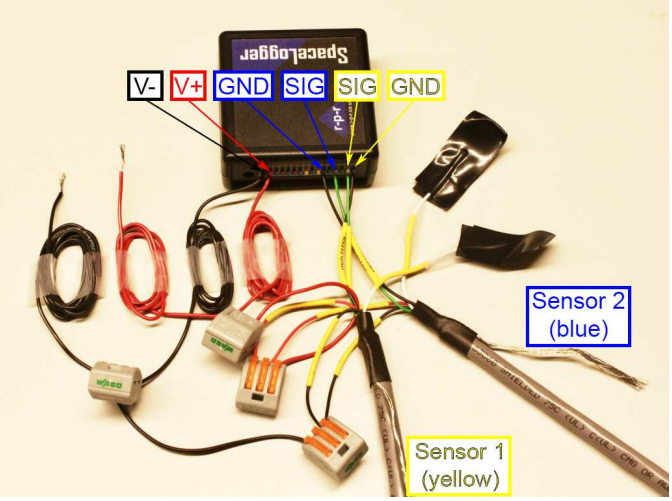

Figure 3.4: Connection to the data logger. Photo: T. Hågbo 2017

Due to accessibility issues related to the ownership of the mast, the logger was attached to the interior of a wall surrounding the mast. The logger was placed inside a waterproof suitcase to shield it from the weather, see figure 3.5. Three holes were placed in the bottom of the case to allow for the DC power supply to run from the nearby Avinor equipment shack in addition to the two signal cables from the sensors. To prevent water from entering the suitcase, the holes were sealed using gasket nipples, silicone and electric tape. The suitcase is secured with a combination code lock. Also, the enclosure surrounding the mast is locked and access is restricted by a pair of keys shared with Avinor. A quick guide to obtaining the data is provided in appendix A.

Figure 3.5: Data logger suitcase. Photo: T. Hågbo 2017

Figure 3.7 shows the placement of the two sensors in the mast and its location at Grønnåsen is presented in figure 3.6. As most of the wind in the region comes from the South or South-southwest, see section 4.1.3, the metal poles in which the sensors are attached to were pointed directly towards the East. In doing so, the air could pass through the sensors as unaffected by the mast as reasonably possible.

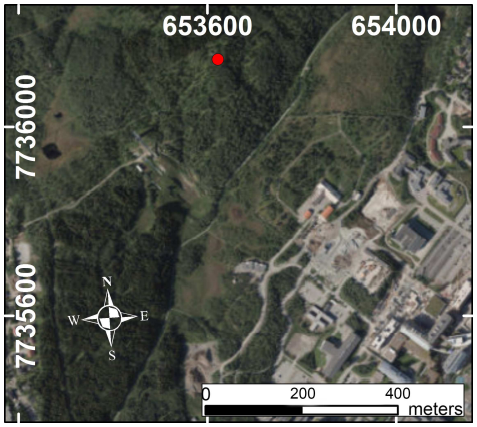

Figure 3.6: Avinor mast, Grønnåsen
Datum: WGS85
Proj.: UTM-33N

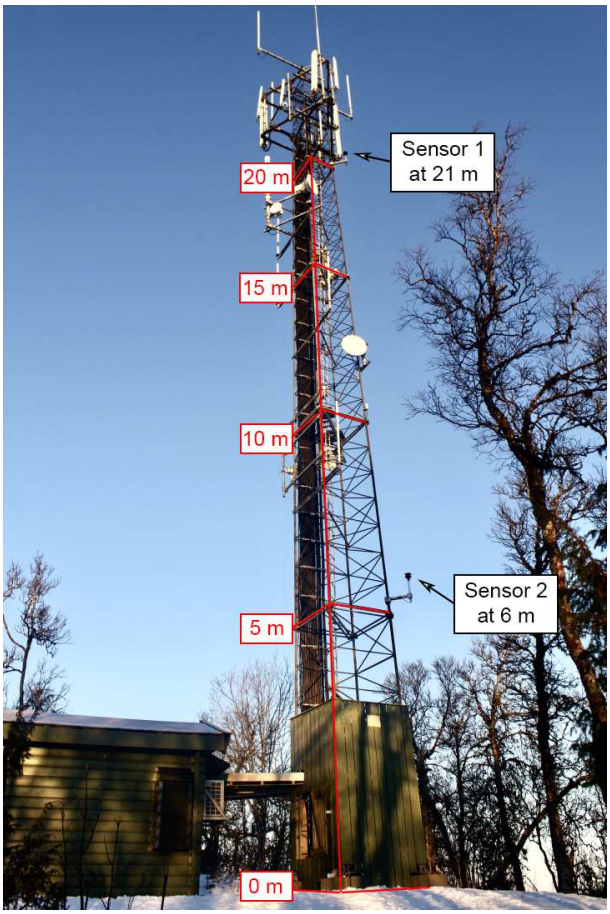

Figure 3.7: Wind sensors placement in the mast. Photo: T. Hågbo 2017

The tree on the right side of figure 3.7 is the closest one to the sensors and also the tallest relative to the mast at about 12 m AGL. The other trees in the area are about the same height relative to the ground, but do not reach the same elevation as the tallest reaching tree is placed on the highest elevated point at Grønnåsen.

One of the sensors, sensor 1, is positioned 21 m AGL, much higher than the nearby trees. Except for a small pole-shaped telecommunication device, all of the other equipment in the mast mounted is at least 2 m above or below sensor 1. The pole-shaped apparatus is vertically orientated, has a length of about 1 m, a diameter of approximately 5 cm and is positioned roughly 1.5 m west-southwest (250°) of the sensor. Sensor 2 is placed 6 m AGL, meaning that the measurements are likely affected by nearby vegetation resulting in turbulent air flows.

3.1.5 Explanations of the Plots

To analyze the weather data, two types of plots are chosen: histograms and wind roses. Explanations of the graphical representation methods are provided below.

Histogram

Histogram plots are considered suitable when studying the distribution of wind speed and how it changes with the seasons. Histograms sort wind speed data into columns representing the frequency of a discreet interval and do not account for wind direction nor time measurement. To investigate seasonal fluctuations, histograms containing multiple sets of data were created for each season.

For the seasonal histograms, Weibull distributions are also added with a secondary y-axis to the right. The Weibull distribution is a type of probability distribution and is known to suit datasets for the velocity of the wind well. The distributions provide an approximation of what the histograms eventually could look like if the data sets were much bigger and the data was categorized in infinitesimal intervals. The Weibull distributions are continuous functions and can be used to see trends in small data sets more clearly.

Wind Rose

To get an understanding of the correlation between the direction of the wind and the wind speed a type of plot called “wind rose” was chosen. Wind roses are designed for analyzing wind data as they simultaneously sort data into discreet intervals that illustrate the frequency of the wind directions. Much like histograms, they only differ in that they measure the direction of the wind rather than the speed.

Generally speaking, the wind can come from any direction, but it is most commonly measured only in coordinates on a plane orientated normal to the “flat ground”, or the center of the Earth. The data from Realfagsbygget and Holt is no exception. Therefore, the directions of the wind are best represented by a circle divided into 360° degrees. 0° represents North, 90° East, 180° South and 270° West. The wind rose divides the circle into 36 sections of 10°.

The color bands of the wind roses show the wind speed ranges. While, the direction of the longest spokes, the radial distance from center of circle, shows the wind directions with the greatest frequencies which are measured in percentages.

3.2 3D-models

3.2.1 General Introduction

There are a variety of 3D-models used in this case study. Some of them are proprietary (self-made) and some have been produced by companies sharing their work upon request. The process of making working 3D-models intended for CFD can be very extensive and involves coordinating multiple sources of data (public and non-public), file types, tools and programs. Dealing with those quantities of data proved to be computationally intensive.

3.2.2 Tromsøya and Surrounding Area

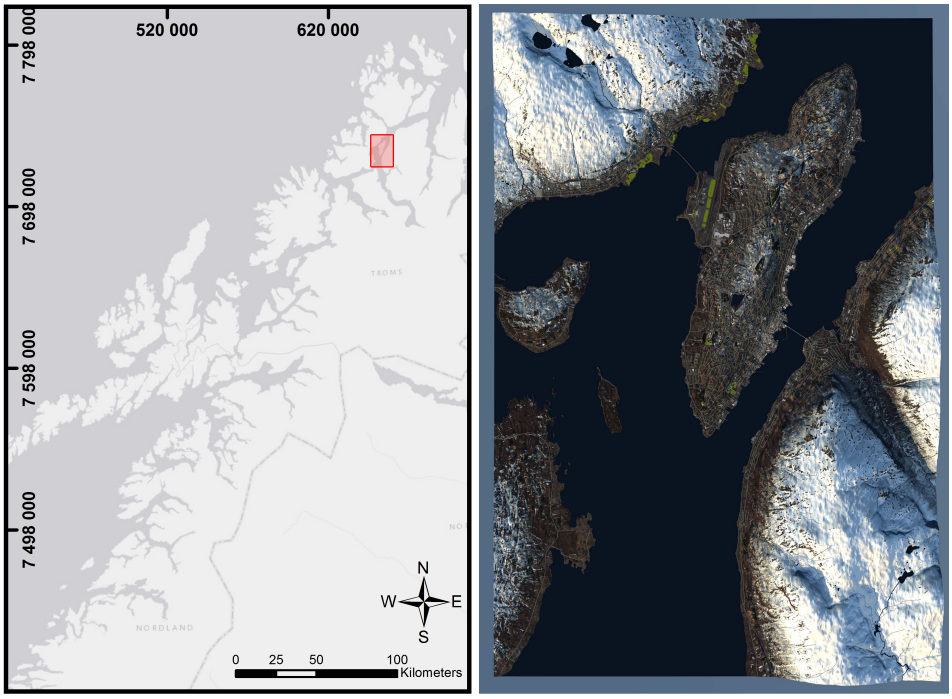

(a) Datum: WGS85 Proj.: UTM-33N **(b)**

Figure 3.8: Tromsøya 3D-model and its origin

Developing the Model

This proprietary model is developed using Autodesk InfraWorks 360 (Infraworks) and QGIS. InfraWorks is a software that simplifies the process of combining multiple types of data into a unified and complete 3D-model of any location. QGIS, an open-source GIS program, is used to put together and prepare multiple DEMs holding the topographic information.

The Tromsøya 3D-model consists of four different layers of information, topography, buildings, imagery and roads. The two first layers, topography, and buildings are responsible for the actual shape of the model. The final two layers, imagery, and roads are added for better visualization and distinction of the locations. Unfortunately, these visualization layers are not included when exporting the model to CFD-software as the simulation tools are incompatible with those layers. The four information layers are all georeferenced using the UTM-33N system enabling seamless merging.

The far most important information layer is the terrain layer. Here a 10 m DTM, is used. It means that one elevation value is assigned an area covering 10 x 10 m in the terrain. The DEM was generated using photogrammetry by comparing stereo pairs of aerial images taken by ASTER onboard the satellite Terra. ASTER stands for "Advanced Space-borne Thermal Emission and Reflection Radiometer" and is owned and operated by METI and NASA. The process of using photogrammetry to obtain DEMs is explained more thoroughly in section 2.4.4. (ASTER 2017)

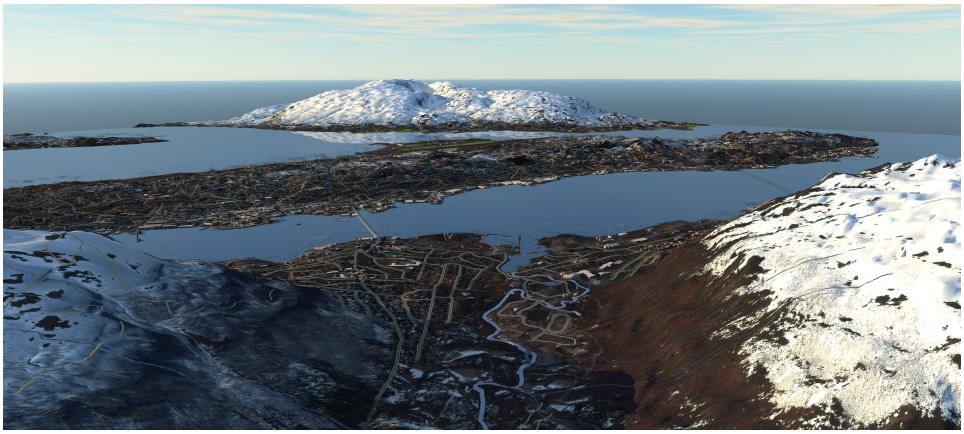

(a) From Tromsdalen

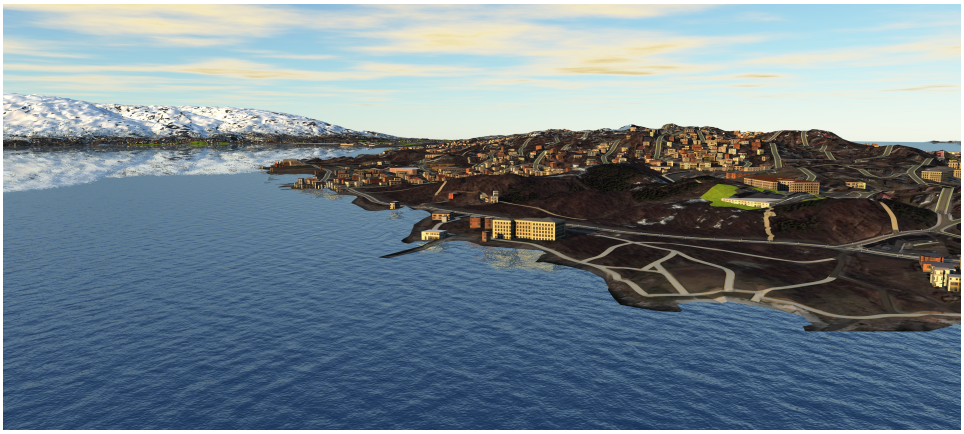

(b) Close-up of the southwestern part of Tromsøya with Kvaløya in the background

Figure 3.9: Tromsøya 3D-model from different angles

As a DTM is just a grid of elevation values and the building layer just contains vector files, they need to be assigned a surface. To do so, while at the same time merging the two layers, the information is combined and used to make a continuous mesh of triangles, also known as a TIN. Each grid point in the DTM and each edge point of the vectors are set to be triangle corners. More about the process of producing TINs is found in section2.4.4. The described arrangement is highlighted in figure 3.10.

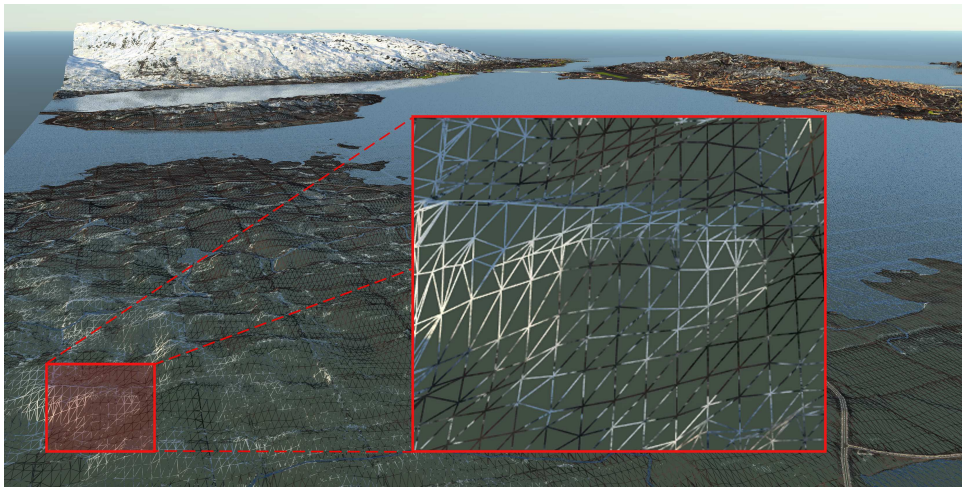

Figure 3.10: Triangulated irregular network

The model is rectangular covering an area of 199.63 km^2 with sides oriented facing north, south, east and west. UTM-34N is the coordinate system giving the boundary coordinates:

$$x_{min} : 18.768407 \quad x_{max} : 19.070531$$
$$y_{min} : 69.571046 \quad y_{max} : 69.725313$$

Here the x-values correspond to longitudes (in degrees east) while the y-values represent latitude (in degrees north).

To save time exporting the model, the number of generator threads was set to four as the computer had a quad-core processor with the ability to use four separate threads. Even though it slowed down the processing, antialiasing was turned on to ensure the reliability of the model. It took approximately one hour to generate a 1.08 GB object file (.obj).

Intended Use

The Tromsøya 3D-model is intended to provide a better understanding of the general wind flow over the area. It does so by singling out areas of interest which can later be used to assess the feasibility of wind power production facilities. A 10 m DTM might not be a sufficient location for a wind turbine in an urban environment such as Tromsøya.

3.2.3 Campus

Acquiring the Models

In 2014, a new university building next to Realfagsbygget was completed. The building is called Teknologibygget and Statsbygg oversaw the construction project. For the project, Statsbygg hired Norconsult section Arkitektstudio to make a model of the building. With approval from Statsbygg, Norconsult shared the 3D-model for use in this study and is presented below in figure 3.11. The 3ds-file has a file size of merely 14.2 MB and unfortunately Norconsult could not provide any information of how the model was produced, but it is quite clear that it is a TIN and that the terrain origins from a DTM.

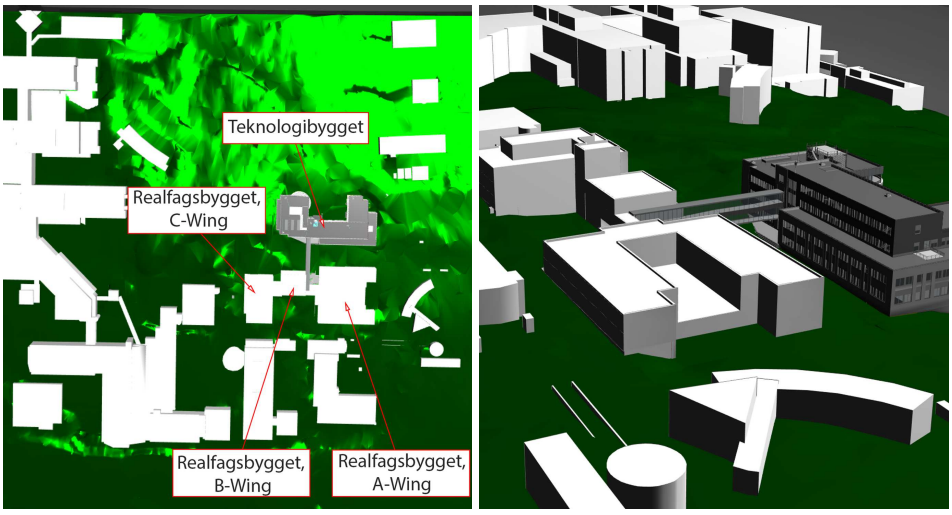

Figure 3.11: Campus 3D-model 1

Statsbygg requested Ramboll Norge AS to make a visualization video of Teknologibygget and its surrounding area. Ramboll went one step further by increasing the area captured in the model and shared it with approval from Statsbygg. In some cases, the model detail appears degraded, particularly in the Realfagsbygget A-wing. In Campus 3D-model 1, the A-wing is shaped like a horse shoe, which is accurate to the real version, but in Campus 3D-model 2 it is simplified to a box shape. See the comparison on the right side of figure 3.11 and figure 3.12.

As the shape of the A-wing is vital for understanding the wind patterns above Realfagsbygget, this study makes use of Campus 3D model 1 to determine the optimal placement of the MWT. Campus 3D model 2 is also utilized to determine any other possible locations for an MWT at the university campus and to investigate the wind behavior in the area of the inlet boundary of Campus 3D-model 1. I have made minor alterations to the model to account

for a recently erected building, the Pasienthotellet, as it does not appear in the original model. Construction drawings of Pasienthotellet were provided by Universitetssykehuset Nord-Norge and the model was updated using Autodesk 3ds Max. The slightly modified model is presented in figure 3.12.

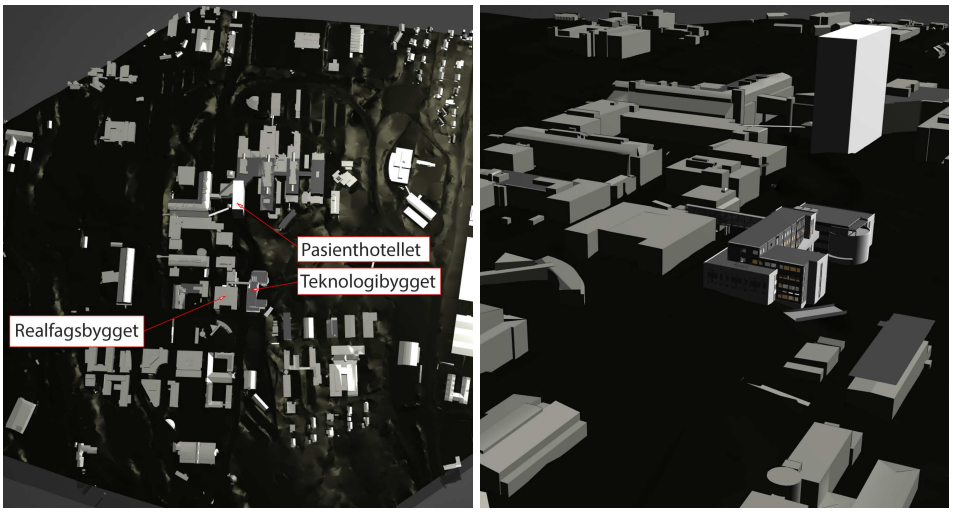

Figure 3.12: Campus 3D-model 2

Intended Use

The two 3D-models of the campus are intended to be used to investigate the behavior of the wind at the campus. The investigation includes revealing probable fluid patterns and to categorize turbulent and laminar regions within the flow for different wind speeds and directions. However, the models are quite small regarding spatial extension and accurate boundary conditions may be difficult to obtain as there are no available annual measurements for the actual physical boundaries of the model.

3.2.4 Grønnåsen and Surrounding Area

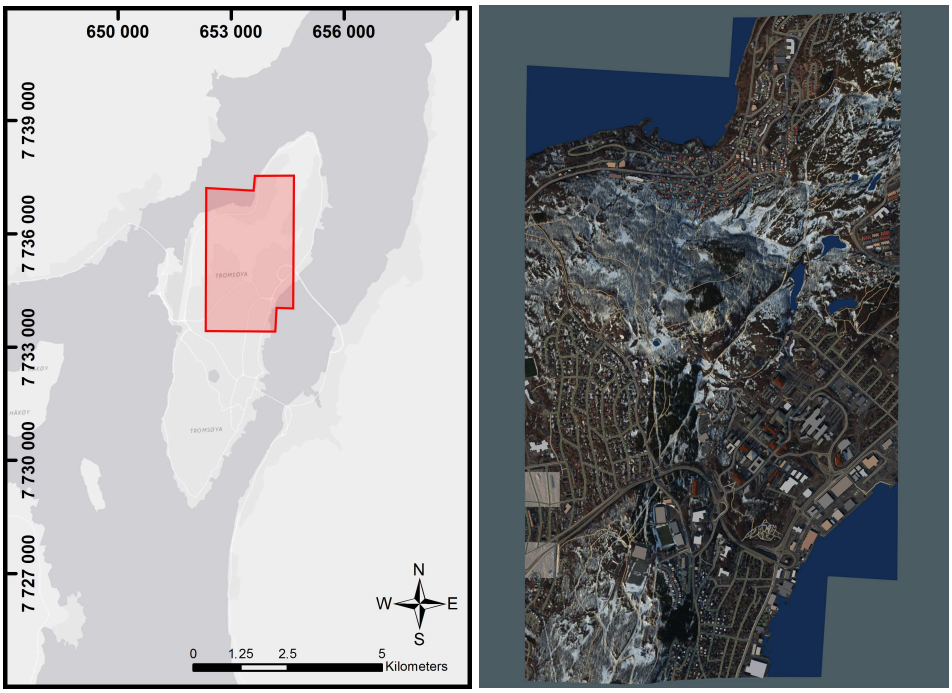

(a) Datum: WGS85
Proj.: UTM-33N

(b)

Figure 3.13: Grønnåsen 3D-model and its origin

Developing the Model

The DEMs, produced through photogrammetry by comparing a stereo set of satellite images, typically have a resolution of 10 m at its finest. A higher resolution would be inaccurate as the distance from the satellite to the ground is far greater than between the ground points, especially if they are less than 10 m apart.

A technology for providing the next level of DEM accuracy is LIDAR, and as data has already been gathered of Tromsø its application to the 3D model will increase detail. LIDAR data was initially stored as a point cloud for further processing and a section of the sampled data set of Tromsø is presented in figure 3.14. It shows a part of the university campus with the easily recognizable labyrinth in the bottom right corner. Each colored point represents the location of an object which had reflected a beam of laser light directly back to the sensor on the airborne LIDAR system.

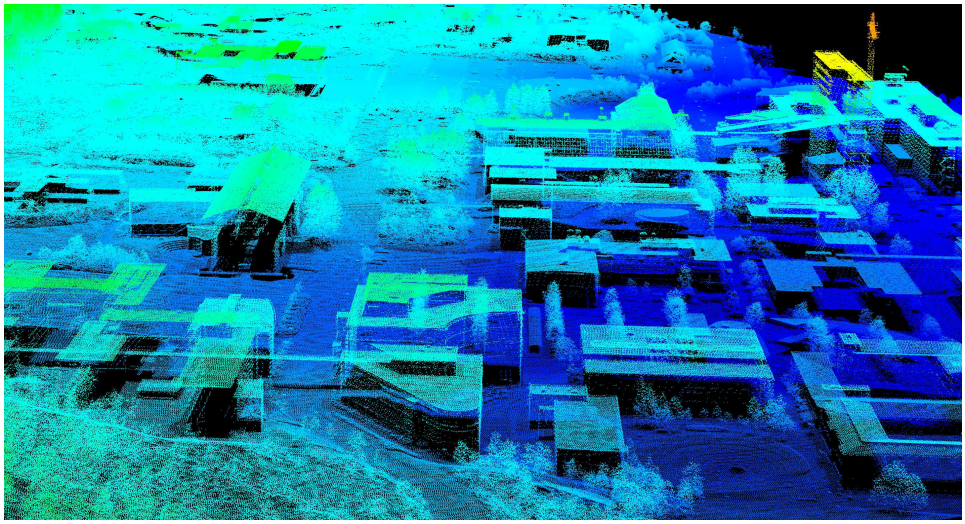

Figure 3.14: LIDAR pointcloud

To process the data, it was decided to use Quick Terrain Modeler by Applied Imagery. Unfortunately, after producing a couple of different types of high-detailed DEMs it was concluded that most of them were simply too complex for Infraworks to generate a 3D-model. Every time the 3D-model to be exported exceeded a limit of about 2.2 GB Infraworks crashed, the very same happened using another computer as well so, it is believed to be a program issue unrelated to hardware.

Fortunately, the LIDAR data set had already been classified. It means that each point was assigned a class, such as “low-vegetation”, “buildings” or “powerlines”, and it enabled the exclusion of classes to produce less complex DEMs. Figure 3.15 shows the difference between a DEM in which only the “bare ground” layer is included and the far more detailed square where the highest point regardless of class type is used in the triangulation process.

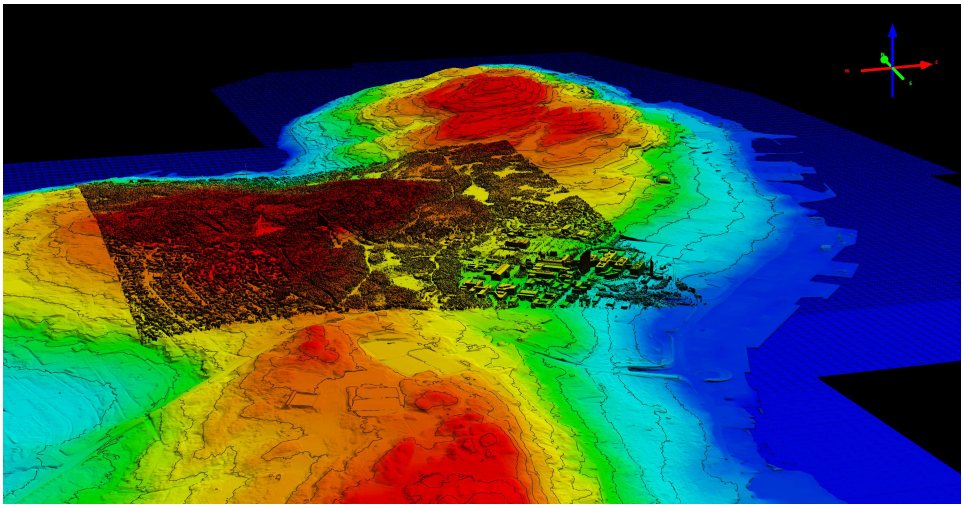

Figure 3.15: LIDAR classes example

The DEM used in the Grønnåsen 3D-model is a raster DTM with one elevation value assigned for every meter squared and is presented in figure 3.16. Just like the Tromsøya 3D-model, the roads, buildings and imagery layers were added and georeferenced using UTM-33N and finally an obj-file of 2.04 GB was produced.

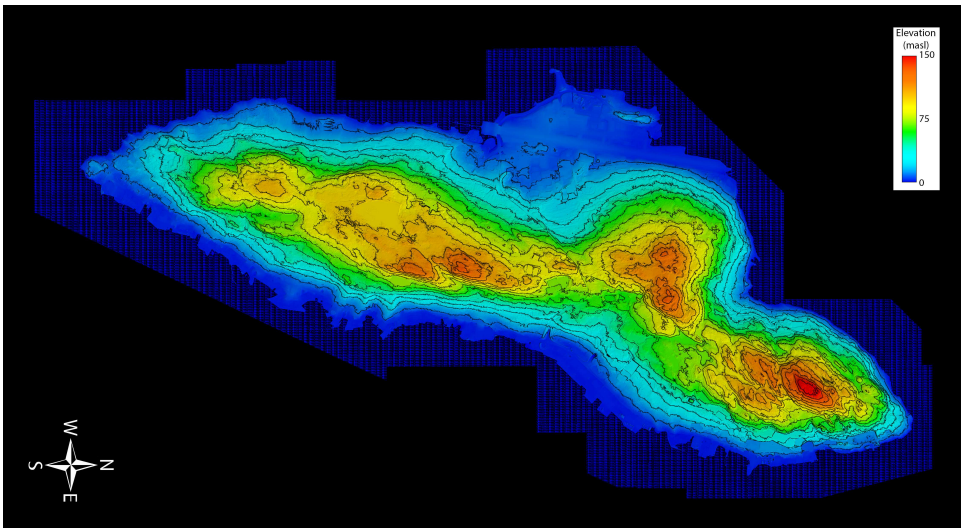

Figure 3.16: 1 m DTM of Tromsøya produced by LIDAR, contour lines every 10 m elevation

Intended Use

Even though highly detailed features, such as vegetation and the tower of the local ski jumping arena, were left out the simulation of the wind through the Grønnåsen 3D-model provided valuable information about the general flow in the area. The model is intended to be used to pinpoint regions that appear to be feasible for wind power production in the Grønnåsen area.

3.3 Autodesk Flow Design

3.3.1 General Introduction

Autodesk Flow Design (AFD) is a CFD-program developed to be "extremely geometry tolerant" (Autodesk 2014, 2) and give reasonably accurate results without demanding a profound knowledge and experience of CFD. "Extremely geometry tolerant" includes not being sensitive to small imperfections in the model and is one of the reasons AFD is chosen when using models obtained through the application of GIS. AFD uses the Finite Volume Method to discretize the fluid equations making them conservative. The turbulence model used is the Large Eddy Simulation. (Autodesk 2014, 2)

3.3.2 Visualization Methods

2D-simulations

2D-simulations are used to quickly assess the wind behavior through a specific cross-section. They are certainly not as accurate as 3D-simulations, but may be valuable as they require less computational power to solve for. They may also more clearly display possible locations of vortices and other types of turbulent flow. The figure to the right, figure 3.17, illustrates exactly that.

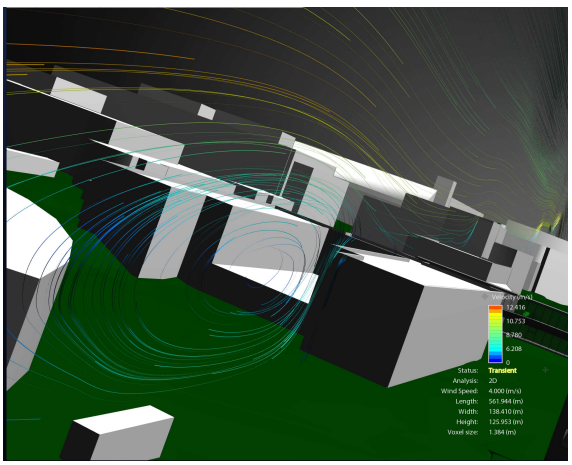

Figure 3.17: Flow lines and vortices, 2D-sim., Campus 3D-model 1

Perhaps the biggest disadvantage regarding 2D-simulations is that the fluid flow is restricted to moving only in a plane and does not account for the surroundings. This simplification is especially problematic in complex surroundings such as urban environments as the surrounding environment of the 2D-plane affects the flow of the air.

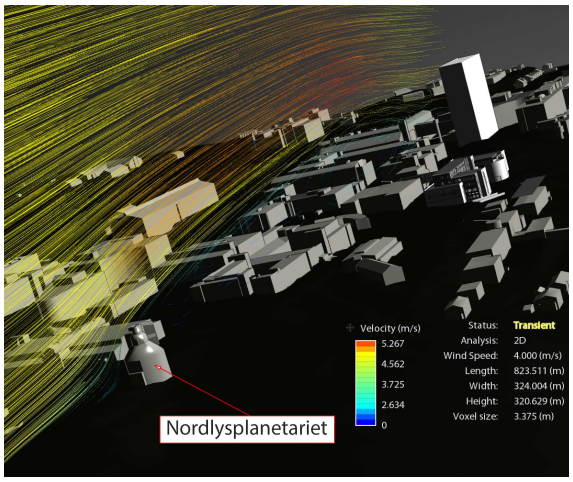

The figure to the left, figure 3.18, is a good example of the described problem. It shows that Norlysplanetariet affects the flow of air downstream significantly more than it would in a three-dimensional space. Most of the air would simply just pass by on the sides of the building and would therefore not create the huge area of turbulence downstream from it.

Figure 3.18: Disadvantage, 2D-sim., Campus 3D-model 2

3D-simulations

General Introduction

Results computed in 3D are more accurate as the flow of air is simulated through and above the entire object, or the region of interest, all at the same time. The flowing air that encounters an object can, when simulating in 3D, pass on any side. In 2D, the flow is restricted to moving only in the simulated plane. AFD has a few alternatives for the visualization of the flow of air in 3D. This study mainly uses “flow lines”, “velocity planes” and especially “isosurface”. It is disadvantageous to use 2D-simulations to simulate airflow in urban environments, so this study will primarily use 3D-simulations.

Flow Lines

Flow lines is perhaps the best tool in AFD to evaluate the nature of the flow, including where the flow is smooth (laminar), where it separates and connects, and especially possible areas of turbulent nature. Unfortunately, flow lines is not very suitable for illustrating the behavior in still pictures. As seen in figure 3.19, the visualization method is erratic and it is difficult to make any conclusions. However, by adjusting the viewpoint, while the flow lines keep moving, the visualization method can provide a better understanding of the flow.

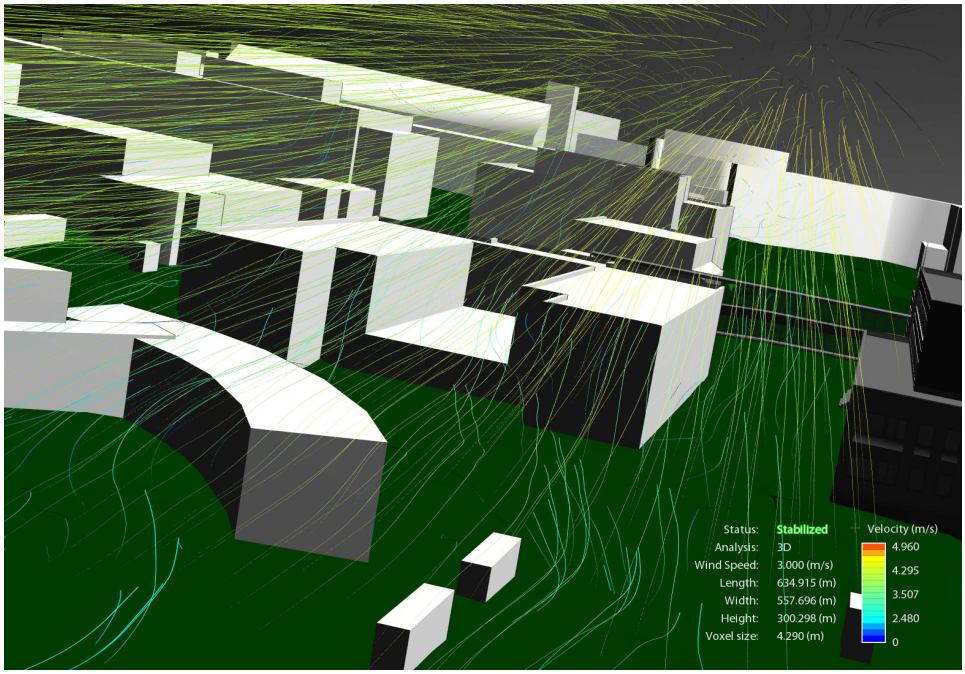

Figure 3.19: Flow lines, 3D-sim., Campus 3D-model 1

Velocity Planes

Velocity planes is a visualization tool to develop a better understanding of how the velocity of the air varies in space. It shows velocity contours of the air located in a plane which can be orientated horizontally or vertically. The figure below, figure 3.20, is an example of both orientations.

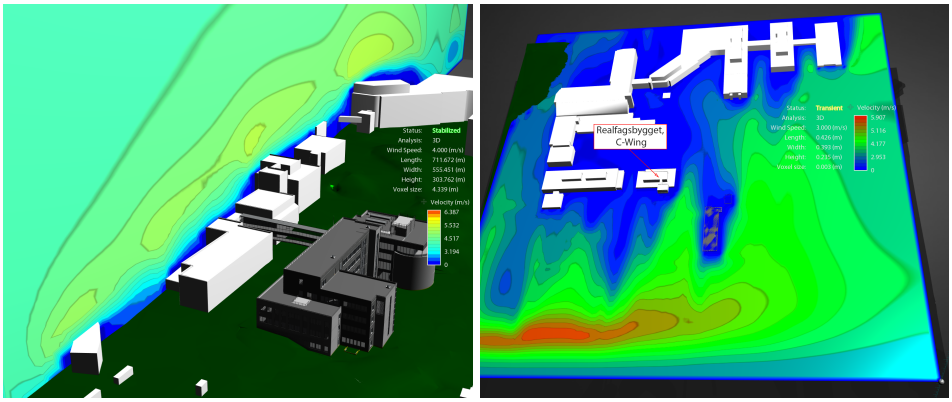

(a) Vertically oriented **(b)** Horizontally oriented

Figure 3.20: Velocity planes, 3D-sim., Campus 3D-model 1

Isosurface
Isosurface works as though you are looking at continuous slices of velocity planes simultaneously with the option to select the velocity to view. An isosurface shows every location in a 3D-simulation that has the same wind speed values and is quite useful when locating regions of the highest wind speeds. For example, the yellow objects in the figure on the right side, figure 3.21, are the contours or rims of the locations of an air velocity magnitude of 7.80 m/s.

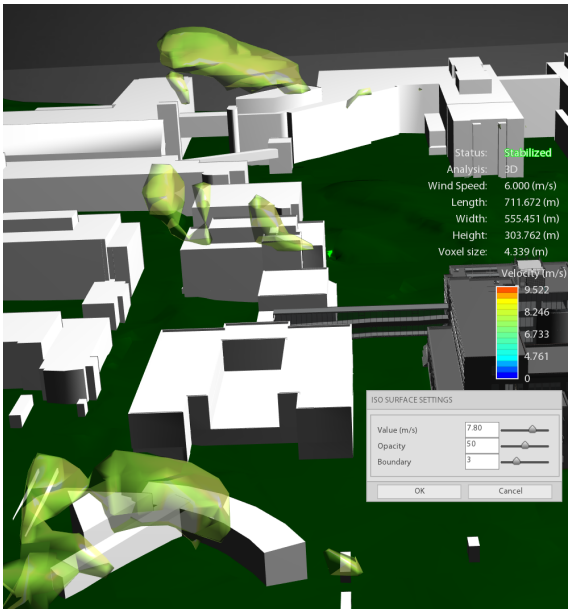

Figure 3.21: Isosurfaces, 3D-sim., Campus 3D-model 1

When locating regions of high wind speed, the speed inside the object is even higher due to continuity. It means that the change in wind speed is smooth and cannot "jump" from for instance 5 m/s to 8 m/s without at one point being 7 m/s.

As a MWT should be placed in an area of high wind speed for maximization of electric power production, the isosurface tool is useful for identifying optimal locations. However, it is important to remember that isosurface does not differentiate between the cause of the high speed, including turbulence. Turbulence is very bad for any wind turbine and needs to be avoided as it decreases the production of electric power drastically and at the same time increases stress. Therefore, the results from isosurface need to be viewed together with another visualization method illustrating turbulence better, such as flow lines.

Interpretation of Simulation Window and Scale
The "Status" could either be "Transient" or "Stable". "Transient" means that the simulated flow has not gotten the time to stabilize and will keep changing its nature by some degree until it reaches its final state as "Stable". "Stable" does not however indicate that the flow cannot vary in time, but rather means that if it does the pattern will be repeating.

The idea of CFD is to divide the three-dimensional space of the flow into a discrete amount of grid points to be calculated. As AFD uses the FVM for discretization these grid points represent small boxes of constant volumes, or voxels, and "Voxel size" is simply the distance from the grid points. AFD restricts the fluid flow simulations to a box-shaped volume of dimensions defined by "Length", "Width and "Height".

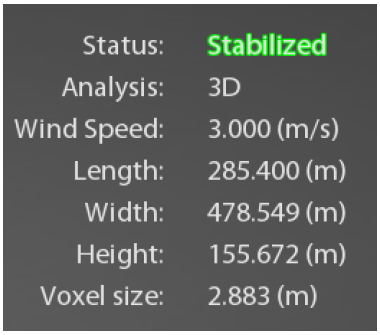

Figure 3.22: Simulation window

The velocity scale in figure 3.23 may seem odd at first. The scale is divided into 16 velocity intervals represented by one color band for every interval. Looking at the values representing the boundary values of every fourth interval, it is clear that the scale is not linear. After well-engineered guesswork, the conclusion was that the interval boundaries used in the scales obey the following formula:

$$b_i = v_{max}\sqrt{\frac{i}{n}} \qquad \forall\, i \in (0, 1, 2, \cdots, n), \qquad n \in \mathbb{N}_1 \tag{3.1}$$

Where b_i is the boundary values of the intervals, v_{max} is the maximum velocity in the simulation and n is a positive integer representing the number of intervals the scale is divided into, for AFD n is 16.

To clarify how the scale works, an example calculation is carried out for the scale to the right, figure 3.23. The maximum velocity in the simulation, v_{max}, needs to be read off the top boundary, hence 9.400 m/s. For example, to find the 4^{th} boundary the value is $i = 4$ substituted into equation (3.1) and $n = 16$:

$$b_4 = 9.400m/s \cdot \sqrt{\frac{4}{16}} = 4.700m/s$$

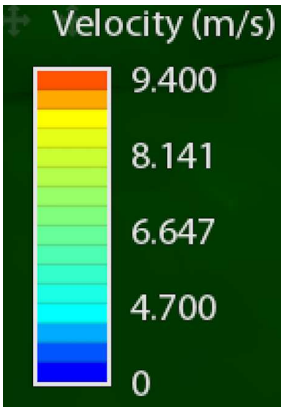

Figure 3.23: Example scale

Resolution Dependency
A high-resolution simulation is understandably often more accurate compared to a simulation of lower resolution. It can solve flow behavior on a smaller scale, like turbulence, which can affect the flow on a bigger scale than itself. However, higher resolution demands more computational power and will therefore require more time to reach a stable state. A general rule is that the resolution is "good enough" when the result of the simulation does not seem to change any more than the desired accuracy.

3.3.3 Boundary Conditions

AFD is a bit different to other CFD software as the wind is simulated through a "virtual wind tunnel"(VWT), see figure 3.24. A clear weakness of the simulation tool is that it does not allow for a gradient inlet wind profile. VWT gives the origin and defines the boundary conditions listed below:

- **Inlet**
  AFD uses the discretization method FVM, which divides the volume of the VWT, highlighted in blue in figure3.24, into a mesh of discreet points assigned to constant volumes. The nodes on the forward facing side of the cube at the left side of figure 3.24 are assigned a scalar value representing the inlet conditions. The value needs to be the same all over the inlet surface as AFD does not allow for any wind profile as input. Here the flow is completely laminar.

- **Outlet**
  AFD uses the conservative set of equations on discretized form. It means that the total mass, energy and momentum is conserved over time. Regarding the outlet conditions, it follows that just as much mass, momentum and energy is going out of the system as in when a stable state is reached.

- **Physical boundaries**
  The fluid flow is restricted to the walls of the "tunnel" and cannot get out through any of the sides perpendicular to the inlet surface. When deciding the size of the VWT this restriction needs to be considered to ensure reliable simulations. The VWT should be big enough so that the flow near the tunnel walls is laminar. It ensures that edge-effects do not interfere with the rest of the flow simulated.

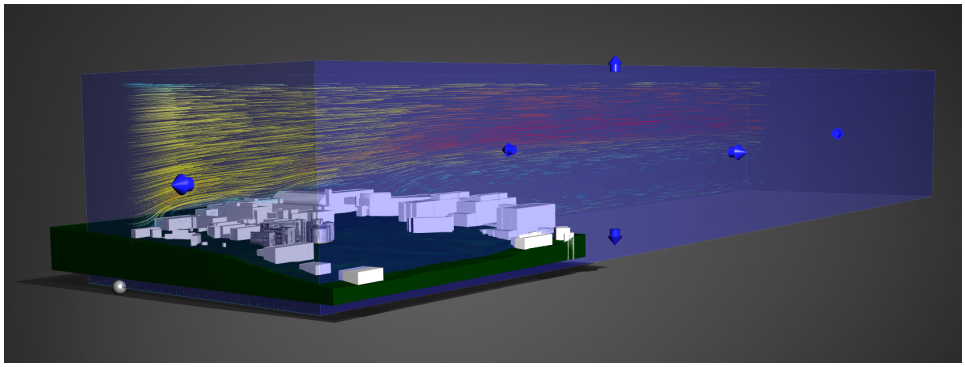

Figure 3.24: Virtual wind tunnel

3.4 AWS Truepower - Openwind

3.4.1 Background

Openwind is a software developed by AWS Truepower to aid in the process of designing, optimizing and analyzing wind farms. It is not a true CFD-program, but a GIS-based program estimating wind flow patterns at given locations based on inputs like wind roses, DEMs and roughness layers. The "Mass-conservation Wind Flow Model" enables the generation of wind data estimations anywhere and performs well in complex terrain(AWS Truepower 2017) and is the only Openwind model applied in this study. AWS Truepower does not provide the functioning of the model, but it has proved to be effective in numerous wind farms and compared to other, more advanced, simulation tools (AWS Truepower 2010, 21-22). (AWS Truepower 2014).

3.4.2 Setup and Limitations

The DEM used in the simulation is a 30 m DTM from Kartverket prepared for Openwind in QGIS. To provide annual weather data to be used in the simulations, data from Bioforsk Nord at Holt was gathered. In addition to wind speed and direction were also temperature data collected as they are required in Openwind. An additional requirement is that the weather data must be in a tabular file format (tab.) and therefore the data was prepared in Windographer - another program developed by AWS Truepower. The DTM (hillshaded) and the weather data used in the simulations, illustrated by a wind rose, is presented in figure 3.25.

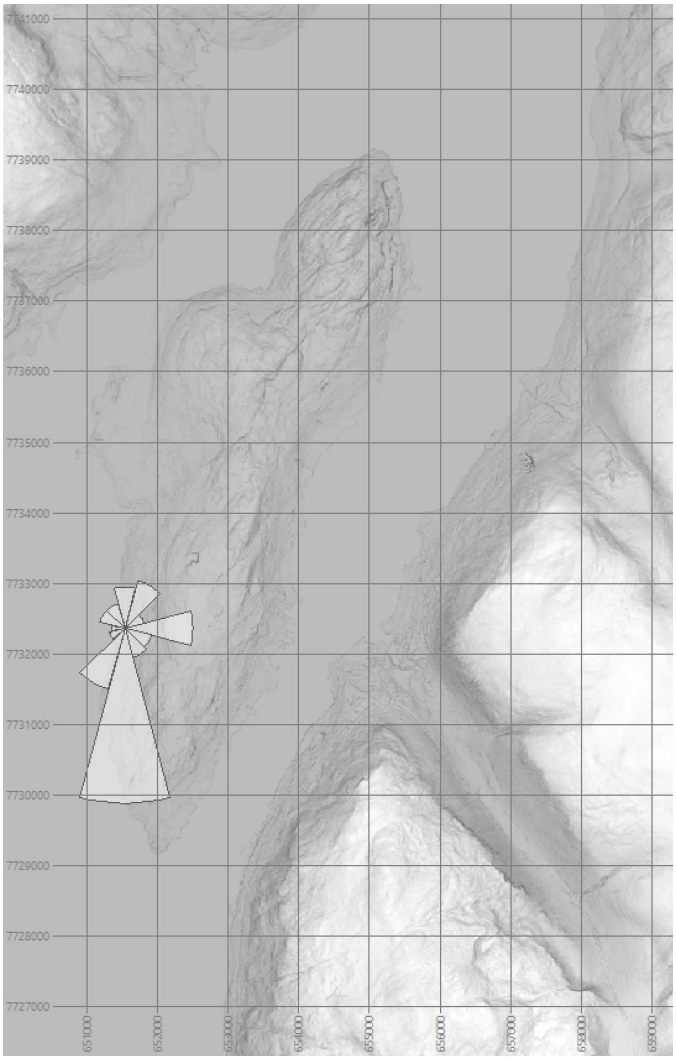

Figure 3.25: Openwind DTM and wind rose
Datum: WGS85 Proj.: UTM-33N

The grid size of the simulations was set to 50 m, any higher resolution resulted in the program crashing. A possible explanation to the problem is that the software version used (the free "Basic" version) does not allow for multithreading, and that the simulation crashes when becoming too computational intensive. Additionally, the software kept crashing when simulating including more than one wind rose, or a roughness layer. A roughness layer holds information of the approximate roughness lengths of land types in a classified landscape. Effectively, the limitations question the validity of the simulations and Openwind results are therefore only intended to compliment AFD results.

4

Results

4.1 Weather Data

Histograms and wind roses are chosen to analyze the weather data and explanations of the graphical representation methods are provided in section 3.1.5. Supplementary plots of weather data are available in appendix B.

4.1.1 Holt

Figure 4.1a and figure 4.1b are histograms illustrating the distribution of wind speed at Holt in 2015 respectively annually and seasonally. The distribution varies considerably with the seasons and the average wind speed from January until the end of March is 4.06 m/s, more than twice the average in the autumn (from July throughout September) with an average of merely 1.89 m/s. Notice that during January – March (dark blue in figure 4.1b) the most frequent wind speed interval is the one from 5 to 7.5 m/s.

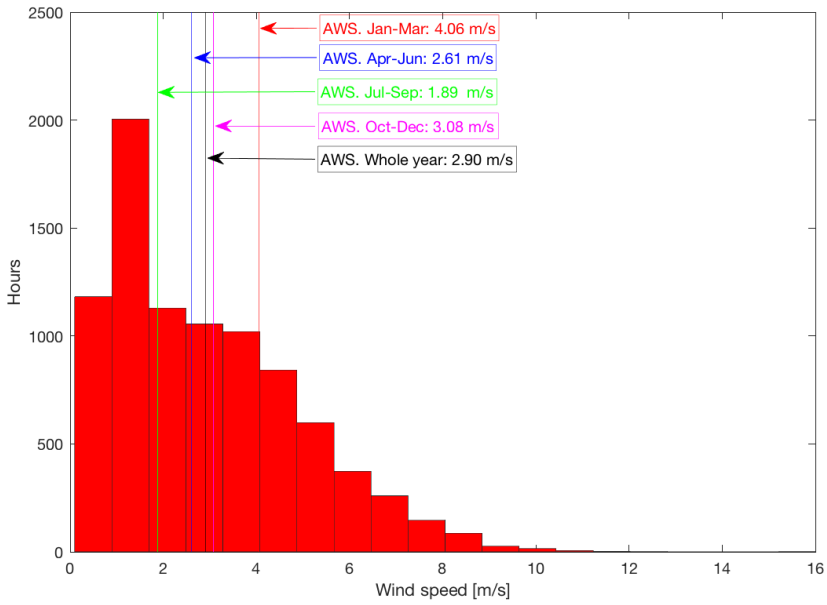

(a) Annually

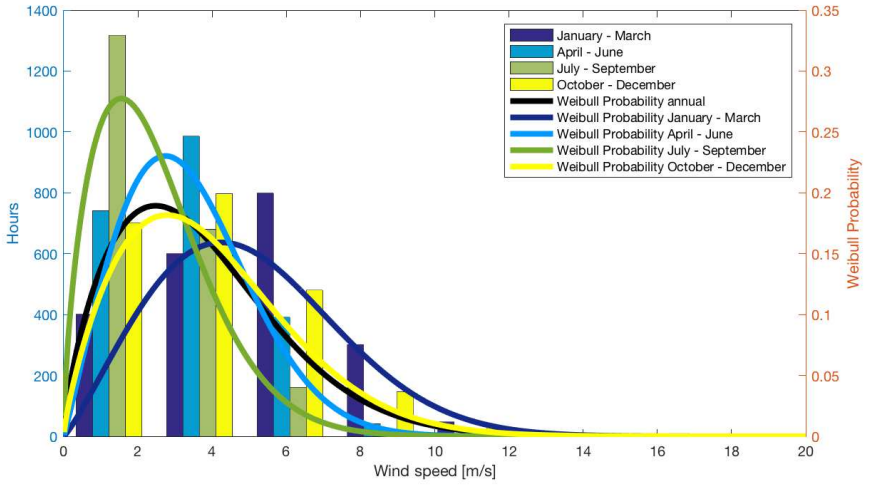

(b) Seasonally

Figure 4.1: Distribution of wind speed at Holt, 2015

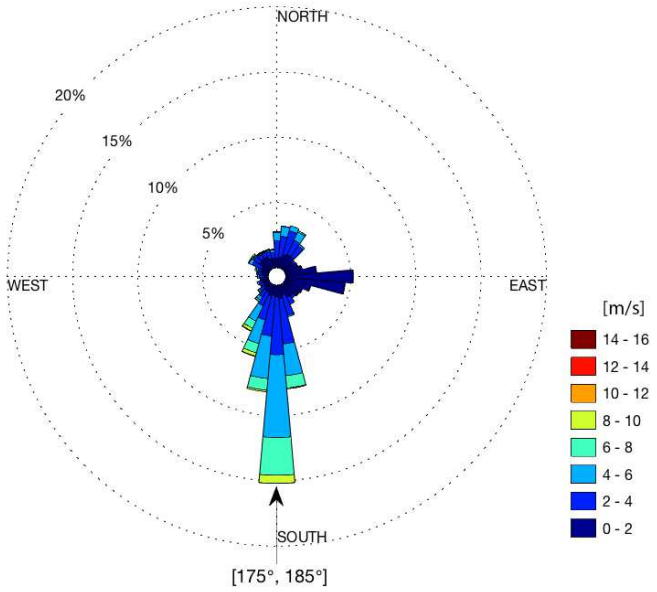

Figure 4.2: Wind rose from Holt, 2015

The wind rose from Holt 2015, figure 4.2, clearly shows that wind coming from the south and blowing north is the dominant direction of the wind. The interval 175° to 185° is by far the most frequent wind direction and represents about 15 % of the measurements. Expanding the interval to 165° - 215° increases the total share which now adds up to about 40 % of the measurements.

In addition, the wind is also sometimes blowing from the east and from the north-northeast, but not nearly as often as from the south. The wind from the south is also the strongest wind indicated in the color bands. Wind roses displaying seasonal variations at Holt can be viewed in appendix B.

4.1.2 Realfagsbygget

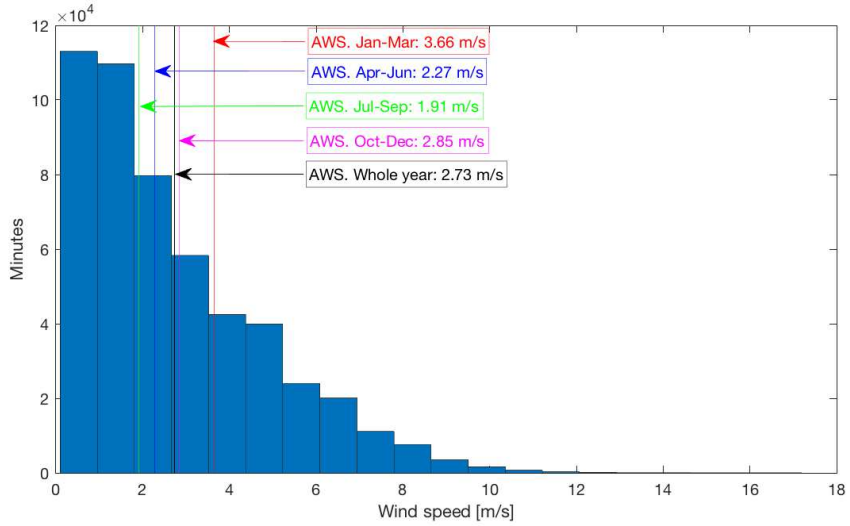

(a) Annually

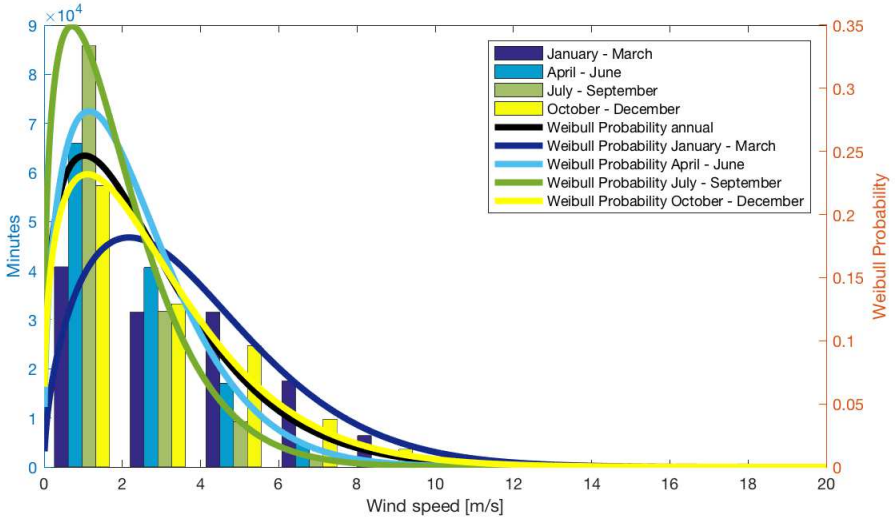

(b) Seasonally

Figure 4.3: Distribution of wind speed at Realfagsbygget, 2015

Figure 4.3a and figure 4.3b are histograms that illustrate the distribution of wind speed at Realfagsbygget in 2015 respectively annually and seasonally. The figures clearly show that relatively low wind speeds are more frequent compared to higher wind speeds, which is expected given the urban and low height location of the anemometer, see section 3.1.3. Also, the distribution changes quite considerably with the seasons.

Included in the histogram as references are the average wind speeds for the different seasons and the wind speed distribution.The average wind speed is higher in the winter seasons compared to the annual average, especially in the period of January to March 2015, with an average wind speed of 3.66 m/s.

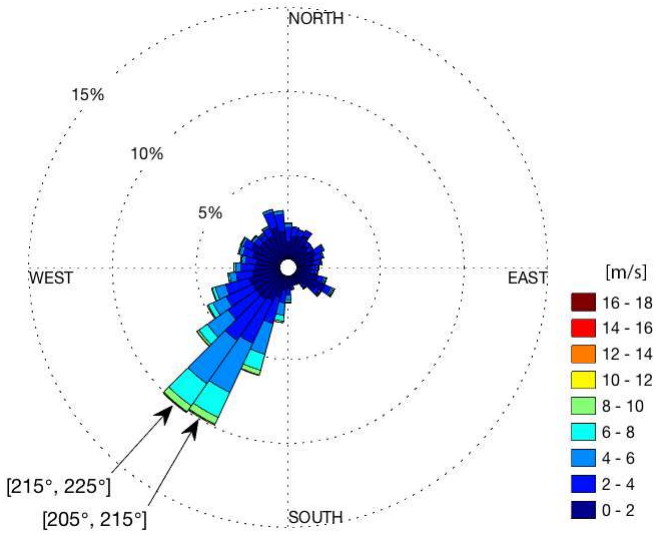

Figure 4.4: Wind rose from Realfagsbygget, 2015

Figure 4.4 presents the annual frequency of the wind directions and its corresponding speed at Realfagsbygget 2015. The intervals 205° to 215° as well as 215° to 225°are the most frequent directions of the wind with a combined frequency of about 20% in 2015 at Realfagsbygget. Also, the color bands indicate that the wind coming from these intervals in the south-southwest region are stronger. Wind roses displaying seasonal variations at Realfagsbygget can be viewed in appendix B.

4.1.3 Grønnåsen

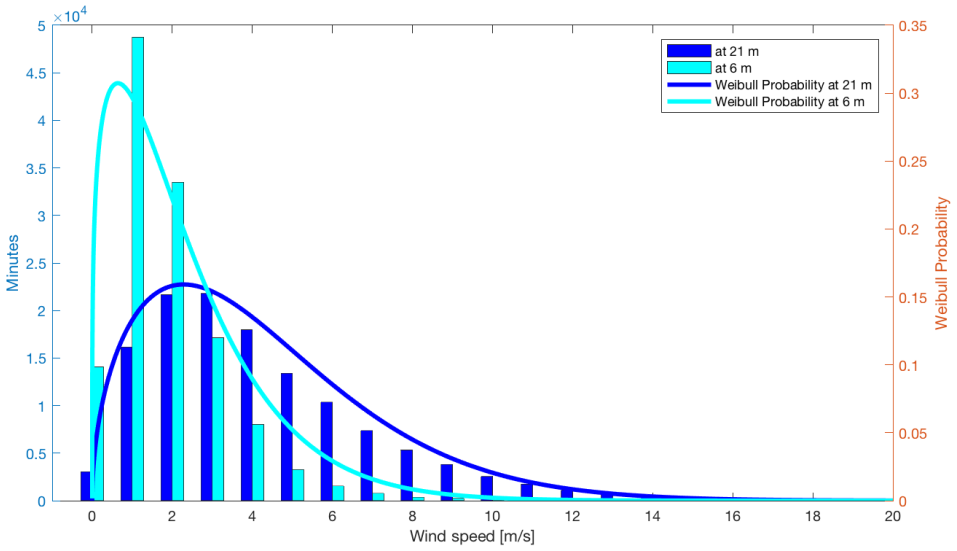

Figure 4.5: Distribution of wind speed at Grønnåsen, mid-February to mid-May 2017

Figure 4.5 is a histogram containing data from both the wind sensor mounted at 21 m AGL, as well as the one at 6 m AGL. As expected, the measured wind is clearly stronger at 21 m AGL, with an average of 4.22 m/s, compared to 1.88 m/s at 6 m AGL. It is important to emphasize that the histogram as well as the wind roses in figure 4.6 do not represent the annual distribution of wind speed and direction, but only the period from mid-February to mid-May.

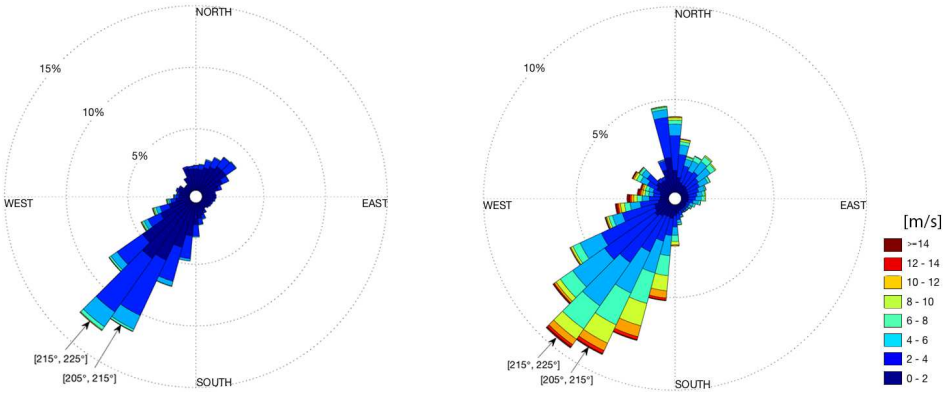

(a) at 6 m **(b)** at 21 m

Figure 4.6: Wind roses from Grønnåsen, mid-February to mid-May 2017 (the scale in the lower right corner belongs to both figures)

An estimated daily averaged wind power density at Grønnåsen at 21 m AGL in the period mid-February to mid-May is presented in figure 4.7 along with the wind speed as a reference. The figure illustrates that the daily averaged power density varies significantly within the period - one day the average was calculated to be about 1400 W/m^2 while other days had almost no power in the wind comparatively. The average wind power density in the period was estimated to be 135.3 W/m^2.

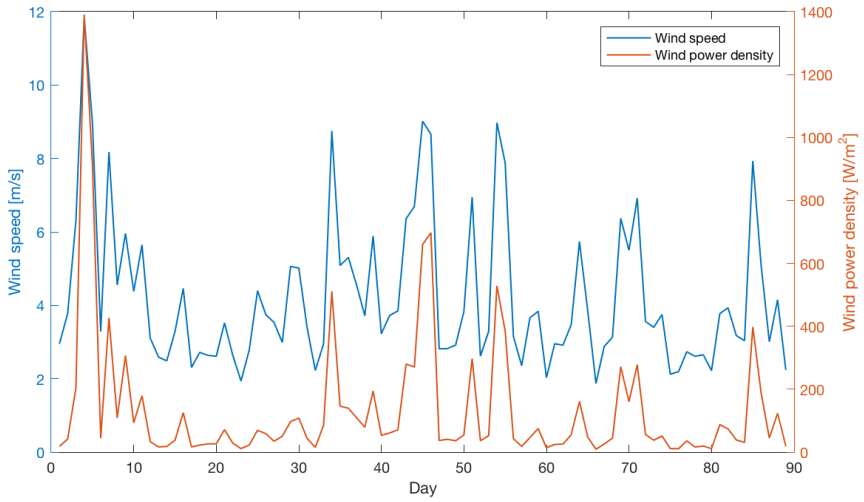

Figure 4.7: Wind power density at Grønnåsen, mid-February to mid-May 2017

The wind power density was calculated using equation 2.7 on 10. No temperature measurements at Grønnåsen are available and therefore the average temperature in the period at Holt was used to decide the air density in the calculations.

The power in the wind is an instantaneous value dependent on the velocity cubed. Therefore, using a linearly averaged wind speed to calculate the instantaneous power in the wind will result in underestimations, larger and more frequent wind speed fluctuations in the time period of the samples corresponds to bigger underestimations. Consequently, wind speed data sampled frequently is desired when estimating the wind power density.

At Grønnåsen the wind speed measurements are averaged over one minute. Therefore, the wind power density was first calculated for each minute and then averaged to a daily average value as presented in the graph of figure 4.7. The order of the operations is crucial to attain satisfactory estimations as switching it up will result in greater underestimations.

4.1.4 Comparison of the Data Sets

Wind Distribution at Holt and Realfagsbygget

Combining the data of multiple annual wind roses with a contour map may provide a better understanding of the air movement trends in the region. Figure 4.8 is a contour map of Tromsø with the locations of two weather stations pinpointed by red circles and their corresponding wind roses from 2015 are added. Only the wind roses from Holt and Realfagsbygget are added as the sensors at Grønnåsen have not been logging continuously for a whole year. The black contour lines show elevations of 100 m intervals, denoted by labels, and the green lines are intervals of 20 m.

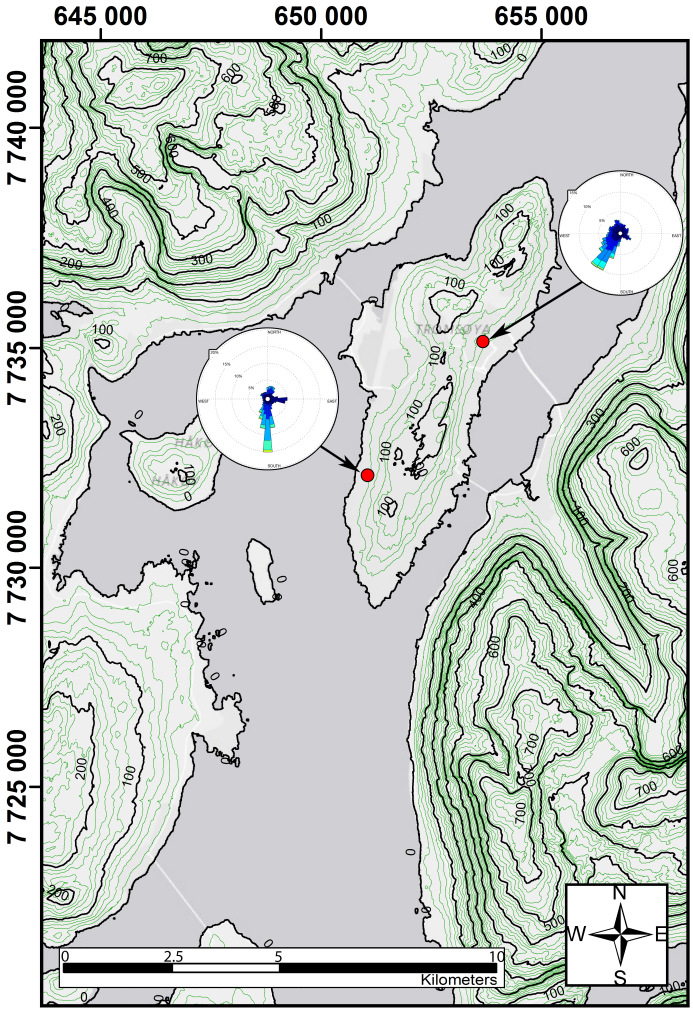

Figure 4.8: Contour map of Tromsø with annual wind roses, 2015
Datum: WGS85 Proj.:UTM-33N

It appears that most frequently the flow of the air follows the fjord and blows from the inland (middle lower edge of figure 4.8) towards the sea (upper right corner of figure 4.8). Also, it is reasonable to assume that the wind is somewhat stratified and tends to maintain at the same elevation and will therefore bend in the direction of the contour lines. Indication of the described effect is seen in that both the presented wind roses show an annual distribution of wind moving in a direction close to parallel to the contour line at the location of the weather station.

Regarding the wind speed, the two data sets are more comparable to the direction of the wind. The annual average wind speed at Holt weather station is slightly higher than at Realfagsbygget at 2.90 m/s compared to 2.73 m/s. The same relation holds for the season with the highest average wind speed, January – March. In this period of the year the average wind speed at Realfagsbygget was 3.66 m/s compared to 4.06 at Holt.

Correlation Between Grønnåsen and Holt

Merely three months of wind measurements at Grønnåsen are not adequate for compiling a statistical analysis of the annual distribution of the wind at the location. To address the issue of insufficient data, the set is compared to another data set from Tromsøya of a much longer time series - Holt at 2 m AGL.

A comparison of the daily averaged wind speed at Grønnåsen and Holt from mid-February to mid-May 2017 is provided in figure 4.9. The red line represents variations at Holt, 2 m AGL, and the blue lines belong to data from Grønnåsen at two different heights, 6 m AGL (light blue) and 21 m AGL (dark blue). During the three months, the daily averaged wind speed changed considerably. For example, for all three sets of data from the 12^{th} of February 2017 (4^{th} day in the sets) had an average of more than 3 times the average just two days later.

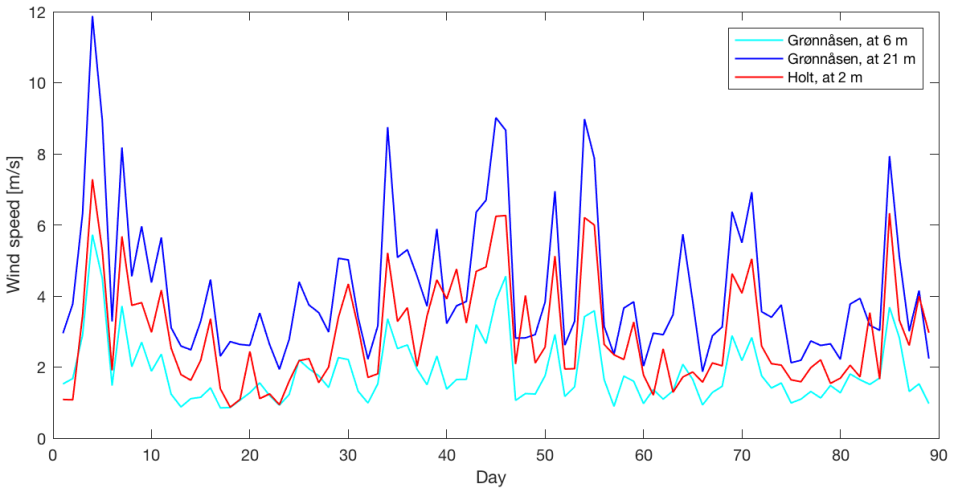

Figure 4.9: Comparison of daily averaged wind speed at Grønnåsen and Holt, mid-February to mid-May 2017

While the correlation between the data sets regarding wind speed is illustrated in figure 4.9, an enhanced understanding of the correlation can be obtained by calculating a correlation coefficient.

Table 4.1 contains calculations of the Pearson correlation coefficient between measured wind speed at Holt and at Grønnåsen. The coefficient is only sensitive to the linear relationship between two sets of data and a coefficient of +1 indicates a direct linear correlation. The table shows that measurements from the sensor mounted at 21 m AGL at Grønnåsen correlates slightly more to the Holt data compared to measurements at 6 m AGL. In addition to the coefficient, the average wind speed at the location is also presented throughout the whole period.

The average wind speed from Grønnåsen at 21 m AGL was 4.22m/s, 1.45 times the average at Holt at 2 m AGL. A far lower average of 1.88 m/s was measured at 6 m AGL at Grønnåsen. It corresponds to 0.65 times the average at Holt at 2 m AGL and 0.45 times the average at 21 m AGL at the same location. The relatively low wind speed average at Grønnåsen at 6 m AGL might be due to the sensor being located within a birch forest of approximately 11-12 m AGL.

Data set	Wind speed average [m/s]	Correlation to Holt at 2 m	
		Hourly	Daily
Holt at 2 m	2.91		
Grønnåsen at 6 m	1.88	0.67	0.84
Grønnåsen at 21 m	4.22	0.73	0.87

Table 4.1: Wind speed averages and data set correlation (Pearson), mid-February to mid-May 2017

Predicted Vertical Wind Profile at Grønnåsen

A few options for predicting the average vertical wind shear at Grønnåsen from mid-February to mid-May 2017 is presented in figure 4.10. Mutual for all the curves is that they adhere to the wind shear power law equation 2.1 described on page 7. They differ in the value of wind shear exponent (see section 2.1.2 on page 7 for explanation on the shear exponent), β, and the measurement(s) used as reference(s). Solid curves use the average wind speed at 6 m AGL as a reference while the dotted curves indicate the average wind speed at 21 m AGL.

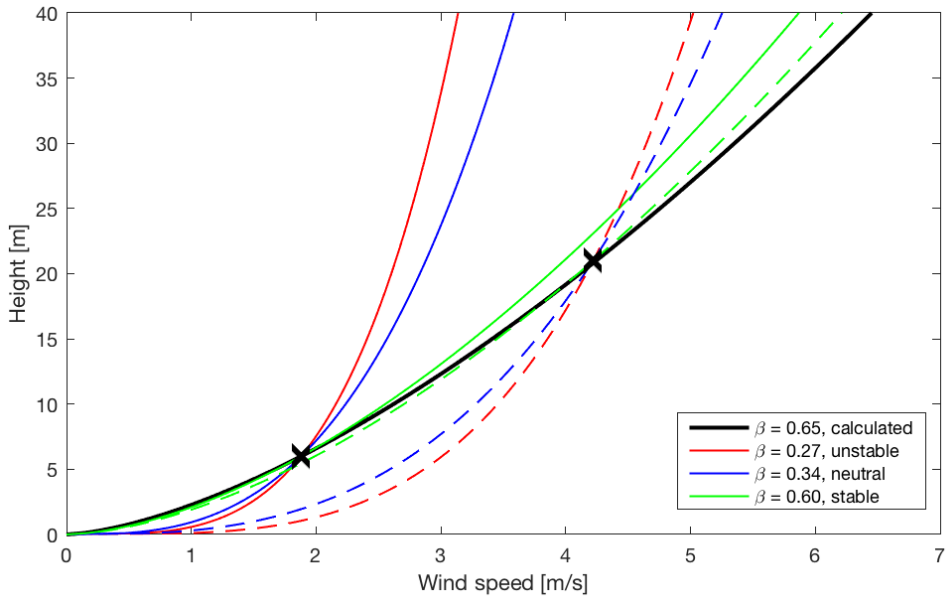

Figure 4.10: Vertical wind profile predictions, at Grønnåsenat mid-February to mid-May 2017. Solid curves use the average wind speed at 6 m AGL as a reference while the dotted curves indicate the average wind speed at 21 m AGL

Except for $\beta = 0.65$, the values used for the wind shear exponent are taken from table 2.1. They represent typical values in an urban environment of different atmospheric states. The black solid curve differs as it applies a wind shear exponent calculated so that the curve fits both the measured references and wind speed averages. It is therefore most likely the best predicted vertical profile offered in figure 4.10.

The value of the calculated wind shear exponent is close to the typical value seen for a stable atmospheric state in an urban environment, but it does not imply that the atmospheric state at Grønnåsen is stable. Also, while an exponential fitted curve may provide sufficient accuracy inbetween fitted points it cannot guarantee reliability beyond those points. Therefore, the predicted vertical wind profile cannot be utilized as an example in this case to accurately predict at what height an average wind speed of more than 8 m/s is reached.

Nevertheless, the black curve suggest that one must be at 40 m height at this location to reach an average wind speed of 6.5 m/s, which is considered by the Norwegian Ministry of Petroleum and Energy to be the lower limit to produce commercially viable wind power (Norwegian Ministry of Petroleum and Energy 2015, 28).

4.2 Flow Simulations

4.2.1 Tromsøya

Inlet Velocity Dependency

Figure 4.11 indicates that there are little or no variations of significance between the areas of highest wind speed simulating 3 m/s and 6 m/s as inlet velocities for the Tromsøya 3D-model with wind coming from 200°. The same results of negligible velocity dependency were also found when simulating the two other inlet wind directions of 180° and 190°.

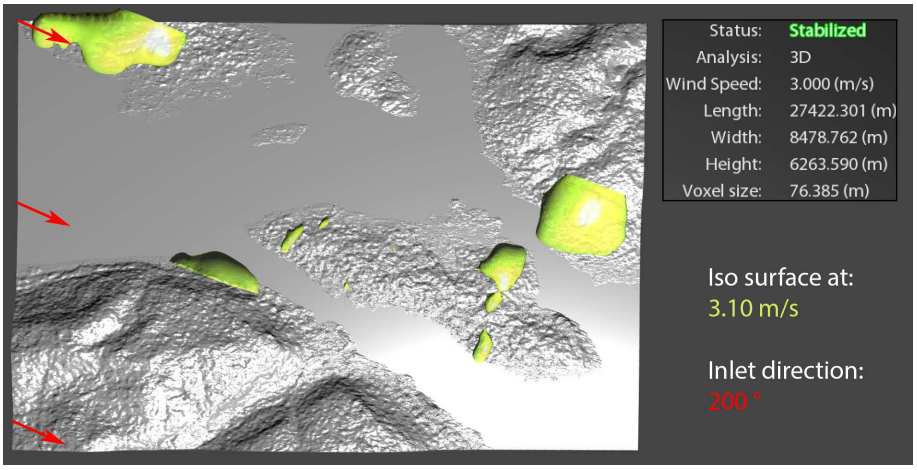

(a) From above, 3 m/s

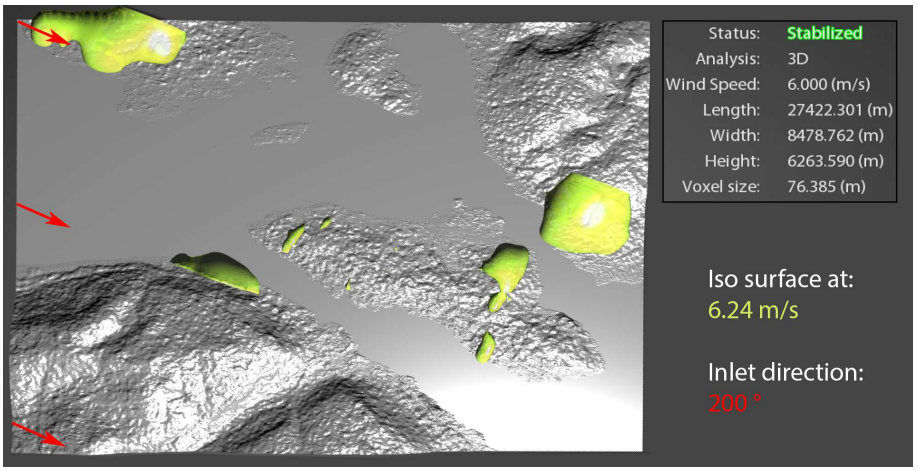

(b) From above, 6 m/s

Figure 4.11: Inlet velocity dependency, Tromsøya, 200°

Inlet Direction Dependency

The figure 4.12 shows the areas of the highest wind speed using 3 m/s as inlet velocity with three different inlet directions of wind. It is quite clear that the areas vary with the direction of the wind, but at the same time they share a common area of relatively high wind speed. When choosing to display the same wind speed iso surface for all three simulated inlet directions it often proved to be inappropriate. While a wind speed iso surface was of satisfactory size simulating wind from one direction, it was not necessarily for other directions in which the regions could be widespread or even absent. Consequently, it was decided to present regions of relatively similar size, but of slightly different wind speed.

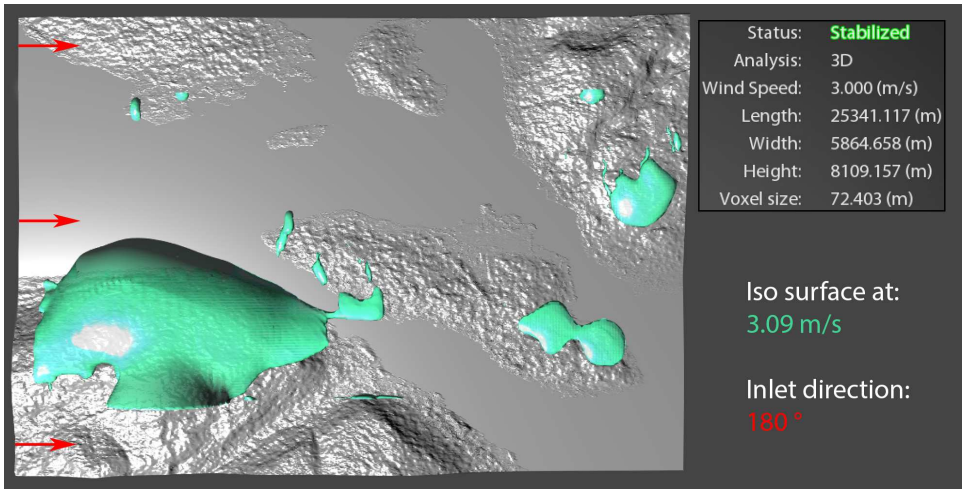

(a) 180°

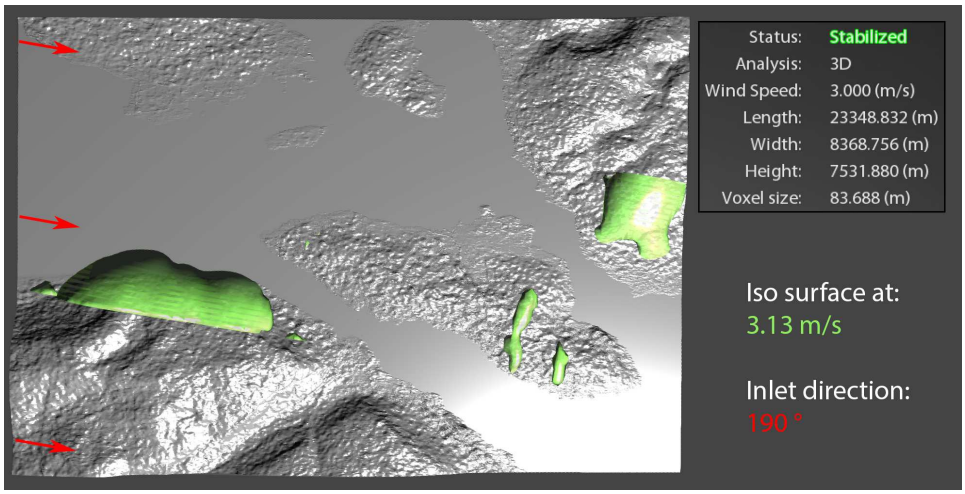

(b) 190°

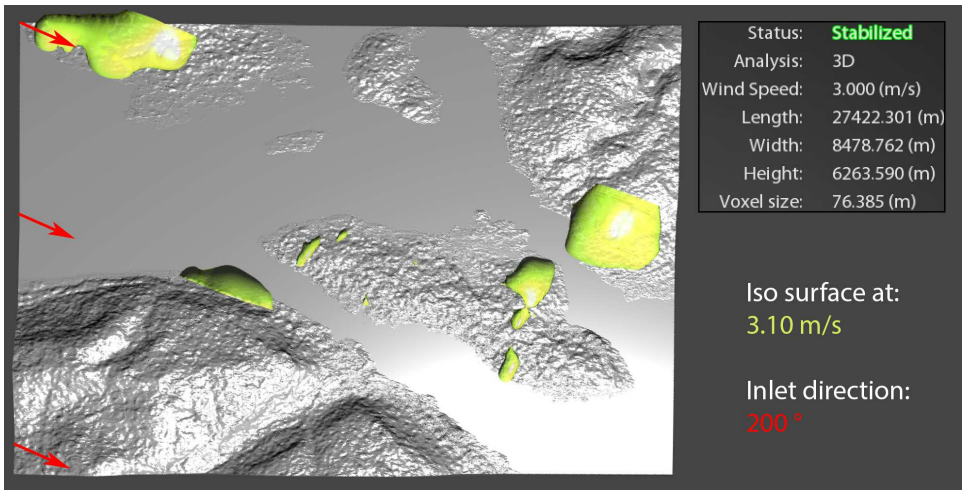

(c) 200°

Figure 4.12: Inlet direction dependency, Tromsøya, viewed from above, 3 m/s

A comparison of the high-speed regions corresponding to the different simulated inlet directions is presented in figure 4.13. It is simply a combination of the regions from figure 4.12 and an image of Tromsøya 3D-model as it appears with the imagery of Microsoft's Bing Maps draped over the topography. The locations of the wind sensors at Realfagsbygget and Holt have been added in addition to a compass star.

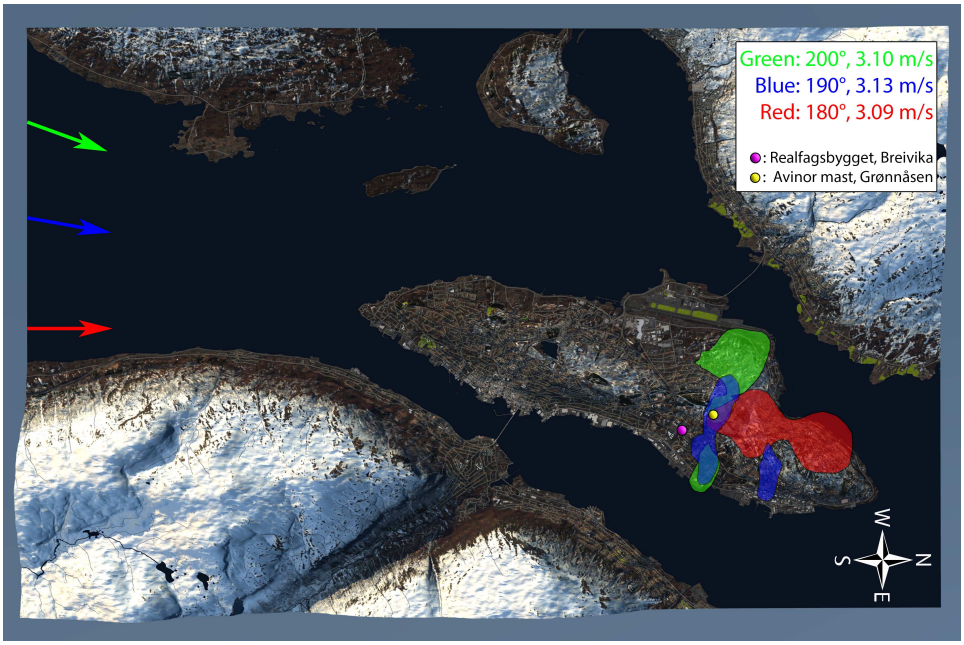

Figure 4.13: High-speed regions combined, 3 m/s

Nature of Simulated Flow

Visualizing the path of a certain quantity of fluid parcels using flow lines is a great aid to study the general flow behavior in the region. Figure 4.14 shows flow lines all the way from the surface of the model to 160 m a.s.l., roughly 10 m above the highest elevated point at Tromsøya. It appears that the flow separates to some extent when reaching the southern part of Tromsøya, then widens out over the island and starts the process of connecting at the end of it. Similar patterns were observed when simulating other inlet directions and wind speed values.

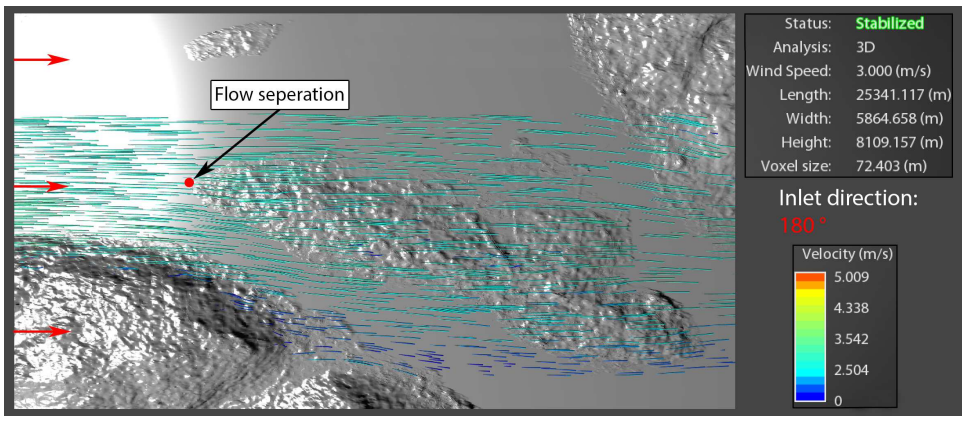

Figure 4.14: Flow lines, Tromsøya, 180°, 3 m/s

Notice that in the region of Realfagsbygget the wind is marginally bended towards the west while the direction of the wind at Holt is similar to the inlet wind direction of 180°. Comparing the simulation to the wind measured at ground level (see figure 4.8 on page 76) indicates that the direction of the wind is distributed differently at the surface level relative to elevated layers.

4.2.2 Realfagsbygget

Inlet Velocity Dependency

Similar to the results using the Tromsøya 3D-model, the locations of the high-speed regions were observed to be close to independent of the inlet wind speed when simulating Campus 3D-model 1. An example presenting simulations using 3 m/s and 6 m/s as inlet velocities is provided below in figure 4.15.

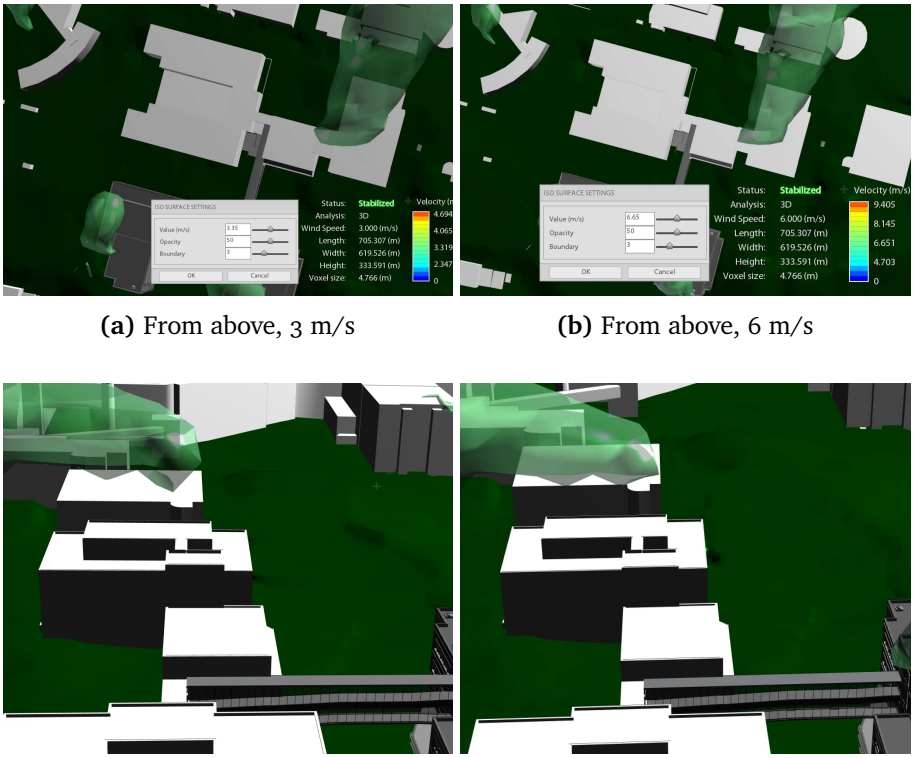

(a) From above, 3 m/s **(b)** From above, 6 m/s

(c) From frontside, 3 m/s **(d)** From frontside, 6 m/s

Figure 4.15: Inlet velocity dependency, Realfagsbygget, 205°

Inlet Direction Dependency

Figure 4.16 shows the areas of the highest wind speed using 3 m/s as inlet velocity on Campus 3D-model 1 with three different inlet directions of wind. A combination of the regions is presented all together in figure 4.17. Unfortunately, AFD does not provide an option for adding scale bars. Note that the scale bar in figure 4.17 can only be used as an approximated scale as it is simply added to the image. The height from the ground to the top of the roof is measured at 18.9 m and is used as a reference length to the scale.

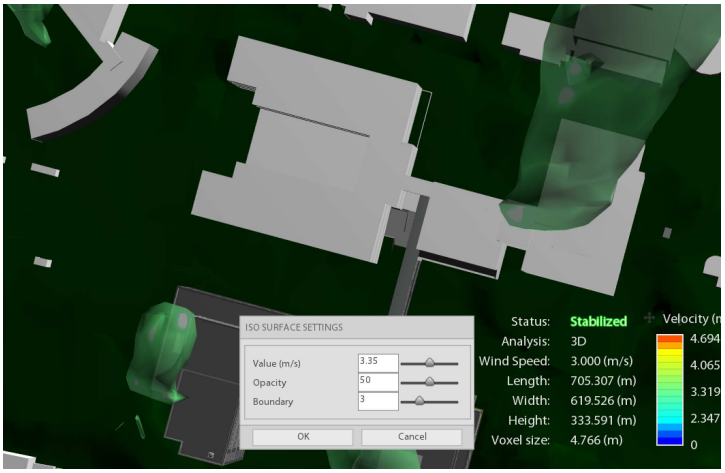

(a) 205°

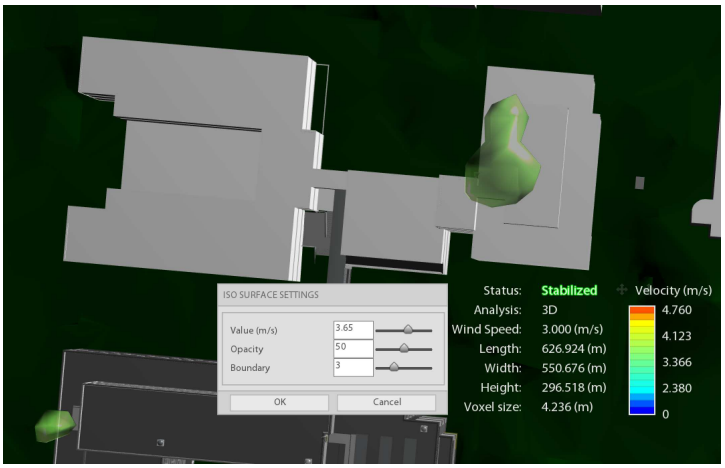

(b) 215°

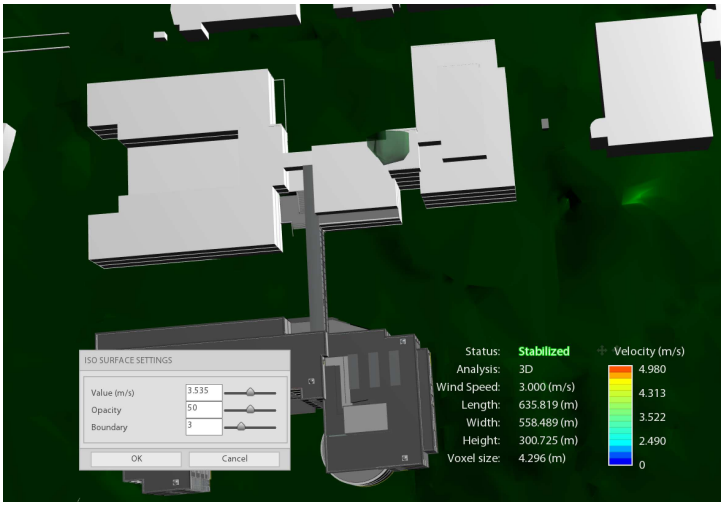

(c) 225°

Figure 4.16: Inlet direction dependency, Realfagsbygget, viewed from above, 3 m/s

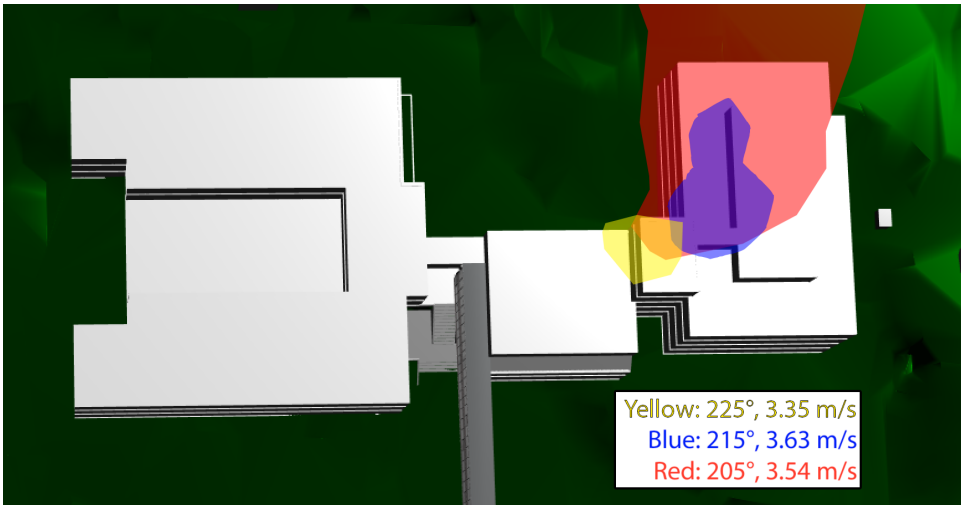

(a) From above

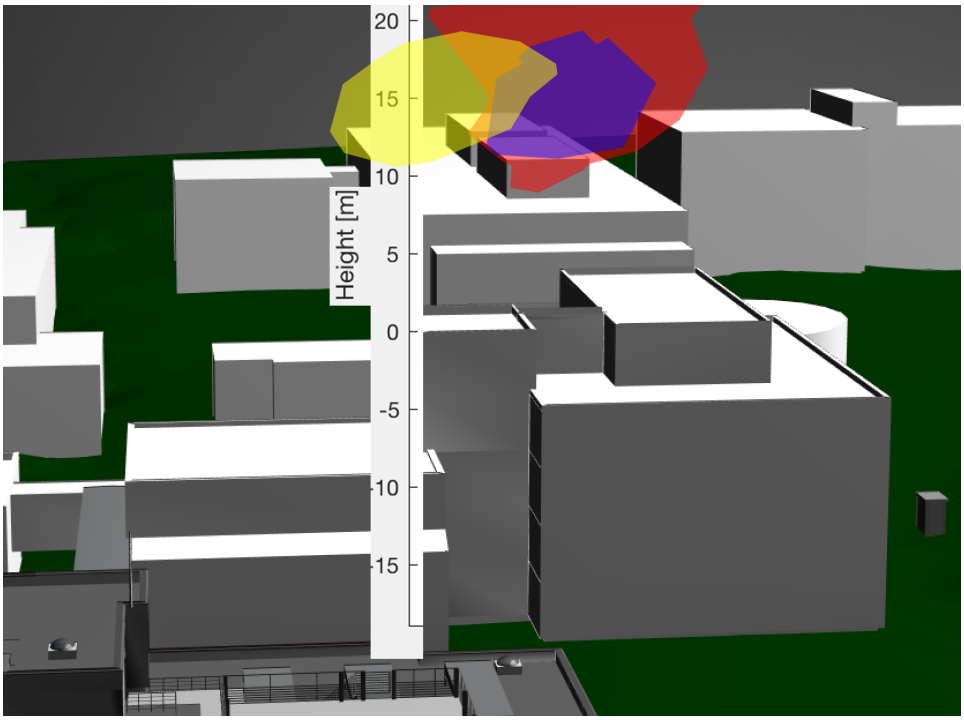

(b) From the side

Figure 4.17: High-speed regions combined, Realfagsbygget, 3 m/s

Nature of Simulated Flow

Figure 4.18 demonstrates important areas of separation and deflection highlighted by the red arrows. Here, flow lines are used for simulation visualization to show trends more clearly. Even though the flow lines are only visible in a small section, the flow of the invisible fluid in the VWT is still simulated as its behavior affects the visible flow lines.

A substantial amount of air is channeled to the open space in the center of A-Wing and is later deflected up towards B-Wing and then C-Wing and is responsible for higher wind speed on the south side (right side of figure 4.19) of the roof of C-Wing. Similar behavior is also observed when simulating with the other two inlet wind directions, 205° and 225°.

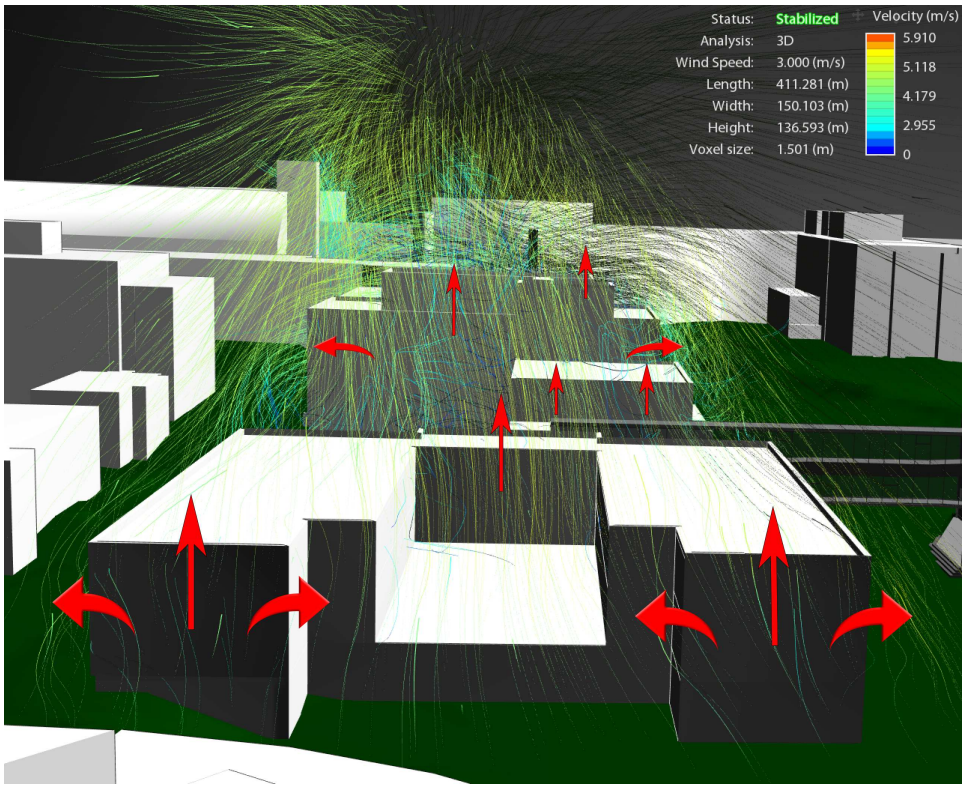

Figure 4.18: Areas of separation and deflection, Realfagsbygget, 215°, 3 m/s

A characterization of the fluid flow regarding turbulence is presented in figure 4.19. Figure 4.20 highlights turbulent behavior by exploiting smoke flow lines as the path of low-velocity fluid parcels are more visible. Similar behavior is also observed for the other two simulated inlet wind directions, 205° and 225°.

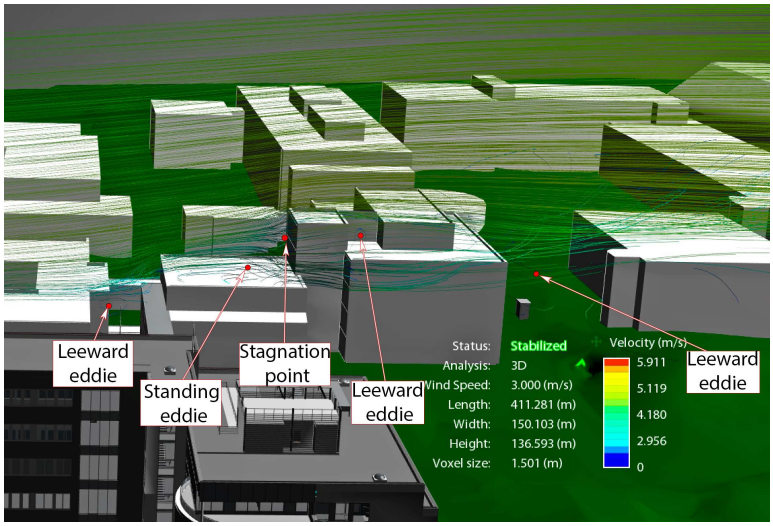

Figure 4.19: Formation of turbulence, Realfagsbygget, 215°, 3 m/s

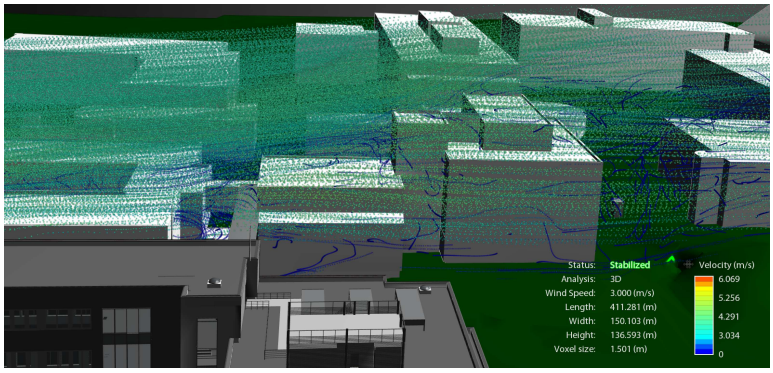

(a) From the side

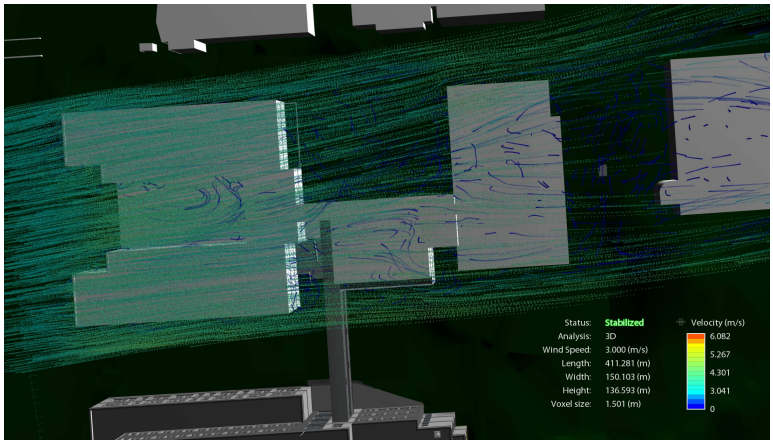

(b) From above

Figure 4.20: Smoke flow lines, Realfagsbygget, 215°, 3 m/s

4.2.3 Grønnåsen

Inlet Velocity Dependency

The locations of the high-speed regions appear to be independent of inlet wind speed when simulating the Grønnåsen 3D-model, which coincides with the results of other models. An example illustrating the independency is presented in figure 4.21.

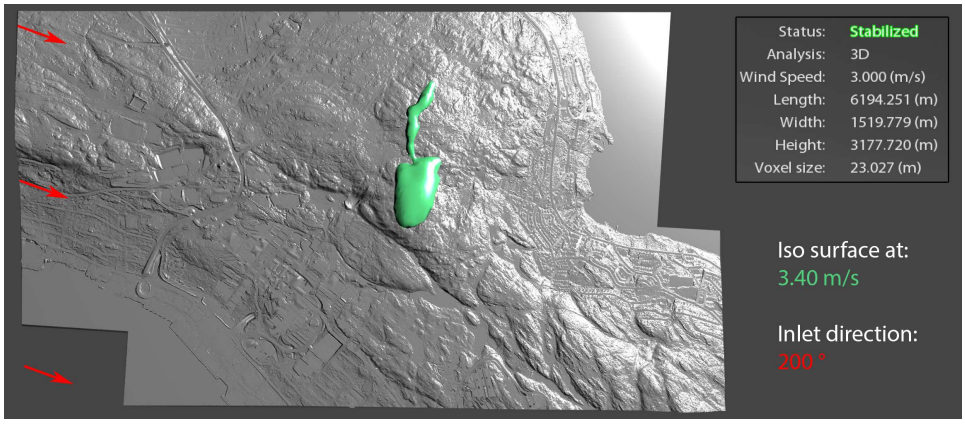

(a) From above, 3 m/s

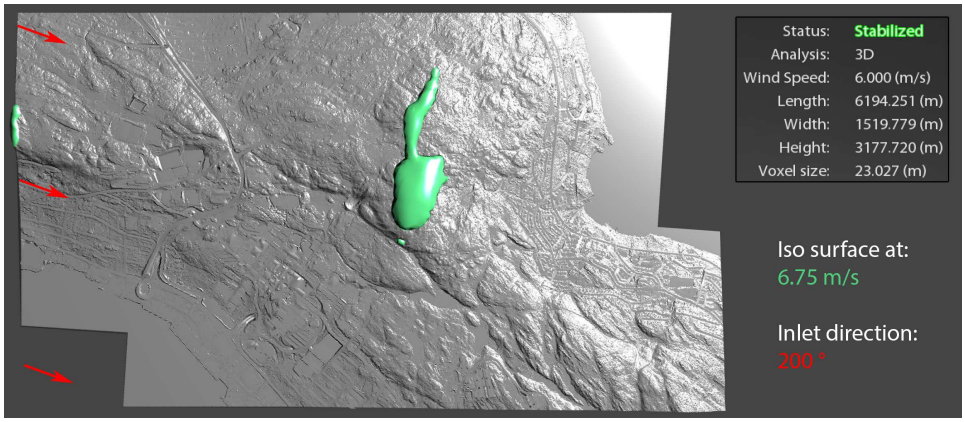

(b) From above, 6 m/s

Figure 4.21: Inlet velocity dependency, Grønnåsen, 200°

Inlet Direction Dependency

Figure 4.22 shows the areas of the highest wind speed using 3 m/s as inlet velocity in the Grønnåsen 3D-model with three different inlet directions of wind. A combination of the regions is presented all together in figure 4.23.

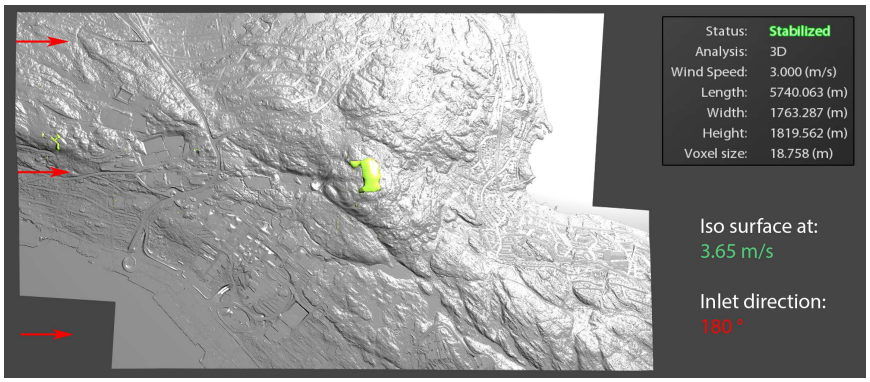

(a) 180°

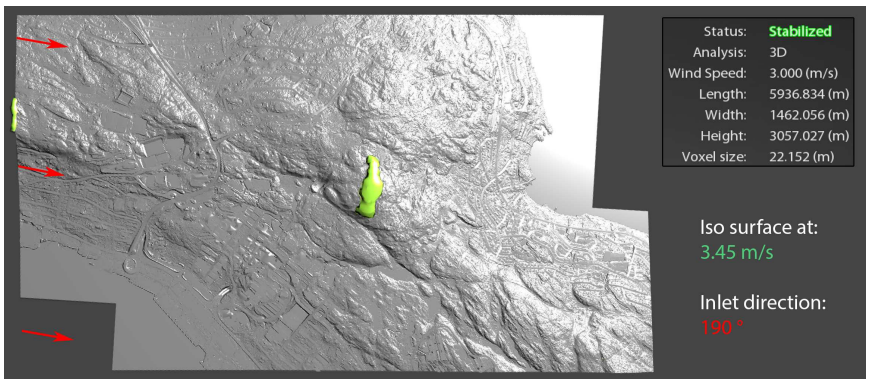

(b) 190°

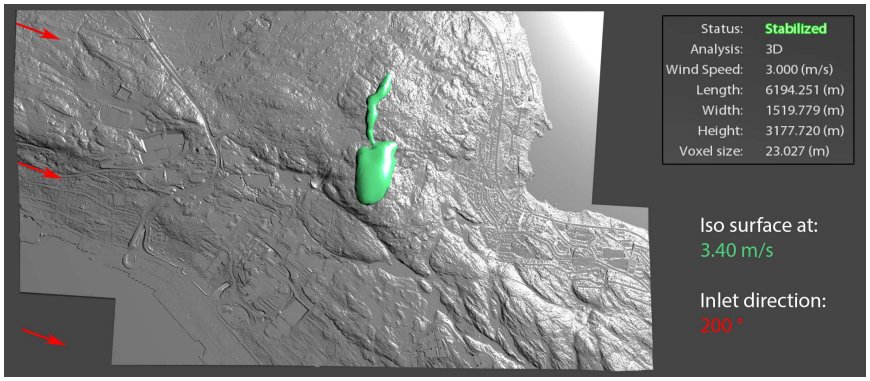

(c) 200°

Figure 4.22: Inlet direction dependency, Grønnåsen, viewed from above, 3 m/s

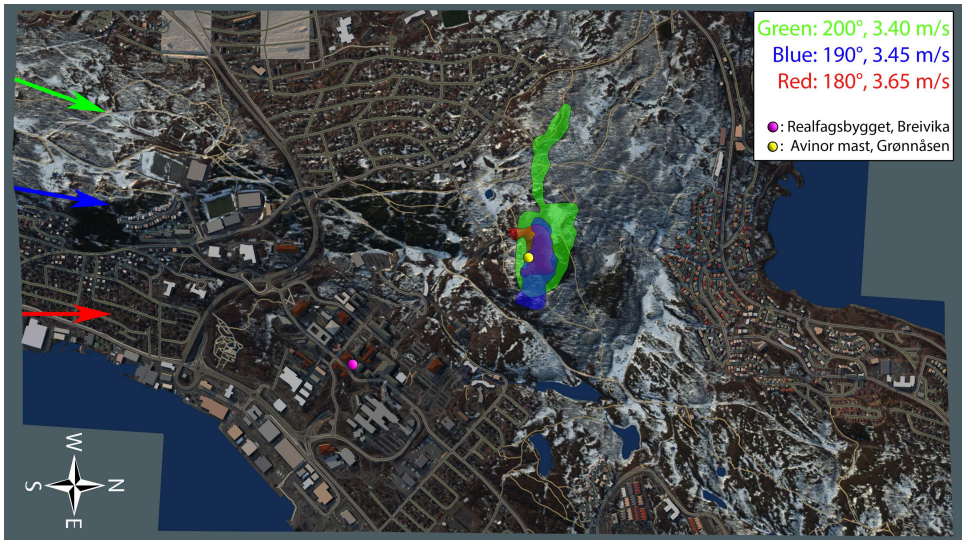

Figure 4.23: High-speed regions combined, Grønnåsen, 3 m/s

Nature of Simulated Flow

Figure 4.24 shows flow lines in the region upstream of Grønnåsen. The hilltop seen at the end of the visualized flow is Grønnåsen, with the ski jumping arena barely visible in front of it. The flow appears to be of laminar nature, only a few meters above the terrain and buildings.

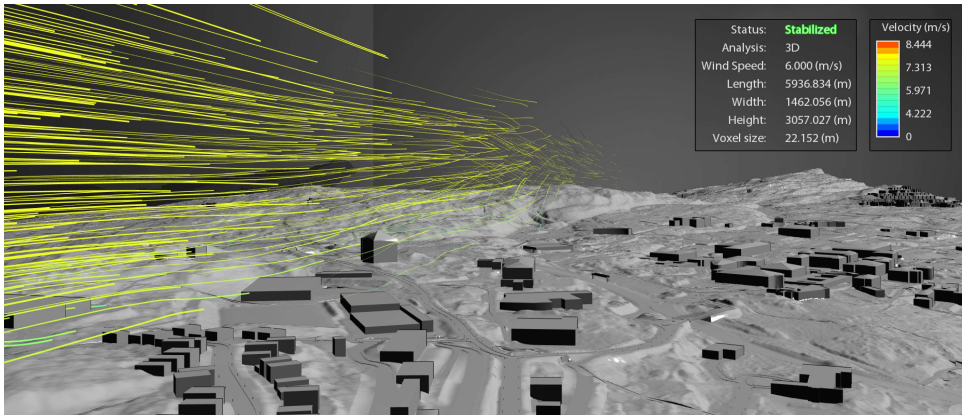

Figure 4.24: Flow lines, Grønnåsen, 190°, 6 m/s

4.2.4 AWS Truepower - Openwind

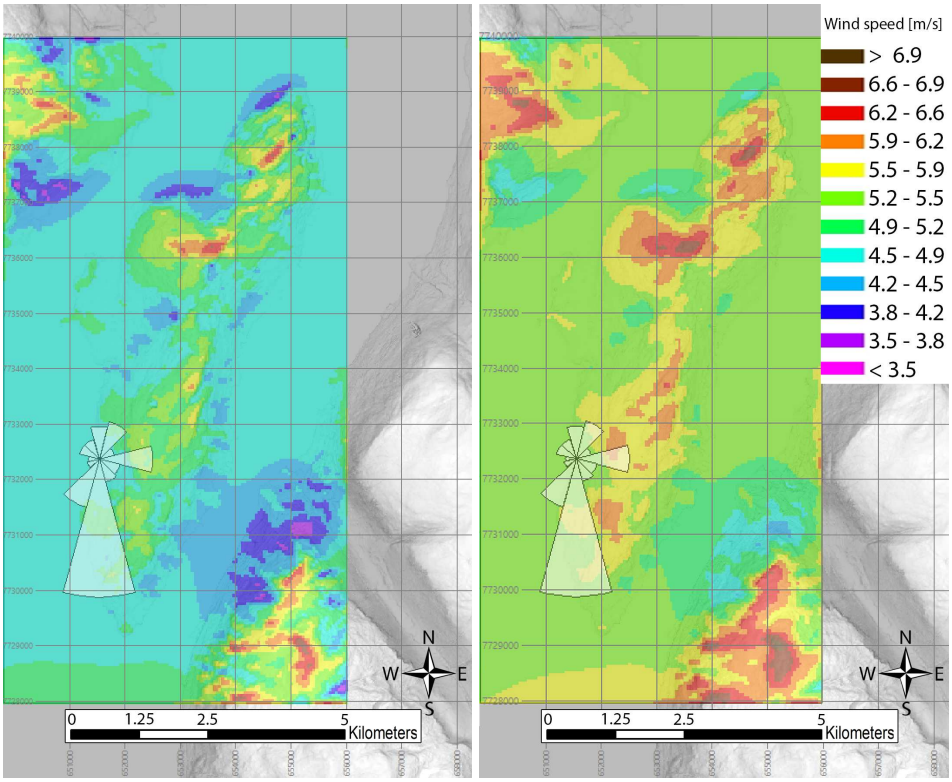

(a) Tromsøya at 20 m AGL **(b)** Tromsøya at 50 m AGL

(c) Grønnåsen at 20 m AGL **(d)** Grønnåsen at 50 m AGL

Figure 4.25: Estimated annual distribution of wind speed averages
Datum: WGS85 Proj.:UTM-33N
(the scale in the upper right corner belongs to all the figures)

Figure 4.25 shows the annual distribution of wind speed averages estimated with Openwind at two levels, 20 and 50 m AGL. The simulation is based on two sources of data; a DEM of a 10 m resolution and a weather data set from Holt containing hourly averaged measurements of wind speed, wind direction and temperature for an entire year (2015). The simulation mesh has a grid size of 50 m.

The figure below, figure 4.26, does also demonstrate estimated wind speed averages, but differs from figure 4.25 in that the averages are calculated for a certain wind direction at every grid point. Note that it is not the same as the *inlet* wind direction, which is a boundary condition set by AFD. Simulations showing the distribution for other wind directions are found in appendix C.

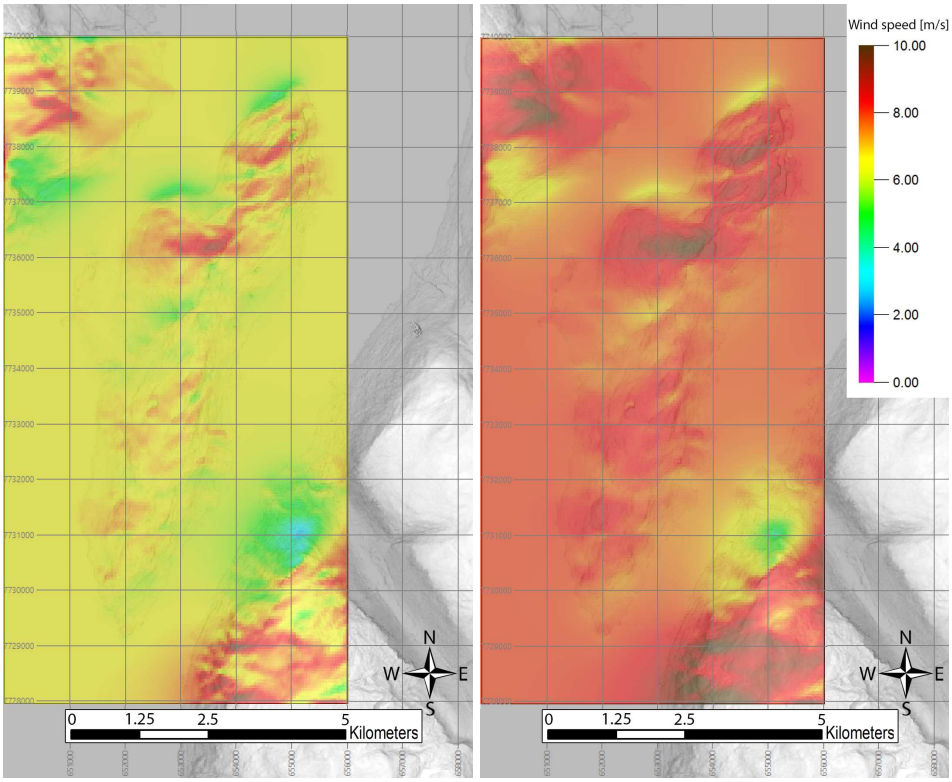

(a) Tromsøya at 20 m AGL **(b)** Tromsøya at 50 m AGL

Figure 4.26: Estimated annual distribution of wind speed averages from 180°.
Datum: WGS85 Proj.:UTM-33N
(the scale in the upper right corner belongs to both figures)

4.2.5 Comparison of the Simulations

AFD and Openwind differ significantly in their approach to locating regions of high wind speed. While AFD, like any other CFD based program, solves the fluid flow directly, Openwind is based on GIS and attempts to predict the distribution of wind speed averages based on a DEM and a data set containing weather data. Therefore, a comparison of the results obtained by the two methods is intriguing. Figure 4.27 combines the results seen in figure 4.23 and figure 4.25. Openwind results are placed above and below their locations to perceive all the results at once, the arrows points to their respective outlines.

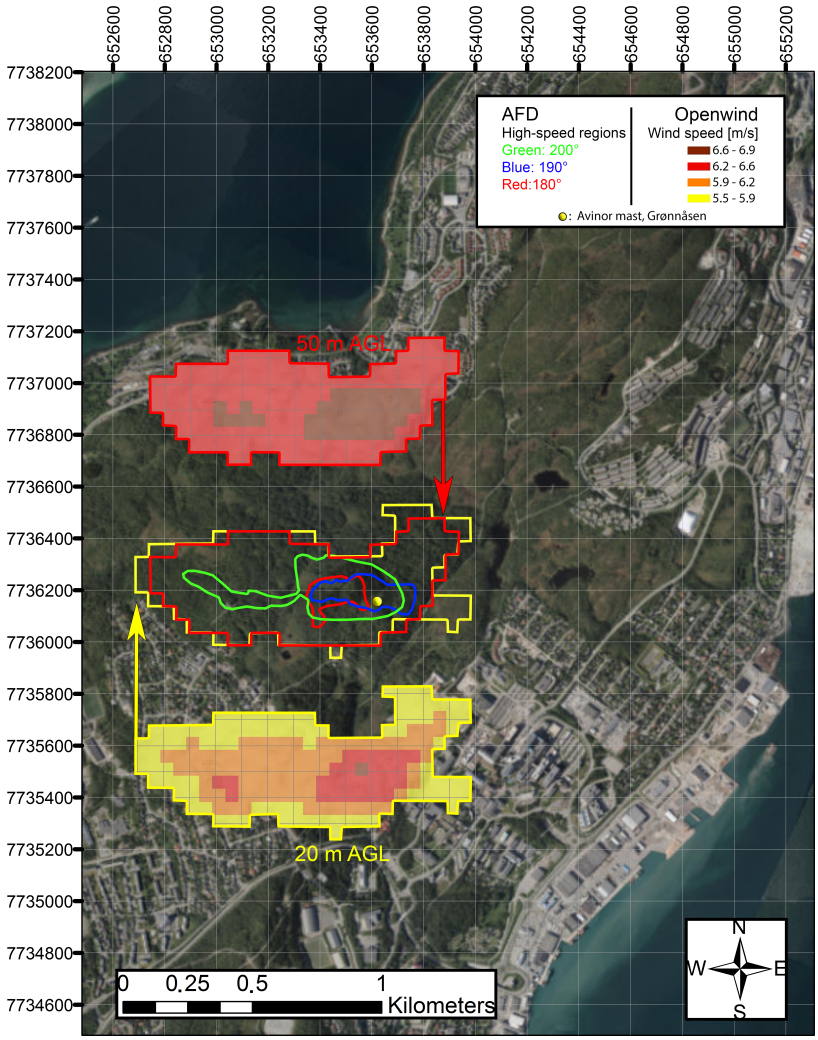

Figure 4.27: Comparison of AFD and Openwind simulations
Datum: WGS85 Proj.:UTM-33N

5 Discussion

5.1 Choice of Computer Tools

5.1.1 Building the 3D-models

To build the proprietary 3D-models used in this study the power of three programs was combined; QGIS, Quick Terrain Modeler by Applied Imagery and Autodesk InfraWorks 360. QGIS worked effectively for its intended use – to merge and prepare DTMs to be imported in InfraWorks. LIDAR data in the form of a point cloud was managed in Quick Terrain Modeler. The program produced highly-detailed DSMs as intended. Unfortunately, the level of detail was far too fine to be processed in InfraWorks. Therefore, a 1 m DTM holding elevation information about the terrain, more precisely the bare ground, produced of the classified LIDAR data was instead used in the process of building Grønnåsen 3D-model.

InfraWorks combines multiple layers of information, such as a DEM and a layer containing buildings, producing a TIN model to be used in flow simulations. Unfortunately, every time the 3D-model to be exported exceeded 2.2 GB the software crashed. 2.2 GB was also the limit when using another far less powerful computer. Except for these issues, InfraWorks satisfied its intended purpose.

5.1.2 Flow Simulation

The main application used for wind simulation in this study is Autodesk Flow Design. AFD is developed to be "extremely geometry tolerant" (Autodesk 2014, 2) and provide reasonably accurate results, hence why this program was chosen. However, quite a few shortcomings of the program were detected. They are as follows:

- **Limited boundary condition options.** Other than the 3D-model itself, the only inputs available were the wind speed and direction. There was no option for setting a gradient wind profile at the inlet. The absence of a gradient wind profile is problematic as the vertical scales in the simulations indicate sizes where the inlet wind speed at the pinnacle would be significantly higher than at the surface level.

- **No option to choose discretization method and turbulence model.** AFD uses the Finite Volume Method to discretize the fluid equations and the turbulence model Large Eddy Simulation (Autodesk 2014, 2). These two options are likely the best ones for the simulation length scales and the computational power available. Nevertheless, comparing the results to simulations using other discretization methods and turbulence models would be valuable.

- **Few tools for measurements.** AFD does not provide any tools for inserting length scales, neither can simulation values be extracted. Hence, the simulation results are restricted to the visualization alone.

Due to the clear limitations of AFD, other more powerful CFD alternatives, such as Autodesk CFD and COMSOL Multiphysics, were explored. COMSOL is not compatible with Infraworks file formatting. Autodesk CFD is a far more advanced version of AFD and supports the file formats of the 3D-models produced. Unfortunately, the program was unable to handle the processing load of creating a simulation mesh. When contacting Autodesk support, it was concluded that the models were far too complex to be processed by Autodesk CFD. The staff suggested reducing the number of faces with Autodesk Meshmixer. Yet, Meshmixer also crashes mid-process when processing the 3D-models. Perhaps a more powerful computer would do the job.

The GIS-based software Openwind by AWS Truepower is used to compliment the results obtained from AFD. Due to cost restrictions, the free version of Openwind was used. Along with other limitations, the basic version is incapable of multithread solving, thus restricting it to solve on only one processor. The processing limitations are likely the reason the program continued to crash when simulating one or more of the options below:

- More than one wind rose included
- Adding a roughness layer classifying land types of approximate roughness lengths
- Solving with a higher resolution than 50 m grid points

Regardless of the limitations, Openwind provides valuable insight to the average wind speed distribution in the location of interest, a more comprehensive discussion of the simulation reliability is offered later in section 5.4.

5.2 Weather Data Reliability

5.2.1 Realfagsbygget

The simulations at Realfagsbygget indicate some discrepancies in the wind speed measured. To clarify, the problem does not appear to be related to the anemometer, but rather a result of the potential local turbulence meaning the anemometer appears to be placed within an area affected by turbulence. Hence, the measurements do not represent the general flow behavior above Realfagsbygget at a height corresponding to laminar flow. Turbulence and other local wind conditions can also affect the direction of the wind measured. However, the data seems reasonable regarding whether it represents the overall direction of the wind above Realfagsbygget.

AFD does not provide any tools for inserting length scales, unfortunately. Neither can it be used to measure the wind speed at a specific location, such as the location of the anemometer at Realfagsbygget. However, it is possible to roughly estimate wind speed values to conclude whether the anemometer is affected by turbulence. The estimating procedure is illustrated in figure 5.1 and explained below.

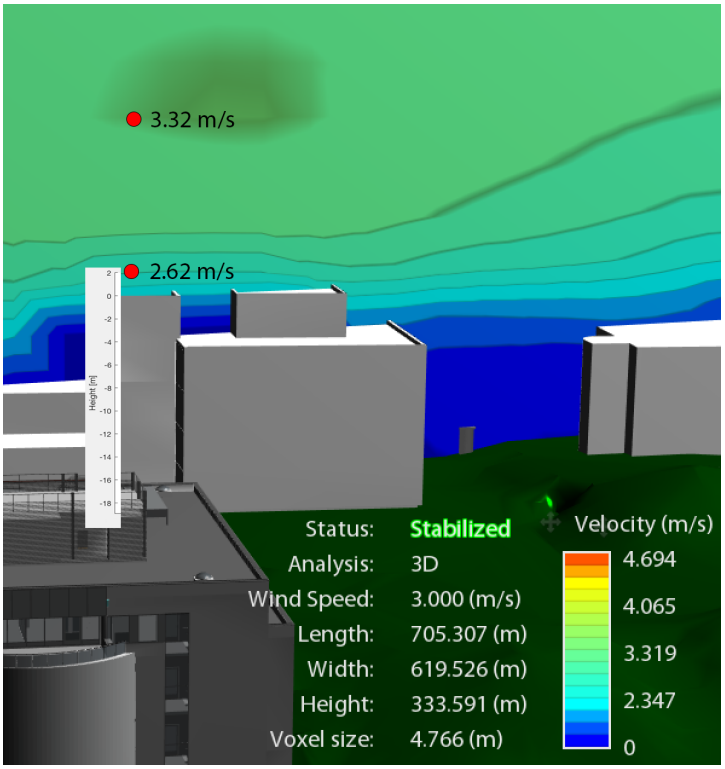

Figure 5.1: Turbulence evaluation at Realfagsbygget

The implemented procedure of estimating the effects of turbulence on the anemometer:

- **Adding length scale**
  The height from the ground to the roof where the anemometer is placed is about 18.9 meters, measured using a tool in Autodesk 3ds Max. Additionally, another anemometer is placed 2 meters above the first one. By orientating a length scale parallel to the 18.9 meter wall, an estimate of the location of the anemometer can be made.

- **Finding the corresponding color band**
  Placing a velocity plane through the location of the anemometer and orienting the viewpoint-angle to be parallel to the roof where the anemometer is placed enables the identification of the corresponding color band. Here the anemometer is located in the boundary between color band 5 and 6.

- **Calculating the wind speed**
  The wind speed is calculated using the equation (3.1).

The wind speed in the location of the anemometer is estimated to be in the transition between the 5^{th} and the 6^{th} color band of about 2.62 m/s, 87 % of the inlet wind speed of 3 m/s. The lower boundary of color band 8 appears in a region from 15 m above the rooftop. In that region, the lower boundary of the simulated wind speed is calculated to be 3.32 m/s, which corresponds to 111 % of the inlet wind speed. A wind speed higher than the inlet wind speed is possible due to local flow consentration. The same relationships were observed when using 6 m/s as inlet wind speed while keeping the other parameters unchanged.

While the estimations are rough, they clearly indicate that the anemometer is located in an area affected by turbulence. The calculations suggest that the actual values of the wind not affected by turbulence or amplification of any kind should be about 15 % higher (comes from 0.87^{-1}) than the values measured.

5.2.2 Grønnåsen

Investigating the locations of the wind sensors mounted in the Avinor mast leads to the conclusion that the measurements are somewhat affected by turbulence. Sensor 2, mounted at 6 m height, is within a birch forest and therefore clearly the wind speed is slowed down . It is likely that the flow measured by that sensor often will be of turbulent nature.

Figure 5.2 might be challenging to interpret at first. It shows the location of the mast, pinpointed by the red circle, and a close-up of a cross-section of it at 21 m height. A wind rose illustrating the wind direction distribution at 21 m height mid-February to mid-May 2017 is added. The ski jumping arena can be seen in the lower part of the figure and appears to be directly upstream of the mast. As the distance from the ski jumping arena to the mast is about 300 m and the 30-meter-tall ski jumping tower is relatively thin, it is most likely not causing wind turbulence 300 m downstream at the Avinor mast, the statement is supported by simulations. However, a slight wind speed decrease at the mast is expected.

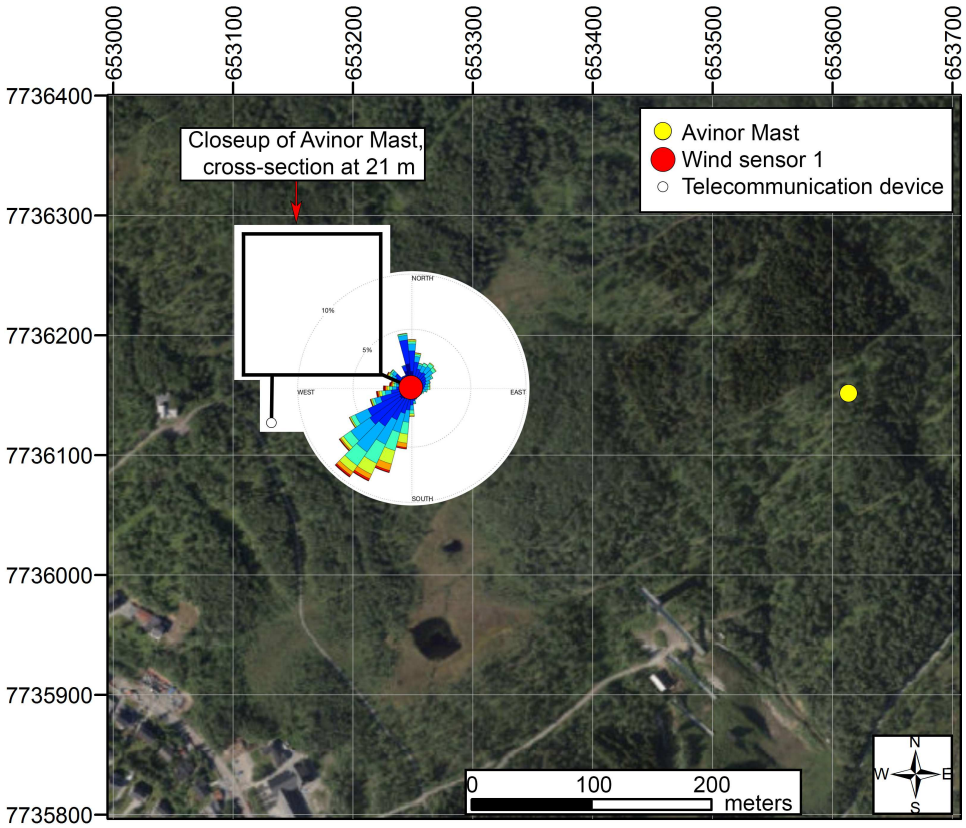

Figure 5.2: Turbulence evaluation at Grønnåsen
Datum: WGS85 Proj.: UTM-33N

For the wind directions inbetween 270° and 0°, the sensors are placed leeward and the measured wind speed will be somewhat reduced due to the framework of the mast itself. In addition, a vertically orientated pole-shaped telecommunication device is mounted at 21 m height, about 1.5 m west-southwest of sensor 1 as illustrated in figure 5.2. It is likely that the device reduces the wind speed measured from directions in the approximate range 240° to 260°. Disregarding the minor issues with the placements of the sensors, it is concluded that the wind measurements provide reliable information regarding wind speed and direction in the area.

5.3 Deciding Parameter Values for Simulation

5.3.1 Inlet Wind Speed

When investigating simulations with a variety of inlet wind speed values it appears that the behavior of the flow is close to independent of the inlet wind speed. Except for the actual values are the patterns almost identical. To validate the results, all the AFD-simulations were used in this study simulated in pairs. One of the simulations in the pair used 3 m/s as the inlet wind speed while the other used 6 m/s, and the other parameters remained unchanged. The value of 3 m/s was chosen as a roundup of the average wind speed in 2015, as Holt had an average wind speed of 2.90 m/s while Realfagsbygget had 2.72 m/s. The inlet wind speed of 6 m/s was chosen as a reference and is closer to the average wind speed weighted by power in the wind.

5.3.2 Inlet Wind Direction

The inlet wind directions used in the simulation were decided by comparing wind roses at Holt and Realfagsbygget to a contour map, see figure 4.8 on page 76.

The wind rose from Holt indicates that the most frequent wind direction accountable for 15 % of the measurements is in the interval [175° - 185°]. Expanding the interval to [165° - 195°] increases the frequency to about 30 %. Holt is located at the west side of Tromsøya and, judging by the terrain highlighted by the contour lines in figure 4.8, it appears that the wind at the surface is deflected slightly towards the west relative to the wind incoming from the south. Note that “deflected towards west” means that the local wind is incoming slightly more from the east, and it is the incoming wind direction that the “inlet wind direction” refers to.

Judging by the wind roses and the topography, it is reasonable to conclude that the wind is most frequently blowing from the inland towards the coast and follows the shape of the fjord. Therefore, for both the Tromsøya 3D-model and the Grønnåsen 3D-model the same three inlet wind directions were simulated for: 180°, 190° and 200°.

The area extent of Campus 3D-model 1 is much smaller than Tromsøya 3D-model and Grønnåsen 3D-model. Here local wind condition is decisive regarding the behavior of the wind, and consequently the inlet directions used in Tromsøya 3D-model and Grønnåsen 3D-model is not necessarily representable. Thus, the measurements obtained from the roof of Realfagsbygget are used to decide the inlet wind direction to be applied for the model.

Figure 4.4 on page 73 shows that the most frequent directions of the wind measured at the roof of Realfagsbygget in 2015 are in the intervals [205° - 215°] and [215° - 225°] with a combined frequency of approximately 20 %. As discussed in section 5.2.1, the data seems reasonable regarding whether it represents the overall wind direction above Realfagsbygget. Consequently, for Campus 3D-model 1 the three inlet wind directions used for simulation are: 205°, 215° and 225°.

5.4 Simulation Reliability

5.4.1 Validity of the 3D-models

The 3D-models used in this study share a few common features. One is that they do not include any vegetation, thus not allowing wind to flow through and be affected by them. For example, a forest that effectively slows down the local wind speed. Another shared property is that the models hold no information regarding surface friction, such as a layer containing the classification of the different land types and corresponding roughness lengths.

The terrain of the Tromsøya 3D-model originates from a 10 m DTM obtained through photogrammetry while the Grønnåsen 3D-model has a more detailed shape – it used a 1 m DTM produced by processing LIDAR data. Unfortunately, the company developing Campus 3D-model 1(Norconsult) could not provide any information on how the model was produced, but the details of the models indicate that it is a TIN and that the terrain originates from a DTM of unknown resolution.

To locate optimal placements for wind turbines the 3D-models are most likely sufficient as they provide a general understanding of the common flow patterns at the location.

5.4.2 Resolution

Simulating fluid behavior is computationally intensive. Therefore, having the appropriate resources is necessary to obtain a satisfactory result in the available timeframe. The simulations presented in this study are simulated on a personal computer with a quad-core processor of 3.2 GHz, SSD harddrive and 24 GB ram. AFD allows for multithreading, enabling all 4 cores to participate in the simulations.

Below is a list of the typical simulation times to reach a “stable state” when simulating in AFD using the computer previously described. When doubling the resolution, the number of grid points in the mesh multiplies by 8 as the flow is solved in three-dimensions ($2^3 = 8$), and the relation is also recognized in the time of simulation completion.

Resulution	Tromsøya 3D-m.	Grønnåsen 3D-m.	Campus 3D-m. 1
100 %	3 hrs	2 hrs	1.5 hrs
200 %	1 day	16 hrs	9 hrs
400 %	8 days	6 days	3 days

Table 5.1: Typical simulation time to reach "stable state"

A general rule is that the resolution is sufficient when the result of the simulation does not change any more than the desired accuracy when increasing the resolution. For all three models, notable changes were seen in the results when increasing the resolution from 100 % to 200 %. The observed variations were somewhat clearer in results obtained simulating with Tromsøya 3D-model compared to Campus 3D-model 1. When further increasing the resolution to 400 % no changes were seen in the Campus results and noticeable, but insignificant, variations were detected in both the Tromsøya and the Grønnåsen results. Consequently, a resolution of 200 % is used for all the simulations presented in this study.

5.4.3 Simulated Results

AFD and Openwind have clear limitations, listed in section 5.1.2, effectively questioning the validity of the simulations. Having no possibility for an inlet vertical wind profile is perhaps the greatest limitation in AFD. Unlike AFD, Openwind is able to estimate the wind speed dependency on elevation. Regardless of the differences in the functioning of the two simulation tools, they are both suggesting the same area at Grønnåsen to be the most effective placement for a wind turbine. Together, AFD and Openwind provide a strengthened understanding of the wind behavior in the area while supporting the validation of the simulations.

Openwind estimates an annual average wind speed in the interval of 6.6 to 6.9 m/s at 20 m AGL at the suggested optimal location for a wind turbine at Grønnåsen. It is likely that the true average at that elevation is notably lower due to effects of the local birch forest not accounted for in the simulations, a prediction of how much lower might be attained when wind measurements at Grønnåsen are gathered.

The simulations using Tromsøya 3D-model have a voxel size of about 75 m, which cannot be considered sufficient when pinpointing an optimal placement for a wind turbine. Therefore, these simulations are only used to locate areas of interest for further investigation.

Regarding wind at the campus, only the simulations using Campus 3D-model 1 are presented in the result chapter. In this model only one building, Fredsbygget, is included upstream of Realfagsbygget. In reality there are many more buildings upstream potentially causing turbulence all the way downstream to Realfagsbygget. To investigate the reliability of the laminar inlet wind, simulations on the bigger model, Campus 3D-model 2, were conducted. The simulations indicated that the flow is laminar when reaching Fredsbygget and therefore the inlet wind behavior at the boundary of Campus 3D-model 1 is considered to be satisfactory.

5.5 Optimal Placement of Wind Turbines

5.5.1 Realfagsbygget

As a MWT should be placed in an area of frequently high wind speed, the area of intersection in figure 4.17 on page 87 is a natural first candidate. However, it is not certain that the optimal placement of the MWT is within this area as the flow could be disturbed by turbulence. Other visualization methods need to be utilized to identify potentially turbulent behavior and ultimately find the most feasible placement regarding maximizing electric power production.

By further investigating the nature of the flow using flow lines, it is clear that the fluid seems to be laminar in the area of intersection in figure 4.17. It is not as easy to see the behavior clearly in still pictures in comparison to moving flow lines in an interactive program, but some of the most important features are presented and characterized in figure 4.19 and 4.20 on page 89.

In figure 4.19 on page 89 the wind comes from 215° with a wind speed of 3 m/s. Minor differences in the behavior of the flow were spotted when simulating wind coming from 205° and 225° and no significant differences were found when increasing the wind speed from 3 m/s to 6 m/s. In all the simulations did the flow seem to be perfectly laminar in the area in question.

Figure 5.3 shows a proposed optimal placement of the MWT and an alternative. The proposed one is in the center of an area where the wind speed is simulated to be at its most intensified over Realfagsbygget. The speed is intensified as the cross-section of the fluid flow is decreased when reaching the front walls of Realfagsbygget. The alternative placement is pointed out in case the optimal one is not practical based on the placement of the pre-existing weather station.

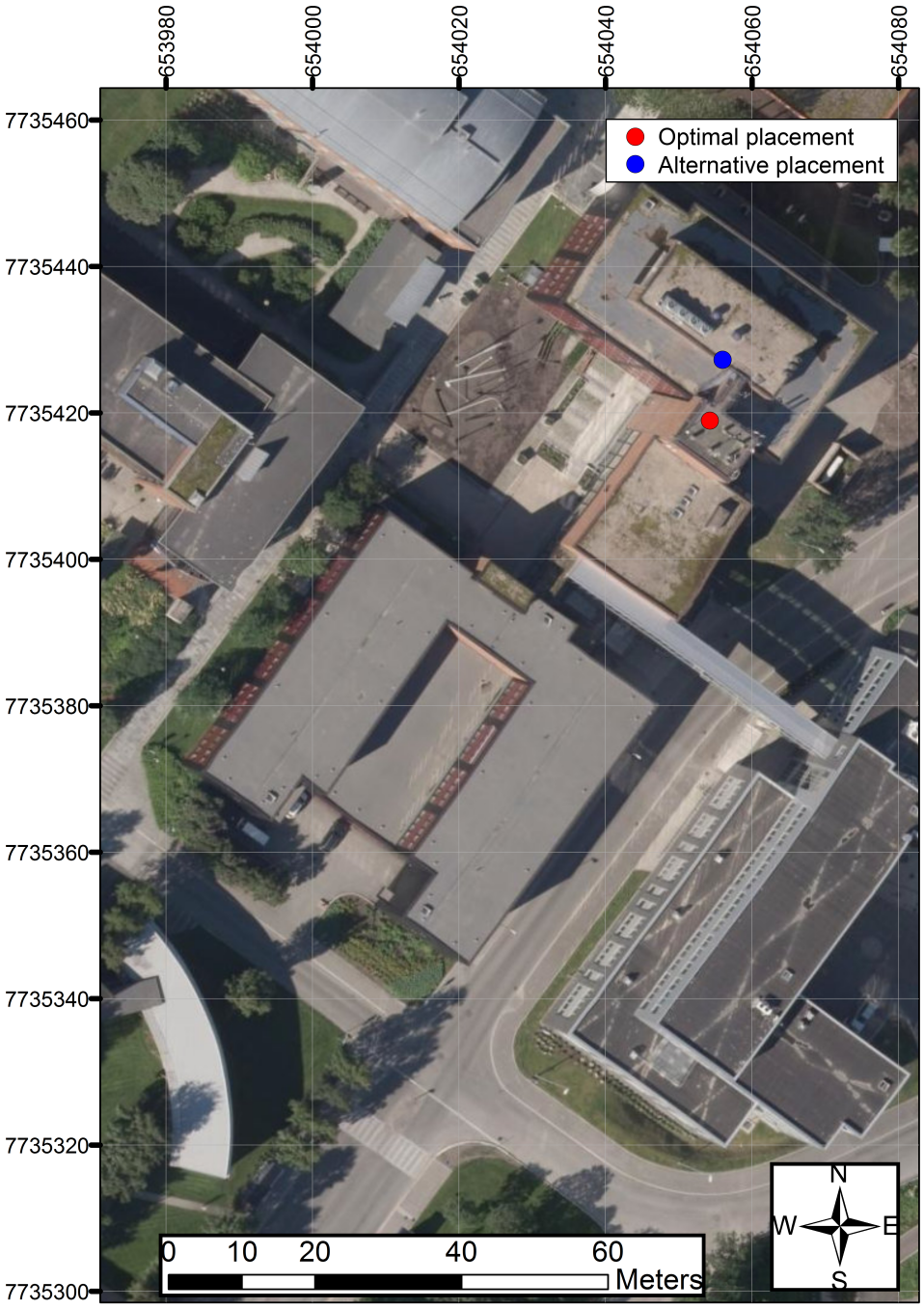

Figure 5.3: Optimal placement of MWT at Realfagsbygget
Datum: WGS85 Proj.: UTM-33N

The blades of the MWT should be placed to operate in a region within 10 to 17 m above the roof. If the optimal height is impractical, the blades can be lowered a couple of meters since the simulations suggest there is little or no turbulence at those heights at the same location.

When comparing the result to other similar studies, a couple of similarities and differences are worth mentioning. First, a study published in 2013, in a renewable energy journal, claims that in an urban environment the maximum turbulence intensity extends from the surface of the roof to a height of about 1.3 times the height of the building (Abohela 2013, 1117). The statement suggests that the lower part of the operating region of the MWT at Realfagsbygget should be at least at a height of 5.7 m as the roof is about 18.9 m above ground. The suggested operating region of the MWT is from 10 meters, well above the height of maximum turbulence according to the claims in the journal article.

Secondly, in a study of MWT performance in urban environments, published in 2013 by an international journal of energy and environmental engineering, yet another general guideline was proposed: “The mast of the turbine should be approximately 50 % taller than the surrounding objects” (Gagliano 2013, 1). As the study refers to horizontal axis wind turbines it simply generalizes that the height of the center of the operating region should be approximately 50 % taller than the surrounding objects. Here the surrounding objects are at 18.9 meters meaning that the center of the operating region should be at about 9.5 meters above the roof. This is somewhat lower than the proposed placement depending on the size of the blades and could be explained by local conditions.

5.5.2 Grønnåsen

When deciding the placement of a wind turbine in the region of Grønnåsen the results obtained from AFD are compared to the Openwind simulations. The comparison is illustrated in figure 4.27 on page 95. Both methods indicate approximately the same optimal placement which validates the results.

Figure 5.4 presents the proposed optimal placement of a wind turbine at Grønnåsen. The red elliptical shape outlines the region the turbine should be placed if the suggested optimal placement is impractical.

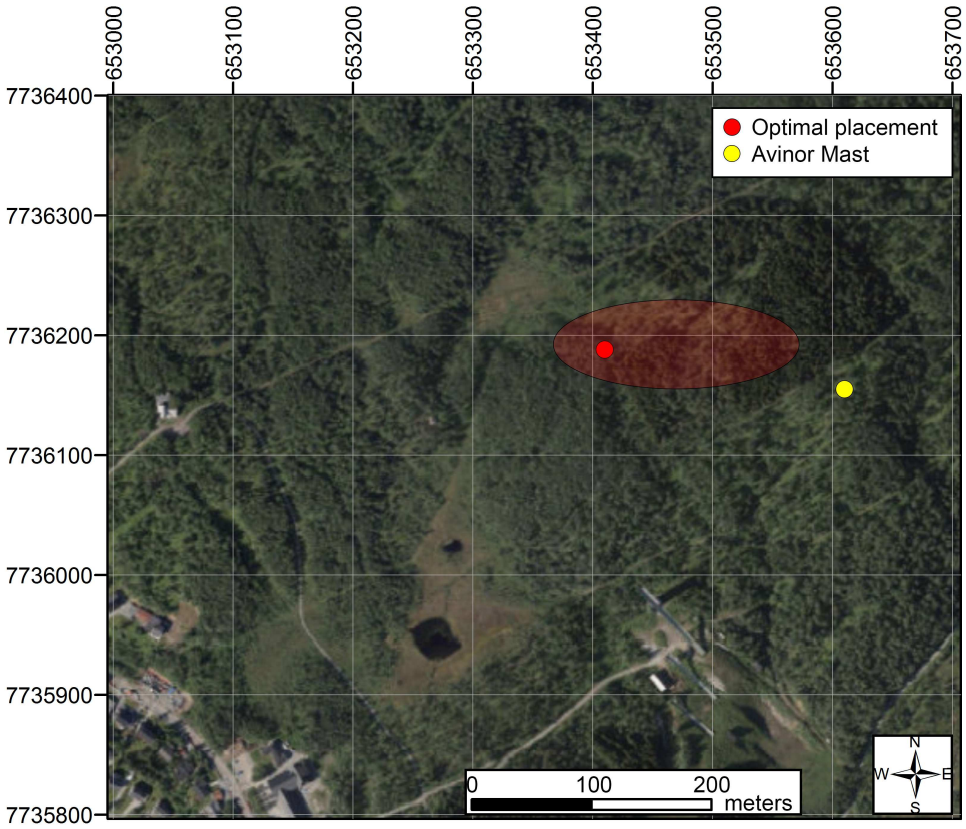

Figure 5.4: Optimal placement of wind turbine at Grønnåsen
Datum: WGS85 Proj.: UTM-33N

Neither of the models include the 30-meter-tall tower of the ski jumping arena, seen in the lower part of figure 5.4. It is likely that the tower affects the flow downstream of it, an effect not accounted for in the simulations. Fortunately, for the most frequent directions of the wind (blowing from south-west) the red ellipsoid is not directly downstream of the tower (see figure 5.2 on page 102) and it is concluded that the suggested optimal area can be retained.

Regarding determining the operating height of the turbine, it is important to acknowledge the limitations of the 3D-model. The Grønnåsen 3D-model does not include vegetation; hence, any turbulence caused by the birch forest at Grønnåsen is not seen in the simulations. To minimize the potential power reducing effect the blades of the turbine should be placed such that they reach a minimum of 7-8 m above the nearby trees. As the wind speed increases with height so will the power produced if further elevated.

5.6 Wind Power Density Estimations

To evaluate the power production potential at the suggested placements of a wind turbine the energy in the wind at the locations in question has been studied. Rough estimates of wind power density in 2015 for the predicted optimal location at Realfagsbygget and Grønnåsen are presented in figure 5.5 below. The dotted lines are only included to illustrate the estimation procedure and the wind speed sampling rate sensitivity. The estimation process and the related uncertainties are explained in the next pages.

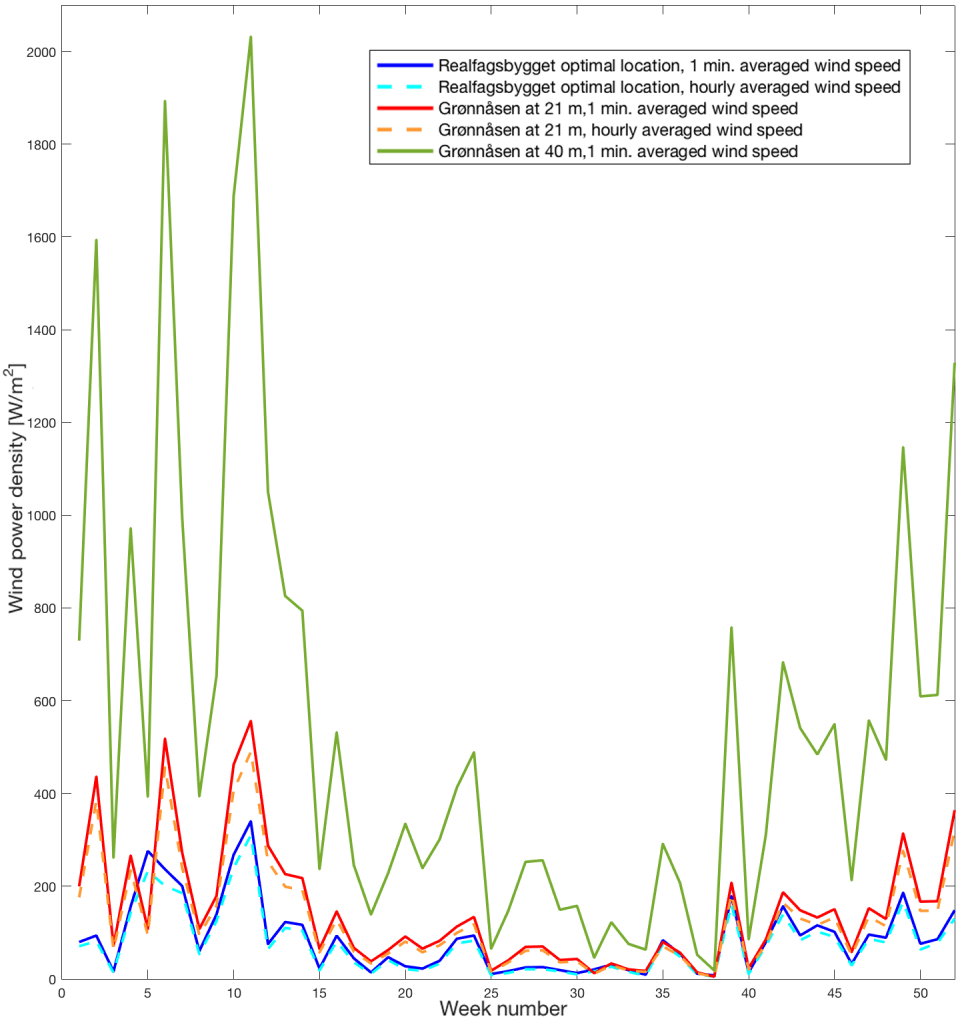

Figure 5.5: Wind power density estimations, weekly averaged values from 2015

The process of estimating wind power density is as follows for the listed locations:

- **Realfagsbygget optimal location, wind speed averaged over one minute**
  AFD simulations indicate that the wind speed at the predicted optimal location for a MWT, 10 to 17 m above the roof of Realfagsbygget, is about 27 % $\left(\frac{3.32\ m/s}{2.62\ m/s} \approx 1.27\right)$ faster than at the anemometer placement (see section 5.2.1) for the most frequently measured directions of the wind which also correspond to most of the energy.

  When estimating the wind power density in the optimal location the wind speed measurements from Realfagsbygget is therefore multiplied by 1.27 before calculating the power density. Here an annual power density average of 2015 was estimated to be 86 W/m^2. The weekly averaged wind power density estimation for the optimal location at Realfagsbygget in 2015 is illustrated by the blue solid line in figure 5.5.

- **Grønnsen at 21 m AGL, hourly averaged wind speed**
  Both AFD and Openwind simulations indicate that the wind speed at the predicted optimal placement at Grønnåsen is similar to the wind speed at the Avinor mast 300 m to the east. Therefore, the measurements from the Avinor mast are used as a basis to estimate the wind power density at the optimal location. Unfortunately, wind data from a complete year has not yet been sampled, as of June 2017. Therefore, the obtained data from mid-February to mid-May 2017 are compared to weather data from Holt, see table 4.1 on page 79. The Pearson correlation coefficient between wind speed measurements at Grønnåsen at 21 m AGL and Holt at 2 m AGL is 0.73 when hourly averaged and 0.87 when averaged by the day. It is not optimal for accurate wind speed predictions at Grønnåsen based on Holt data, but it is the best available option.

  In the period mid-February to mid-May 2017 the average wind speed in the mast at 21 m AGL was 4.22 m/s compared to 2.91 m/s at 2 m AGL at Holt. Therefore, when using 2015 Holt data the wind speed was multiplied by 1.45 $\left(\frac{4.22\ m/s}{2.91\ m/s} \approx 1.45\right)$ to simulate Grønnåsen weather data before calculating the power density. The weekly averaged wind power density estimation for Grønnåsen at 21 m AGL in 2015 is illustrated by the orange dotted line. A dotted line is used to highlight that the wind speed data used in the calculation are hourly averaged and thus likely underestimations.

- **Realfagsbygget optimal location, hourly averaged wind speed**
  To compare the estimated wind power density at Realfagsbygget and Holt the wind speed data should be averaged over the same length of time, preferably the shortest achievable time step to maximize accuracy. A way to study the sensitivity of the time averaged over is to average the data from Realfagsbygget into hourly averaged data and then calculate the wind power density. When doing so the annual average power density was reduced by 13.6 % compared to the estimation based on data averaged over one minute. The weekly averaged wind power density at Realfagsbygget 2015, calculated using hourly averaged wind speed data, is plotted in a light blue dotted line.

- **Grønnsen at 21 m AGL as if based on data averaged over one minute**
  Increasing the estimated wind power density based on hourly averaged data by 13.6 % simulates approximate values as if the data was averaged over one minute instead, a weekly average of it is marked by the red solid line. The annual power density average of 2015 was estimated to be 146 W/m^2 at Grønnåsen at 21 m AGL.

  It is important to emphasize that observed relation only describes the minute to hourly averaged wind speed sensibility for the data set at Realfagsbygget. The relation would be different for other types of locations as the magnitude and frequency of the fluctuations in wind speed varies. The weather stations at Realfagsbygget and Holt differs in type of location as the wind sensor at Holt is placed in the middle of an agricultural field while the anemometer at Realfagsbygget is placed on the roof of a building at a university campus. Nevertheless, the relation of a 13.6 % reduction in the calculated annual average power density based on hourly averaged wind speed compared to average by the minute at Realfagsbygget is considered satisfactory for providing a rough estimate for Grønnåsen.

- **Grønnsen at 40 m AGL**
  The predicted vertical wind profile at Grønnåsen (see section 4.1.4 on page 79) suggest that the average wind speed in the measured period is 6.5 m/s at 40 m height. An annual wind speed average of 6.5 m/s is considered by the Norwegian Ministry of Petroleum and Energy to be the lower limit to produce commercially viable wind power (Norwegian Ministry of Petroleum and Energy 2015, 28). The power density in the wind at the previously described locations should therefore be compared to the density corresponding to the average wind speed of 6.5 m/s.

To estimate the wind power density at 40 m AGL at Grønnåsen the measured wind speed at 21 m AGL was multiplied by 1.54 $\left(\frac{6.5\ m/s}{4.22\ m/s} \approx 1.54\right)$ before calculating the power density. The weekly averaged wind power density estimation for Grønnåsen at 40 m AGL in 2015 is illustrated by the green solid line and the average of the year was 535 W/m^2.

As described above is it clear that the estimations presented in figure 5.5 are rough and have many uncertainties associated to them. Therefore, the estimations cannot be used to accurately represent the wind power densities at the locations. The figure is only intended to provide a better understanding of the likely energy potential differences at the two locations and to compare them to an energy density considered to be commercially viable regarding wind power electricity production.

6

Conclusion

6.1 Summary

Weather data
The wind above Tromsøya and the surrounding region most frequently follows the topography of the fjord and blows from the inland northward towards the coast.

- Holt and Realfagsbygget
In 2015, the annual average wind speed at the Holt weather station (2 m AGL) was 2.90 m/s, a bit higher than at Realfagsbygget (2 m above the roof) which had an average wind speed of 2.73 m/s. Simulations indicate that the anemometer at Realfagsbygget is placed within an area of turbulence, which can explain the measured wind speed reduction at Realfagsbygget relative to Holt. Concerning wind directions, at Holt the prevailing winds originate from the south, while at Realfagsbygget the wind mostly comes from the southwest. The deviation is caused by the topography and local conditions.

- Grønnåsen
Weather data at Grønnåsen has only been sampled since mid-February 2017. In the periodfrom mid-February to mid-May 2017, the measured average wind speed was 4.22 m/s at 21 m AGL, 1.45 times the average at Holt at 2 m AGL in the same period. The most frequent incoming direction in the period was southwest, similar to Realfagsbygget. By using the hourly averaged wind speed data, a Pearson correlation coefficient of 0.73 between the data sets from Grønnåsen

(at 21 m AGL) and Holt (at 2 m AGL) was calculated. Increasing the time interval to daily averages further amplified the coefficient to 0.87. However, due to the placement of the sensors in the mast, the wind incoming from the interval [240° (west-southwest) - 0° (north)] might be affected by the mast itself, potentially reducing wind speed and changing the direction measured. Despite the sensor placements, it is concluded that the wind measurements provide reliable information regarding wind speed and direction in the area.

Developing 3D-models
Most of the data manipulation to obtain the 3D-models used in this study was conducted in Autodesk Infraworks 360. Infraworks combines multiple layers of information and produces a TIN model, which is a 3D-model consisting of a triangle mesh. To attempt increasing the level of detail in the models, the utilization of LIDAR data was proposed. The data was successfully processed in Quick Terrain Modeler and high-detailed DSMs were produced. Unfortunately, dealing with those quantities of data proved to be too computationally intensive as Infraworks kept crashing while handling the high-detail DSMs. Consequently, none of the 3D-models used in this study include any vegetation and hold no information regarding surface friction.

Wind simulations
The main application used for wind simulation in this study is Autodesk Flow Design. AFD uses the Finite Volume Method to discretize the fluid equations and the Large Eddy Simulation as a turbulence model (Autodesk 2014, 2). A clear weakness of the simulation tool is that it does not allow for a gradient inlet wind profile, questioning the validity of the simulations. To compliment the results obtained from AFD, the GIS-based software Openwind is used. Unlike AFD, Openwind is able to estimate the wind speed dependency on elevation. Together the two simulation tools provide a strengthened understanding of the wind behavior while supporting the validation of the simulations.

The resolution used in the AFD simulations presented was set to 200 % as no noteworthy changes were seen when further increasing the resolution to 400 %. Simulations indicated that there are little or no variations of significance in the location of the areas of highest wind speed between simulating different realistic values for inlet wind speed. Other important simulation results are presented in the following section.

6.2 Concluding Remarks

The suggested optimal location of a MWT at the roof of Realfagsbygget is at B-wing with the UTM-33N coordinates: (654053 – 7735418). An alternative placement is proposed in case the optimal one is not practical regarding the placement of the pre-existing weather station and has the UTM-33N coordinates: (654055 – 7735427). Simulations imply that the wind speed is at its most intensified in the region 10 to 17 m above the roof and that the flow is laminar there. Therefore, for both of the suggested locations the blades of the MWT should be placed to operate in a region within 10 to 17 m above the roof. If the optimal height is impractical, the blades can be lowered a couple of meters as the simulations suggest there is little or no turbulence at those heights above the roof.

At Grønnåsen, the predicted optimal wind turbine location has the UTM-33N coordinates: (653410 - 7736185). The placement was decided based on a comparison of AFD and Openwind simulations in which both methods indicated approximately the same location. To minimize the potential power reducing effect of turbulence the blades of the turbine should be placed such that they reach a minimum of 5 m above the nearby trees. As the wind speed increases with height so will the power produced if further elevated.

The average power density and wind speed at 21 m AGL in the Avinor mast at Grønnsen was calculated to be 135.4 W/m^2 and 4.22 m/s in the period from mid-February to mid-May 2017. Rough estimations suggest that the annual power density at the suggested optimal location of a wind turbine at Grønnåsen is 146 W/m^2 at 21 m AGL and 535 W/m^2 at 40 m AGL. The estimated annual power density at the suggested location of a MWT at the roof of Realfagsbygget is in comparison merely 86 W/m^2. It is important to emphasize that these estimations are rough and have many uncertainties associated to them. Therefore, the estimations cannot be used to accurately represent the wind power densities at the locations. A complete annual time series of wind measurements at Grønnåsen is favorable to improve the reliability of the estimations.

6.3 Future Work

There are numerous possible extensions for improving the accuracy of the simulations and to facilitate the installation of a wind turbine in the proposed locations. Some of these are:

- **Strive to utilize the full potential of the LIDAR data**
  Process the data in such a way that a highly detailed DSM of reasonably low file size can be produced and used to create a 3D-model. Also, the classification of the data enables information about roughness lengths of different land types to be added and used by, for example, Openwind Enterprise.

- **Upgrade to Openwind Enterprise**
  Openwind Basic is quite limited compared to the possibilities within the Enterprise version. The GIS-based software can be used to include a roughness layer, as well as multiple wind roses while increasing the resolution of the simulations significantly. It can also be used to estimate power production and holds power curves of multiple modern wind turbines on the market.

- **Enable the usage of Autodesk CFD**
  The complexity and file size of the models produced in this study were too big for Autodesk CFD to be able to create a simulation mesh. Reducing the file size of the models, while maintaining the necessary detail, may permit the usage of Autodesk CFD. Autodesk CFD offers various options for defining the boundary conditions, such as allowing for a vertical wind profile inlet, and also changing the turbulence model used. Effectively, the enhanced options increase the validity of the simulations.

- **Conduct a risk analysis**
  Evaluating potential risks related to icing, fire, aviation, bird life, noise and public accessibility.

- **Other possibilities**

  - Simulate the possibility of deforestation to alter the flow and enhance the power production

  - Estimate power production

  - Plan the foundation of the wind turbine and the cable path

- Studs options to interconnect the turbine and other components in the hybrid system

- Conduct a complete economic analysis

Appendices

A

Importing Data from Sensors at Grønnåsen

This quick guide aims to help UiT staff and students to gather and prepare the weather data at Grønnåsen for storage and analyzation. The commands provided in this guide only work on a Unix-based computer. However, the same approach can also be used when preparing the data on a Windows-based computer. The DOS commands will be different, but are easily found through a quick search on the web.

1. **Get access to data logger**
   The suitcase containing the data logger is secured with a combination code lock and the surrounding enclosure is also locked. A key and the combination code will be provided by the author of this thesis upon request.

2. **Ensure a continuous time series of data**
   The logger is programmed to save 60-second-averages and the data is transferred to the SD memory card each minute, indicated by a red light blinking. The memory card should not be removed while transferring data, so please remove it a couple of seconds after the red light has blinked, just to be sure. An empty SD memory card should be inserted back into the slot within one minute.

3. **Merge the files**
   Each TXT-file holds the data of one day. To simplify the process of importing the data to any computer tool analyzing it, the files can be merged. Make sure all the TXT-files you want to merge are located in the same folder and that their original file names are unchanged. In a Unix-based computer: open the Terminal and find the directory of the folder holding the TXT-files. Then type:
   `cat *.TXT > output.txt`
   It will make a single file, "output.txt", containing all the TXT-files added together in a chronological order.

4. **Prepare the file to be imported by Matlab or Python**
   Some computer tools, including Matlab and Python, have issues reading the txt-file produced at the previous step and will divide one row of data into two rows. In a Unix-based computer it can easily be dealt with in the Terminal by entering the folder holding the txt-file and typing:
   `sed -e "s/\^M//" output.txt > outputnew.txt`
   It will create a new file, "outputnew.txt", where "`^M`", responsible for the misreading, is replaced with a space bar. NB! When typing "`^M`" do not use the hat on your keyboard, but instead type "`control-v + M`".

The logger can be reprogrammed by placing a TXT-file named "SETUP.TXT" in the root folder of the memory card to be inserted. The currently used setup is presented below and additional commands can be found in the user manual at: `http://www.meacon.co.za/RPR%20Loggers/PDFs/S10%20User%20Manual.pdf`.

SETUP.TXT

```
WAIT
DATE=DD/MM/YY    // set date
TIME=hh:mm:ss    // set time
RATE=60          // store a 60-second-average
BAUD=4800        // set baud rate
RX2=Y            // monitor sensor 2
SENTENCE2=Y      // if data from sensor 1 is detected
                 // - expect data from sensor 2
LOGETX=N         // do not record End-of-Text character
SEPARATOR=Y      // add a comma after the first data sample
NEWLINE=N        // no new line is added after the data from sensor 1
                 // so that data from sensor 2 appear at the same line
FILE=20.txt      // store data in a txt-file
```

B

Additional Plots of Weather Data

B.1 Holt

Seasonal Wind Roses

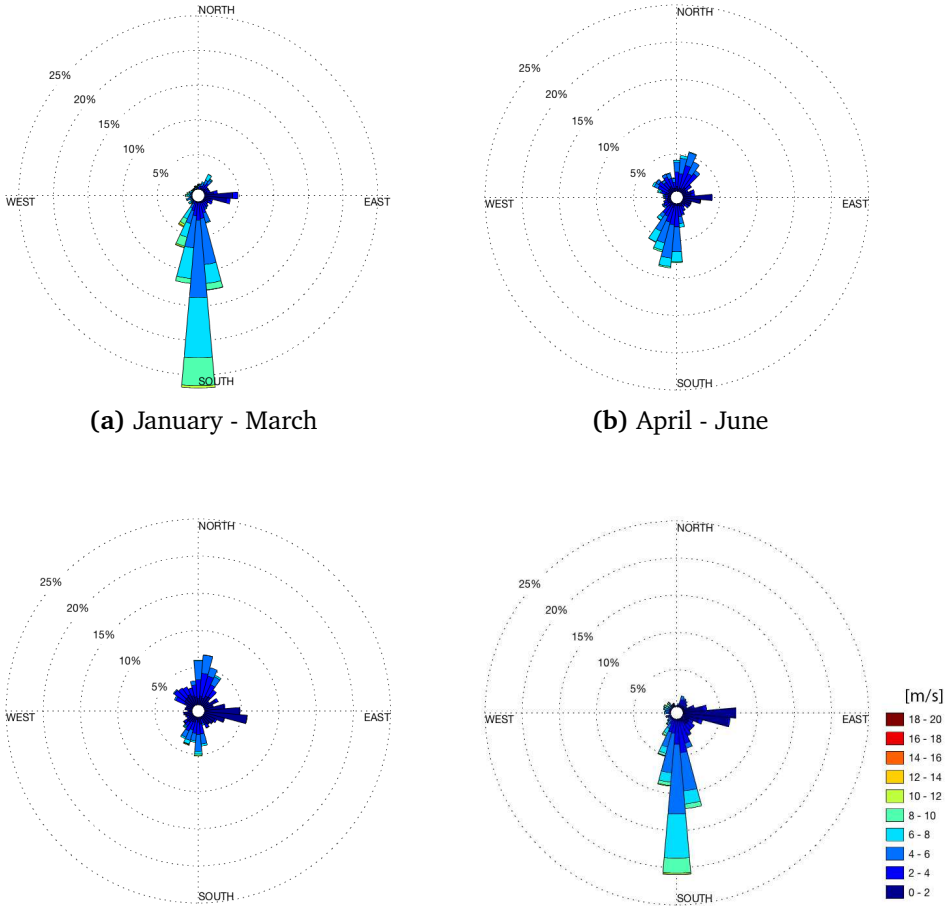

(a) January - March

(b) April - June

(c) July - September

(d) October - December

Figure B.1: Seasonal wind roses from Holt, 2015
(the scale in the lower right corner belongs to all the figures)

B.2 Realfagsbygget

Seasonal Wind Roses

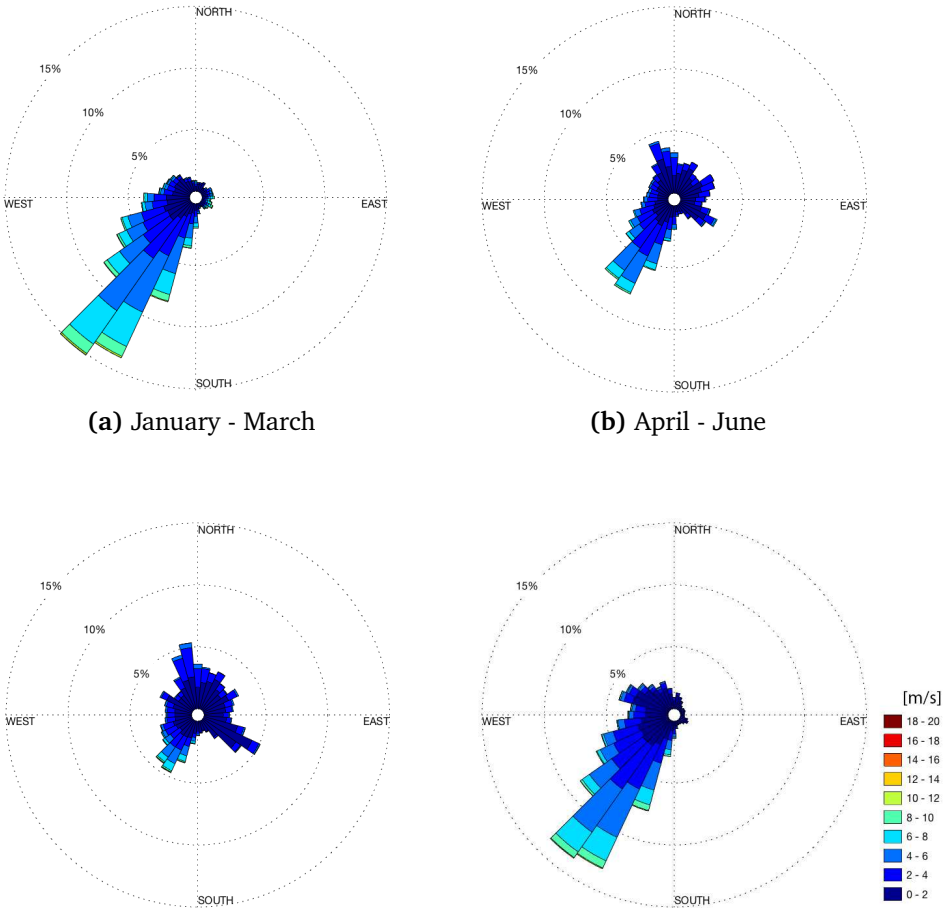

(a) January - March

(b) April - June

(c) July - September

(d) October - December

Figure B.2: Seasonal wind roses from Realfagsbygget, 2015
(the scale in the lower right corner belongs to all the figures)

/C

Openwind - Additional Simulations

C.1 Wind speed distributions from different directions

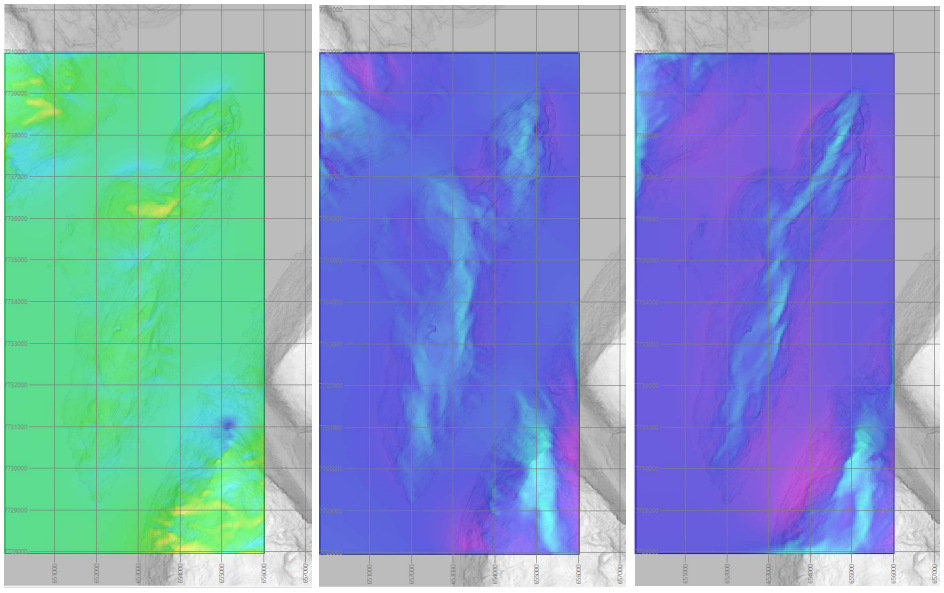

(a) 0° **(b)** 60° **(c)** 120°

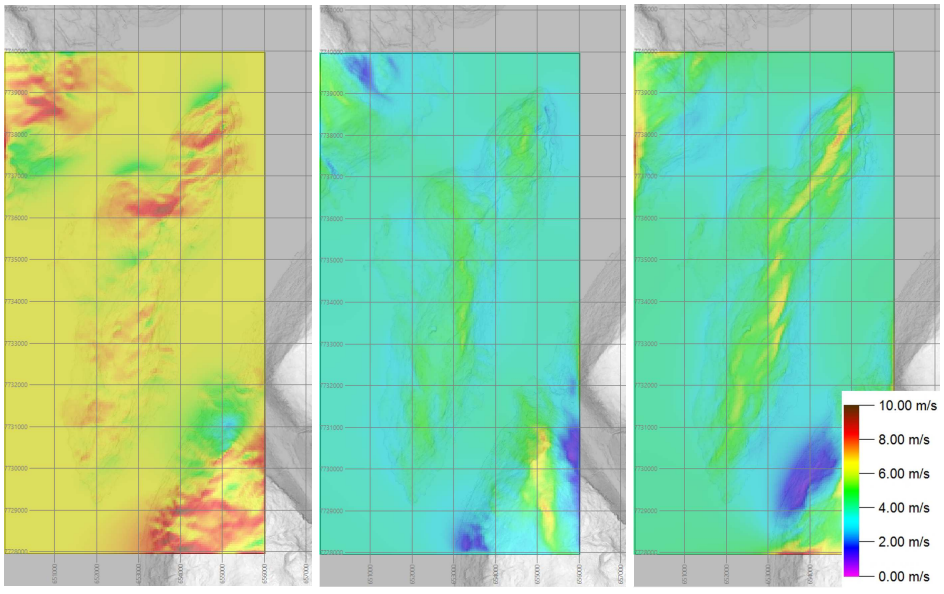

(d) 180° **(e)** 240° **(f)** 300°

Figure C.1: Estimated annual distribution of wind speed averages from different directions, at 20 m AGL. Datum: WGS85 Proj.:UTM-33N (the scale in the lower right corner belongs to all the figures)

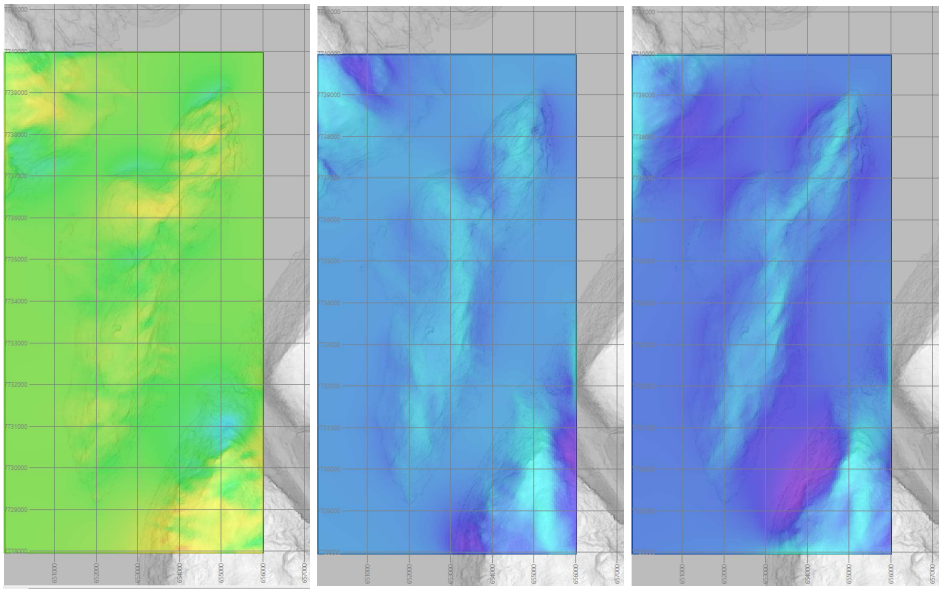

(a) 0° **(b)** 60° **(c)** 120°

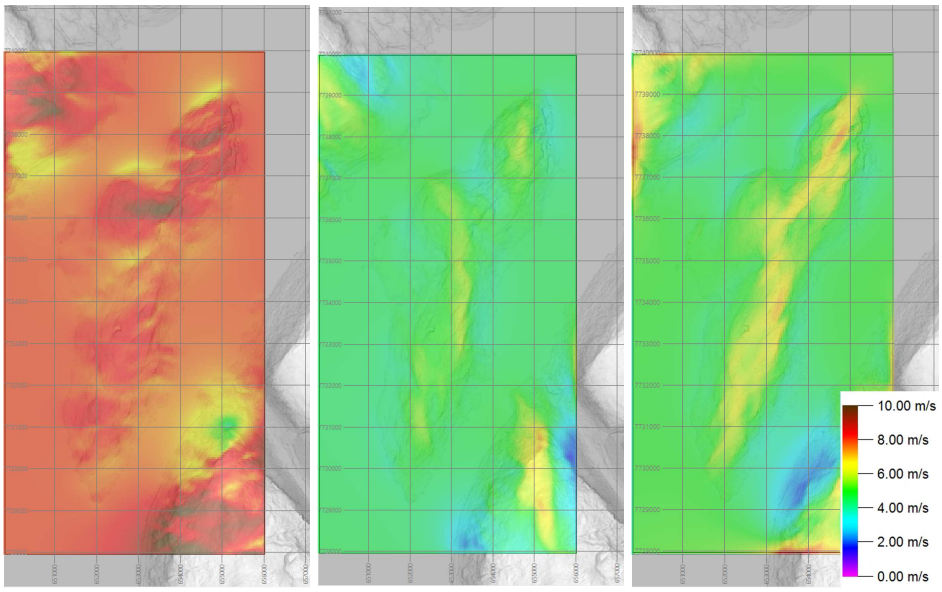

(d) 180° **(e)** 240° **(f)** 300°

Figure C.2: Estimated annual distribution of wind speed averages from different directions, at 50 m AGL. Datum: WGS85 Proj.:UTM-33N (the scale in the lower right corner belongs to all the figures)

D

Sources of Data

D.1 Public

- **Weather data**
  - Bioforsk weather station
    Data from Holt downloaded at Bioforsk's datebase, `http://lmt.bioforsk.no/agrometbase/getweatherdata_new.php`.
- **3D-models**
  - Tromsøya 3D-model
    Multiple DEMs from Kartverket at `http://data.kartverket.no/download`. Information about roads and buildings gathered at OpenStreetMap, `www.openstreetmaps.org`, and is made available under the Open Database License at `https://opendatacommons.org/licenses/odbl/1-0`. The imagery layer origins from Microsoft's Bing Maps, `https://www.bing.com/maps/`.
  - Grønnåsen area 3D-model
    Roads, buildings and imagery has same source as Tromsøya 3D-model above.

- **Maps**

  Quite a few maps, both DEMs and background maps, are presented in the thesis which origins from the same few common sources:

  - 30 m DEM from Kartverket at `http://data.kartverket.no/download`. Used in the figures:2.17, 4.8 and as the DTM used in Openwind as seen in 3.25.

  - "Light Gray Canvas", owned by Esri and gathered trough ArcGIS' Web Map Service (WMS). Used in the figures: 3.1, 3.8a, 3.13a and 4.8.

  - "GeocacheBilder 32633", produced by Geodata AS and gathered trough ArcGIS' WMS. Used in figures: 3.2a, 3.3a, 3.6, 5.3 and 5.4.

D.2 Non-public

- **Weather data**

  - Realfagsbygget weather station
    Data provided by Jon Ivar Kristiansen, a senior engineer at the "Department of Computer Science" at UiT.

- **3D-models**

  - Campus 3D-models
    Statsbygg owns the rights to both models and approved the usage of them in this study. Norconsult section Arkitektstudio created Campus 3D-model 1 and Rambøll further developed it to become Campus 3D-model 2.

  - Grønnåsen area 3D-model
    LIDAR data given access to by Tromsø municipality administration and is owned by Statens Kartverk. The 1 m LIDAR DTM is owned by Geodata AS.

Bibliography

Abohela, I., N. Hamza, and S. Dudec. 2013. *"Effect of roof shape, wind direction, building height and urban configuration on the energy yield and positioning of roof mounted wind turbines."* In *Renewable Energy 50*, 1106 -1118. Amsterdam: Elsevier. doi:10.1016/j.renene.2012.08.068

Andrews, John, and Nick Jelly. 2007. *"Energy Science – principles, technologies, and impacts."* New York: Oxford University Press. ISBN: 978-0-19-928112-1

ASTER. 2017. *"ASTER Global Digital Elevation Map Announcement."* Accessed February, 2017. `https://asterweb.jpl.nasa.gov/gdem.asp`

Autodesk. 2014. *"Flow Design Preliminary Validation Brief."* Accessed April, 2016. `http://www.autodesk.com/us/flow_design/Flow_Design_Preliminary_Validation_Brief_01072014.pdf`

AWS Truepower. 2017. *"Basic Edition - Features."* Accessed May, 2017. `http://software.awstruepower.com/openwind/editions/basic`

AWS Truepower. 2010. *"Theoretical Basis and Validation."* Accessed May, 2017. `http://www.autodesk.com/us/flow_design/Flow_Design_Preliminary_Validation_Brief_01072014.pdf`

AWS Truepower. 2014. *"User Manual."* Accessed May, 2017. `http://software.awstruepower.com/openwind/wp-content/uploads/sites/2/2014/12/Openwind_user_manual_1-6.pdf`

CFD Online. 2017. *"Direct Numerical Simulation (DNS)."* Accessed April, 2017. `https://www.cfd-online.com/Wiki/Direct_numerical_simulation_(DNS)`

Defra. 2011. *"Department for Environment Food and Rural Affairs – Digital terrain model."* Accessed February, 2017. `http://adlib.everysite.co.uk/adlib/defra/content.aspx?id=2RRVTHNXTS.96RYU2KJZWFLU`

ESA (European Space Agency). 2004. *"Space in Images."* Accessed April, 2017. http://www.esa.int/spaceinimages/Images/2005/06/Earth_s_wind_patterns

Eymard, Robert, Thierry Gallouet, and Raphaele Herbin. 2003. *"Finite Volume Methods."* https://www.cmi.univ-mrs.fr/~herbin/PUBLI/bookevol.pdf

Floriani, Leila De, and Paola Magillo. 2009. *"Triangulated Irregular Network."* In *Encyclopedia of Database Systems*, edited by Ling Liu and M. Tamer Zsu, 2907-3220. Boston: Springer US. ISBN: 978-0-387-39940-9. doi: 10.1007/978-0-387-39940-9_437.

Gagliano, Antonio, Francesco Nocera, Francesco Patania, and Alfonso Capizzi. 2013. *"Assessment of micro-wind turbines performance in the urban environments: an aided methodology through geographical information systems."* In *International Journal of Energy and Environmental Engineering*, 4:43. Berlin: Springer. ISSN: 2251-6832. doi:10.1186/2251-6832-4-43. http://dx.doi.org/10.1186/2251-6832-4-43

GISGeography. 2017. *"How Universal Transverse Mercator (UTM) Works."* Accessed February, 2017. http://gisgeography.com/utm-universal-transverse-mercator-projection

IPCC, 2007. *" Climate Change 2007: Mitigation."* Contribution of Working Group III to the Fourth Assessment Report of the Inter- governmental Panel on Climate Change. B. Metz, O.R. Davidson, P.R. Bosch, R. Dave, L.A. Meyer (eds). Cambridge and New York: Cambridge University Press. https://www.ipcc.ch/pdf/assessment-report/ar4/wg3/ar4_wg3_full_report.pdf

Kaltschmitt, Martin, Wolfgang Streicher, and Andreas Wiese. 2007. *"Renewable Energy – Technology, Economics and Environment."* Berlin: Springer. ISBN: 978-3-540-70947-3. doi: 10.1007/3-540-70949-5. http://link.springer.com/book/10.1007%2F3-540-70949-5

Ledo, L., P.B Kosasih, and P. Cooper. 2011. *"Roof mounting site analysis for micro-wind turbines."* In *Renewable Energy 36*, 1379-1391. Amsterdam: Elsevier. doi:10.1016/j.renene.2010.10.030

Li, Zhilin., Qing Zhu, and Christopher Gold. 2005. *Digital Terrain Modeling - Principles and Methodology.* Florida: CRC Press. ISBN: 0-415-32462-9. https://nguyenduyliemgis.files.wordpress.com/2014/11/digital-terrain-modeling-principles-

and-methodology_2005.pdf

Lillesand, Thomas M., Ralph W. Kiefer, and Jonathan W. Chipman. 2015. *" Remote Sensing and Image Interpretation – Seventh edition."* New Jersey: John Wiley & Sons. ISBN: 9781118343289.

NASA. 1990. *"NASA Technical Reports Server (NTRS) – Providing Access to NASA's Technology, Research, and Science."* Accessed April, 2017. https://www.ntrs.nasa.gov/search.jsp?R=EL-1996-00130&qs=t%3D0%26N%3D125%2B4294947648%2B4294966788%26No%3D10

NASA. 2003. *"Visible Earth - A catalog of NASA images and animations of our home planet."* Accessed March, 2017. https://visibleearth.nasa.gov/view.php?id=68992

NASA. 2017. *"What are passive and active sensors?"* Accessed February, 2017. https://www.nasa.gov/directorates/heo/scan/communications/outreach/funfacts/txt_passive_active.html

Nelson, Vaughn. 2009. *"Wind Energy – Renewable Energy and the Environment."* Florida: CRC Press, Taylor Francis Group. ISBN: 978-1-4200-7568-7. http://library.uniteddiversity.coop/Energy/Wind/Wind_Energy-Renewable_Energy_and_the_Environment.pdf

Nibio. 2016. *"LandbruksMetrologisk Tjeneste."* Accessed April, 2016. http://lmt.bioforsk.no/agrometbase/getweatherdata_new.php

Norwegian Ministry of Petroleum and Energy. 2015. *"Facts 2015 – Energy and Water Resources in Norway."* Accessed June, 2017. https://www.regjeringen.no/contentassets/fd89d9e2c39a4ac2b9c9a95bf156089a/facts_2015_energy_and_water_web.pdf

Peacock, A.D.,D. Jenkins, M. Ahadzi, A. Berry, and S. Turan. 2008. *"Micro wind turbines in the UK domestic sector."* In *Energy and Buildings 40*, 1324-1333. Amsterdam: Elsevier. doi:10.1016/j.enbuild.2007.12.004

Tookapic. 2005. *"Photo 12600 by Alicya."* Accessed April, 2017. https://stock.tookapic.com/photos/12600

Vallis, Geoffrey K. 2006. *"Atmospheric and Oceanic Fluid Dynamics."* Cambridge: Cambridge University Press. ISBN: 978-0521-84969-2.

Versteeg, H.K, and W. Malalasekera. 1995. *"An Introduction to Computational Fluid Dynamics – The Finite Volume Method."* Harlow: Longman Scientific Technical. ISBN: 0-582-21884-5. https://ekaoktariyantonugroho.files.wordpress.com/2008/04/an-introduction-to-computational-fluid-dynamics-versteeg.pdf

Wendt, John F., John D. Anderson Jr., Joris Degroote, Gerard Degrez, Erik Dick, Roger Grundmann, and Jan Vierendeels. 2009. "*Computational Fluid Dynamics - An Introduction.*" Belgium: Springer. Third edition. e-ISBN: 978-3-540-85056-4. http://www.springer.com/us/book/9783540850557?token=prtst0416p

Wikimedia Commons. 2005. *"Darrieus Rotor by W.Wacker."* Accessed April, 2017. https://commons.wikimedia.org/wiki/File:Darrieus_rotor001.jpg

Wilcox, David C. 1993. *"Turbulence Modeling for CFD."* California: DCW Industries. ISBN: 0-9636051-0-0. https://www.scribd.com/doc/50191605/Turbulence-Modelling-CFD-Wilcox

Zhang, Zhao., Wei Zhang, Zhiqiang John Zhai, and Qingyan Yan Chen Kosasih, and P. Cooper. 2007. *"Evaluation of Various Turbulence Models in Predicting Airflow and Turbulence in Enclosed Environments by CFD: Part 2—Comparison with Experimental Data from Literature."*In *HVACR Research, 13:6*, 871-886. Oxfordshire: Taylor Francis. http://dx.doi.org/10.1080/10789669.2007.10391460